Synthesis and Characterisation of Barium Hexaferrite Nanoplatelets for Ferrofluids and Composites

Yusra Ahmed

A thesis submitted for the degree of
Doctor of Philosophy

Cardiff University
December/2025

Acknowledgements

Firstly, I would like to express my sincere gratitude to my supervisor, Daniel Zabek, for his invaluable advice, guidance, and unwavering support throughout the four years of my PhD. I am also grateful to my second supervisor, Jonathan Bartley, for his support and encouragement, particularly in helping me settle into the first year of study.

I would like to thank all my colleagues at Cardiff University, who made this journey both rewarding and memorable. I am grateful to all members of the MAGMA group, including Jeremy Hall, Phil Anderson, Christopher Harrison, and Phillip Lugg-Widger for their constant support, insightful discussions, and encouragement during our weekly meetings.

Lastly, I would like to thank my parents, husband, and siblings for their unconditional love, patience, and continuous support, without which this journey would not have been possible.

Abstract

A colloidal suspension of magnetic nanoparticles can offer exciting and ever – expanding opportunities for applications requiring hybrid particle/fluid phenomena. Ferrofluids are a classic example of this hybrid behaviour, whereby, radical changes in shape and magnetically controlled transport can be easily observed and has potential in a variety of technical and biomedical applications. It has been particularly challenging to make ferrofluids that are ferromagnetic in nature, such that they produce spontaneous, equilibrium magnetic ordering in the absence of an applied field. In contrast to conventional ferrofluids, this thesis focuses on ferrofluids based on barium hexaferrite nanoparticles, which exhibit distinctive magnetic properties due to their anisotropic structure. The primary aim of this thesis is to synthesis barium hexaferrite nanoparticles with optimal structural properties to enable stable dispersion in a non – volatile solvent, thereby producing a stable magnetic ferrofluid. The use of a non – volatile, high boiling point solvent is a deliberate design choice, as it extends the operational temperature range of the ferrofluid and opens the potential for exploration of practical applications that would not be achievable with conventional volatile carrier fluids. Some potential applications include magnetic hyperthermia for cancer treatment, magnetic sealing, magnetically directed drug delivery, sensors, actuators, and heat transfer applications among many others.

The first part of this thesis explores the optimal hydrothermal synthesis conditions for producing magnetically applicable barium hexaferrite nanoparticles with a platelet morphology and narrow size distribution. The surface of the nanoparticles is coated with a long – chain surfactant during the hydrothermal process which allows them to disperse in an appropriate carrier fluid. It has been shown that coating the nanoparticles with dodecylbenzenesulfonic acid (DBSA) surfactant allows an extremely successful dispersion in 1-butanol with long – term stability and excellent magnetic properties. However, 1-butanol is an extremely volatile solvent with limited miscibility in water. The experimental observations presented in this thesis show that replacing DBSA with hexadecyltrimethylammonium bromide (CTAB) surfactant allows dispersion of the barium hexaferrite nanoparticles in ethylene glycol which has a much higher boiling point than 1-butanol and is miscible in water. The resulting ethylene glycol ferrofluid shows long – term stability and comparable

magnetic properties to DBSA – coated barium hexaferrite nanoparticles. In addition, replacing 1-butanol with ethylene glycol greatly improves the applicability of the ferrofluid. The second part of this thesis utilises the ethylene glycol ferrofluid composing barium hexaferrite nanoparticles by taking advantage of the low volatility and high boiling point of ethylene glycol as a carrier fluid. A condensation polymerisation reaction between the ethylene glycol ferrofluid and succinic acid yields a novel polyethylene succinate (PES) based polymer matrix composite (PMC) with hard magnetic properties and a filler content much higher than previous studies.

List of Figures

List of Tables

List of Abbreviations

Abbreviation	Definition
AMNP	Anisotropic Magnetic Nanoparticles
SrM	Strontium Hexaferrite
BHF	Barium Hexaferrites
TEM	Transmission Electron Microscopy
PLAL	Pulsed Laser Ablation in Liquid
SAED	Selected Area Electron Diffraction
MRFs	Magnetorheological Fluids
DLVO	Derjaguin-Landau-Verwey-Overbeek
VDW	van der Waals
CTAB	Cetyl Trimethylammonium Bromide
GLYMO	Glycidoxypropyltrimethoxysilane
DLS	Dynamic Light Scattering
DBSA	Dodecylbenzenesulfonic Acid
SEM	Scanning Electron Microscopy
VSM	Vibrating Sample Magnetometer
PSD	Particle Size Distribution
HAADF STEM	High-Angle Annular Dark-Field Scanning Transmission Electron Microscopy
SDS	Sodium Dodecyl Sulfate
SAED	Selected Area Electron Diffraction
XRD	X-Ray Diffraction
XPS	X-ray Photoelectron Spectroscopy
TGA	Thermogravimetric Analysis
PES	Polyethylene Succinate
PMCs	Polymer Matrix Composites
PVA	Polyvinyl Alcohol
PAA	Polyacrylic Acid
FTIR	Fourier Transform Infrared
GPC	Gel-Permeation Chromatography
NMR	Nuclear Magnetic Resonance
TMS	Tetramethylsilane
DMSO	Dimethyl Sulfoxide

List of Variables

Variable	S.I. Units
Magnetic Flux Density - B	Tesla
Magnetic Field Strength H	A/m
Current – I	A
Magnetic Dipole Moment - p_m	$\mathrm{A/m^2}$
Magnetic Moment - M	$\mathrm{A/m^2}$
Local Magnetisation - $M(r,t)$	$\mathrm{A/m}$
Time – Averaged Magnetic Moment - δm	$\mathrm{A/m^2}$
Volume	$\mathrm{m^3}$
Mesoscopic Volume - δV	$\mathrm{m^3}$
Saturation Magnetisation - M_s	A/m
Magnetic Remanence -M_r	A/m
Coercive Field - H_c	A/m
Internal Susceptibility - χ	[-]
Magnetic Susceptibility - χ_m	[-]
Relative Permeability - μ_r	[-]
Electron Charge - e	C
Electron Mass - m_e	kg
Planck's Constant - h	[-]
Orbital Angular Momentum - l	$\mathrm{A/m^2}$
Orbital Spin Momentum - s	$\mathrm{A/m^2}$
Bohr Magneton - μ_B	$\mathrm{A/m^2}$
Curie Temperature - T_c	K
Demagnetizing Field - H_d	A/m
Magnetostatic Energy - E_{ms}	J
Anisotropy Energy - E_A	J
Demagnetising Factor - N_d	[-]
Single – Domain Diameter - D_{sd}	nm
Exchange Stiffness - A	J/m
magnetocrystalline Anisotropy - K_1	$\mathrm{J/m^3}$
Density - δ	$\mathrm{g/cm^3}$
Melting Point - T_m	K

Chapter 1: Introduction

Chapter 1 begins with an introduction to the fundamental concepts of magnetism, including magnetic field strength, flux density, and magnetic moment. A clear understanding of these terms is essential for appreciating the different classes of magnetic behaviour, such as ferromagnetism and ferrimagnetism. The discussion then considers how these materials respond to an applied magnetic field and the key parameters that distinguish them, namely coercivity, magnetic saturation, remanence, and magnetocrystalline anisotropy. Further attention is given to shape anisotropy and size-dependent magnetic effects, which provide additional insights into the magnetic character of materials.

1.1. Magnetic field of a solenoid

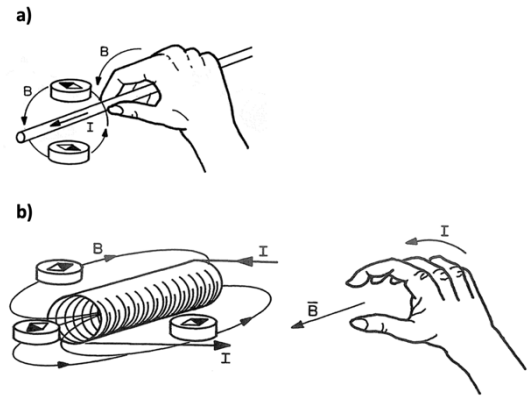

Figure 1: electrical conductor carrying an electric current – I and exhibiting a magnetic field - B perpendicular to the current. Right – hand with thumb showing direction of current and direction of magnetic B field about a current. In the case of a solenoid, thumb showing direction of magnetic B field (a) and curled fingers around the solenoid in the direction of the current in the loops of the solenoid (b)[1].

The field of magnetism encompasses the study of magnetic properties of matter and their interaction with magnetic fields. A magnetic field is generated as a current – I(A) (in the form of a continuous flow of electric charge) is passed through a length of wire. The direction of the positive current I and the magnetic field can be explained using the right – hand rule, here the thumb indicates the direction of the positive current while the fingers indicate the direction of the magnetic field lines $B\,(\mathrm{HA/m^2}$ defined as $\mathrm{Wb/m^2}$ or tesla) (**Figure 1a**). If a length of current – carrying wire is formed into a solenoid, a parallel magnetic field can be observed inside the solenoid. This time the direction of the fingers indicates the direction of current while the thumb gives the direction of the magnetic field

inside the solenoid (**Figure 1b**). The constitutive relations are equations that describe how a material responds to electric or magnetic fields. In terms of an electric conductor carrying a current, the magnetic field strength H(A/m) can be described as, $H = I/L$, where I is the current and L is the length of the wire (m)[1].

1.1.1. Magnetic field strength, *H*

The H(A/m) field, also known as the magnetic field strength or the magnetisation force is an indispensable auxiliary field described for magnetic or superconducting materials. Magnetic materials generally respond to an applied magnetic field H with a change in their magnetic dipole moment p_m $(\mathrm{A/m^2})$ and their magnetic moment $M\,(\mathrm{A/m})$ (intrinsic property of the magnetic material) reflects the local value of H[1].

1.1.2. Magnetic flux density, *B*

The magnetic flux density B can be related to M and H by the permeability where, $\mu = \mu_r\mu_0$ with $\mu_0 = 4\pi \times 10^{-7}$ henry/m. To consider a closed loop path as in **Figure 1a** again, where it can be assumed that B is circular and has a constant value at a distance – *r* [m] from the wire. Integrating around *r* follows:

$$B(r) = \frac{\mu_0 I}{2\pi r} \quad (1)$$

Where B has units Tesla. The above can also be described in terms of the magnetic field $H = B/\mu_0$ (A/m) generated by the current:

$$H = \frac{1}{2\pi r} \quad (2)$$

The magnetic induction in matter is dependent on H and the magnetisation M, as shown by the equation below:

$$B = \mu_0(H + M) \quad (3)$$

In free space, $M = 0$, $B = \mu_0 H$ and B and H are indistinguishable, apart from the constant μ_0 which is very small.

1.1.3. Magnetic moment, *M*

To discuss the microscopic origin of magnetism in materials, it is important to understand the atomic magnetic moment. The elementary quantity in solid – state magnetism is the magnetic moment M ($\mathrm{A/m^2}$), and the magnetisation $M(r)$ is its mesoscopic volume average. The intrinsic magnetic moment of an atom is associated with the spin of each electron (electromagnetism) and a further contribution is associated with its orbital motion around the nucleus (origin of magnetism). $M(r,t)$ is the local magnetisation at a specific point, r in space and at a particular time, t. $M(r,t)$ is often described in literature as fluctuating significantly on a sub-nanometre scale as well as rapidly in time on a sub-nanosecond scale. However, for simplicity, it is more appropriately described as a mesoscopic average $\langle M(r,t) \rangle$ over a distance of order a few nanometres, and times of order a few microseconds to reach a steady, homogenous, local magnetisation $M(r)$. The time – averaged magnetic moment δm ($\mathrm{A/m^2}$) in a mesoscopic volume δV ($\mathrm{m^3}$) is:

$$\delta m = M \delta V \quad (4)$$

This magnetisation can be the saturation magnetisation M_s (A/m) within a ferromagnetic domain or it may be the uniform magnetisation of a paramagnet or a diamagnet induced by an applied field[2]. Spontaneous magnetisation is usually associated with a hysteresis loop and is an eminent manifestation of magnetisation of ferromagnetic materials. The values of M_s of some ferromagnetic elements such as Fe, Co, and Ni at 298 K are 1720, 1370 and 485 kA/m, respectively. For magnetite, the M_s is 480 kA/m, while a large electromagnet can produce a field of 1000 kA/m.[2]

1.1.4. Magnetic moment per unit volume

A magnetic solid is made up of a large number of atoms with magnetic moments. The magnetic moment per unit volume is a fundamental concept in magnetism and provides a measure of the magnetic properties of a material at a microscopic or macroscopic level. The specific moment per unit volume is a standard measured value for solid magnets. However, when the particles are small or in powder form, the magnetic properties are significantly different to those in bulk. Therefore, when measuring the magnetic properties of a powder, the magnetic moment per unit volume cannot be measured reproducibly due to randomly orientated particles and the presence of air voids, hence a true sample volume is difficult to obtain. Instead, the magnetic moment per unit weight is measured by taking into account the density of the material, generating the mass magnetisation.

1.2. Magnetic susceptibility and magnetic permeability

Magnetic susceptibility χ_m [-], is a dimensionless parameter describing the degree to which a material becomes magnetised in response to an applied magnetic field *H*.

$$M = \chi_m H \qquad (5)$$

Where *M* is the magnetisation induced within the material. Diamagnetic, and many paramagnetic materials exhibit small susceptibilities, typically in the range of about -10^{-6} to 10^{-3}. In contrast, ferromagnetic materials can have much larger and strongly field – dependent susceptibilities, reaching values of 10^3 or higher. The magnetic flux density *B* is related to *M* and *H* by the permeability $\mu = \mu_r \mu_0$ with $\mu_0 = 4\pi \times 10^{-7}$ henry/m and μ_r [-] is relative permeability.

$$B = \mu_0(H + M) = \mu_0(H + \chi_m H) = \mu_0(1 + \chi_m)H = \mu H \quad (6)$$

$$B = H + 4\pi M = H + 4\pi\chi_m H = (1 + 4\pi\chi_m)H \qquad (7)$$

Therefore, $\mu_r = 1 + \chi_m$. The parameters μ_r and χ are different ways of describing a material's response to a magnetic field. Permeability and susceptibility can be described as tensors as they relate two vector quantities that are not parallel. Permeability is often discussed in relation to ferromagnetic materials where relative permeability can be large in value, up to 10^4 or more[1,3].

1.3. Orbital angular momentum

Magnetism relates to angular momentum of elementary particles, i.e. protons, neutrons, and electrons, which all possess an intrinsic angular momentum $\frac{1}{2}\hbar$ (J s) known as spin, where $\hbar$ is Planck's constant h divided by 2π.

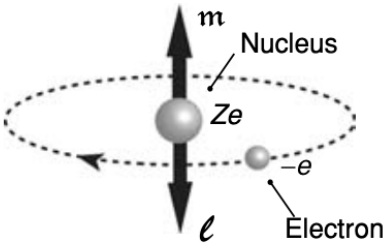

Figure 2: the Bohr atom, the electron moves in a circular orbit where its quantised angular momentum l and magnetic moment m are oppositely directed[2].

The orbital moment can be understood using the Bohr model (**Figure 2**) of the atom in which electrons revolve around a nucleus with charge Ze in circular orbits. An electron circulating in its orbit can be visualised as generating a small current loop and producing a magnetic moment, m (A m^2). In quantum mechanics, the orbital angular momentum is quantised and described by the orbital quantum number l as shown below (where e (C) is the charge and m_e is the mass (kg))[2].

$$m = -\frac{e}{2m_e} l \quad (8)$$

1.3.1. Spin angular moment

Along with orbital moment, the electron also possesses intrinsic spin angular momentum with quantum number s. Electrons possess an intrinsic magnetic moment, independent of their orbital motion which can align in one of two discreet orientations relative to a

magnetic field. s can be described in terms of spin magnetic moment, m as shown below (where e (C) is the charge and m_e is the mass (kg))[2].

$$m = -\frac{e}{m_e} s \quad (9)$$

1.3.2. Spin – orbit coupling

The magnetic properties of solid materials arise from the magnetic moments of their atomic electrons while the magnetic dipole moments are due to the orbital or spin angular momentum. The spin magnetic moment of a single electron is $\mu_s = \pm e\hbar/2m$ (where e is elementary charge of electron, $\hbar$ is Planck's constant and m is electron mass), which is called the Bohr magneton:

$$\mu_B = \frac{e\hbar}{2e} \quad (10)$$

$$= 0.927 \times 10^{-23} \, (A \, . m^2)$$

Both orbital and spin moments contribute to the overall magnetism of an atom, hence a weighting factor is described to give their relative contributions. This weighting factor is called the $f$factor: $g = 1$ for orbital magnetism only $(s = 0)$ and $g = 2$ for spin magnetism only $(l = 0)$. The spin – orbit coupling is an extremely important interaction for magnetic phenomena that are key to most applications of magnetic materials. This coupling interaction describes the effects of an electrons' orbital motion on the orientation of its spin. The spin – orbit coupling interaction is essential for magnetocrystalline anisotropy, magnetostriction, magnetooptic effects, anisotropic magnetoresistance[1].

1.4. Ferromagnetism and Ferrimagnetism

The main classes of magnetic materials are the ferromagnets, antiferromagnets and ferrimagnets, these are defined in terms of the relative orientations and magnitude of the atomic or molecular magnetic moments. However, for brevity, only ferromagnetism and ferrimagnetism will be discussed in detail.

Type	Example	Atomic/Magnetic Behaviour		
Ferromagnetism	Transition metals Fe, H, Co, Ni; alloys of ferromagnetic elements; some alloys of Mn, e.g. MnBi, Cu_2MnAl.	Atoms have parallel aligned magnetic moments. Susceptibility is large (below T_C).	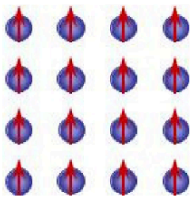	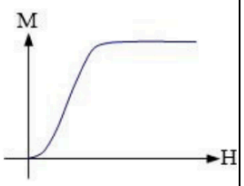
Antiferromagnetism	Transition metals Mn, Cr and many of their compound, e.g. MnO, CoO, NiO, Cr_2O_3, MnS, MnSe.	Atoms have anti-parallel aligned magnetic moments. Susceptibility is small and positive, $+10^{-5}$ to $+10^{-3}$.	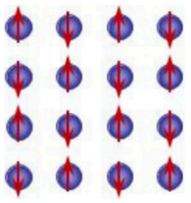	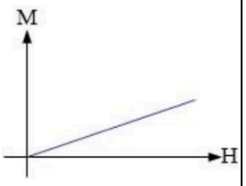
Ferrimagnetism	Fe_3O_4 (magnetite); γ-Fe_2O_3 (maghemite); mixed oxides of iron and other elements such as Sr ferrite.	Atoms have mixed parallel and anti-parallel aligned magnetic moments. Susceptibility is large (below T_C).	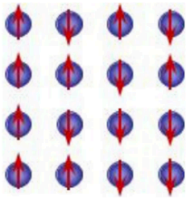	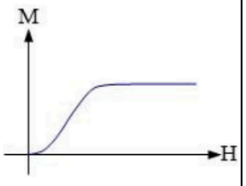

Figure 3: A summary of ferromagnetism, antiferromagnetism and, ferrimagnetism. Including examples of each magnetic behaviour and atomic alignment in response to a magnetic field.

Figure 3 shows a summary of ferromagnetism, antiferromagnetism and, ferrimagnetism with their corresponding atomic alignment to an applied magnetic field, H. Ferromagnetism is a term derived from the magnetism detected in Fe^{2+} or Fe as iron was the first element in which ferromagnetism was observed[4]. Common elemental ferromagnets also include iron, nickel and cobalt. While all materials respond to a magnetic field to some degree, many of them are paramagnetic (e.g. aluminium and platinum), or diamagnetic materials (e.g. copper and silver) which means they have a weak or undetectable magnetic property. Ferromagnetic materials are those most commonly known as “magnetic materials” and are

materials that can become a permanent magnet or strongly react to a magnetic field[5]. Ferromagnetism in materials is only possible when the atoms are arranged in a lattice and the atomic magnetic moments can interact to align parallel to each other as shown in **Figure 3**. Weiss presented the idea of magnetic domains within a material and the atomic magnetic moments align within these regions[6]. Ferromagnetic materials are often compared in terms of saturation magnetisation i.e. when all domains are aligned.

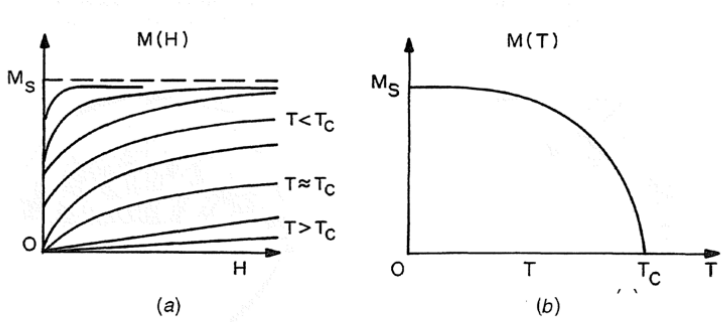

Figure 4: magnetisation of a strongly magnetic material (ferromagnet) verses field (H)(a), and how M_s decreases with temperature up to Curie temperature T_c [1].

Ferromagnetic materials are distinguished by a long – range ordering of their atomic moments, even in the absence of an external field. This spontaneous long – range magnetisation of a ferromagnet disappears above a specific ordering temperature called the Curie temperature T_c. **Figure 4a** shows the dependence of magnetisation M_s on the applied magnetic field *H* at different temperatures. **Figure 4b** shows the temperature dependence of the spontaneous magnetisation *M(T)* in zero applied magnetic field. When heated above T_c, these ferromagnetic materials lose their magnetic properties and become weakly magnetic, i.e. paramagnetic. This is because the thermal energy above T_c is high enough to break the internal alignments of domains while below T_c, magnetism can be permanently induced in these materials[7]. The relative magnetic permeability $\mu_r = \mu/\mu_0 (= 1 + \chi_m)$ is more commonly used to describe the magnetic response of a ferromagnetic material to H, as compared to susceptibility. This is because ferromagnets are typically used in electromagnetic devices where B or $\partial B/\partial t$ is more important when producing a voltage is considered[1].

In contrast to ferromagnets, where atomic magnetic moments align parallel to produce a net magnetisation, some magnetically ordered materials can exhibit antiparallel coupling of neighbouring moments such that the resultant magnetisation is zero. Materials with this arrangement are called antiferromagnets (**Figure 3**). Similar to ferromagnetic materials

losing spontaneous magnetisation at a specific T_c, antiferromagnetic materials lose their long range magnetic ordering above their corresponding Néel Temperature T_n. Antiferromagnets have limited applications as their net magnetisation is zero, which means they produce no external field and the direction of the atomic moments is not easily affected by an external field[1]. The cancellation of opposite magnetisation in two antiferromagnetically coupled sublattices is only possible for identical magnetic moments. However, we can also consider the case of two sublattices in which the magnetic moments are unequal due to the magnet comprising atoms of different materials, or because the ions are not the same, e.g. Fe^{2+} in one lattice and Fe^{3+} in another. In this case, the antiferromagnetic coupling between the two sublattices leads to a partial cancellation of the magnetic moment. Hence, the total magnetisation at low temperatures is the difference between that of the two sublattices which is not zero. Such materials are called ferrimagnets, an example of which is magnetite, Fe^3O^4, which has iron ions of different valence at sites of different coordination. The exchange interactions in these materials lead to parallel alignment of atoms in some of the crystal sites and anti – parallel alignment of others. Like ferromagnets, the material consists of magnetic domains, but ferrimagnets usually have lower saturation magnetisations. Having said this, ferrimagnets (e.g. Fe_3O_4 and $BaFe_{12}O_{19}$)[2] are very important due to their good high frequency properties[8].

1.5. Magnetostatic energy

Magnetostatic energy is an effect that contributes to the energy of a ferromagnetic material. The magnetostatic energy, also called stray field or dipolar energy is measured by the magnetic energy of a sample in its own magnetic field. This is the demagnetisation or demagnetizing field which is the field arising from the divergence of the magnetisation and is represented by the symbol H_d(A/m). It can be derived using Maxwell's equation:

$$div\ B = div\ \mu_0(H + M) = 0$$

$$div\ H_d = -div\ M \qquad (11)$$

The magnetostatic energy E_{ms} (J), is given by the energy of the magnetisation in the demagnetizing field as shown below:

$$E_{ms} = -\frac{1}{2}\mu_0 \int_V H_d \cdot MdV \qquad (12)$$

Where the integral includes the volume – V [m^3] of the sample, V. The $\frac{1}{2}$ factor is important as it accounts for the fact that the magnetostatic energy arises from the interaction of the magnetisation with the magnetic field that it creates, hence this energy term is also called the magnetic self – energy. The magnetostatic energy of samples with a spherical shape can be easily determined as the magnetic field is the same at every point of the sample, this is also true for samples with a thin film of wire – like morphology[9].

1.6. Fundamentals of magnetic anisotropy

Anisotropy in a material is present when one of its physical properties is a function of direction, likewise, magnetic anisotropy is the preference for the magnetisation to lie in a particular direction in a sample. Parameters such as permeability and susceptibility can be used to describe the magnetisation process. Therefore, these parameters are functions of the direction in which the field is applied to the material. The energy of a magnetically ordered sample depends on the relative direction of the magnetisation and the structural axes, and hence the solid has a preferred axis along which the energy is at a minimum. Magnetic anisotropy can be a result of sample shape, crystal symmetry, stress, or directed atomic pair ordering.

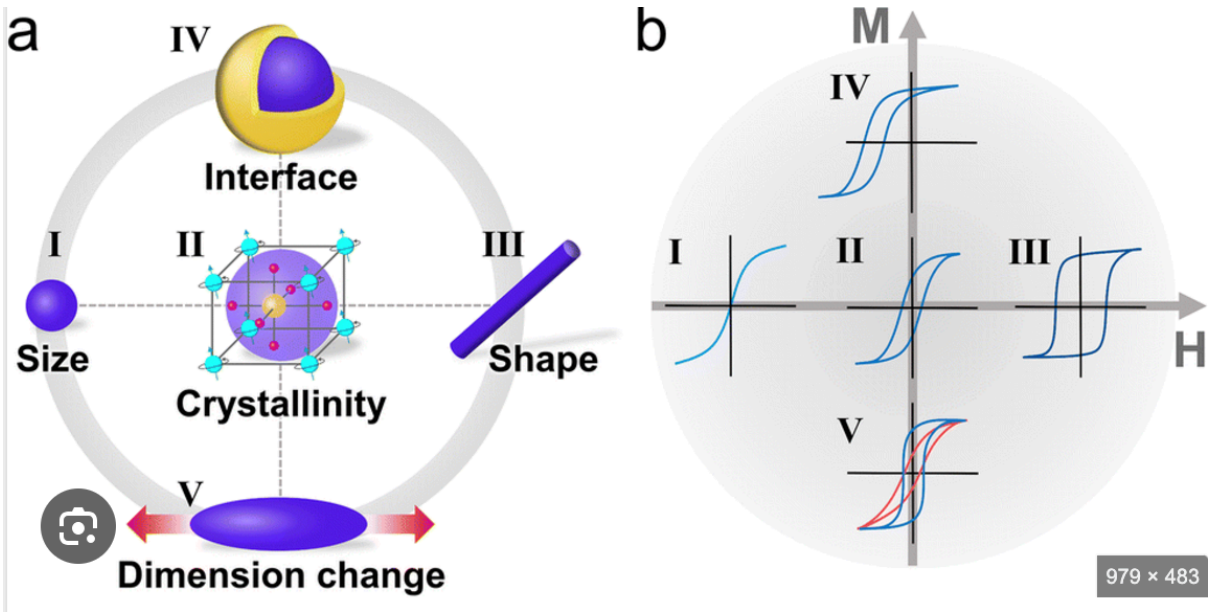

Figure 5: Factors influencing the magnetisation states of nanoparticles, the magnetic properties induced by size (I), crystallinity (II), shape (III), interfacial coupling (IV) and dynamic changes (V) (a). Also, how these factors influence the hysteresis loop (b), such that a decrease of size led to superparamagnetism (I), the crystal structure determined the inherent magnetisation (II), shape anisotropy resulting in increased coercivity and remanence magnetisation (III), exchange coupling at interface between different magnetic materials causing curve shifts (IV), and effect of dynamic changes in the magnetisation states (V)[10].

Figure 5 shows the variables influencing the magnetisation states of nanoparticles, such as size, crystallinity, and shape (**Figure 5 (a)**) and how the anisotropy energy influences the hysteresis loop based on these factors (**Figure 5 (b)**). The magnetic properties induced by size, crystallinity, shape, interfacial coupling, and dynamic changes can be verified by the magnetic hysteresis loop, which is a characteristic curve that shows how a magnetisation responds to an applied magnetic field. A decrease in the size of magnetic particles below the sub – nanometre scale (**Figure 5 a(I)**), reduces the magnetic anisotropy energy caused by crystal orientation across the entire volume of the particle. When this energy falls below the thermal energy threshold, the magnetic orientation within the particle experiences thermal fluctuations, which are common in paramagnetic materials. This phenomenon is called superparamagnetism and yields a narrow hysteresis loop with negligible coercivity (**Figure 5 b(I)**)**.** The crystal structure of a material (**Figure 5a(II)**) will also determine the inherent magnetisations as an enhancement in the coercivity can be seen as crystallinity of a material

improves and magnetic anisotropy energy increases (**Figure 5b(II)**). **Figure 5b(III)** shows an increase in coercivity and remanent magnetisation as a function of shape anisotropy (**Figure 5a(III)**). **Figure 5b(IV)** shows a shift in the hysteresis loop due to exchange anisotropy which describes the magnetic interaction across the interface (**Figure 5a(IV)**) between two magnetic materials, one of which is typically antiferromagnetic[11]. The parameters described in **Figure 5(I – IV)** describe the magnetic anisotropy in a static state without considering potential dynamic states of a material, such as, applied mechanical stress, temperature changes, and the different strengths and directions of stray fields. **Figure 5a(V)** illustrates how the dimensions of a material can vary in response to a change in its magnetisation orientation, this is a phenomenon called magnetostriction. Magnetic materials exhibit strain of the saturation magnetostriction coefficient (γ_{si}) in the direction of the magnetic field during magnetisation. If (γ_{si}) is positive, the material elongates during magnetisation which increases the remanent magnetisation (**Figure 5b(V)**)[10].

1.6.1. Intrinsic Magnetocrystalline anisotropy

Crystallographic orientations in magnetic materials determine preferential directions of magnetisation to minimise anisotropy energy, this is referred to as magnetocrystalline anisotropy. This is an intrinsic property originating from the spin – orbit interaction. The electron orbits are linked to the crystallographic structure and through their interaction with the spins, they cause the preferred direction of alignment to be along the well – defined crystallographic axes. Therefore, certain directions in space are easier to magnetize a given crystal than other directions. The simplest case is the uniaxial magnetic anisotropy. In the case of hexagonal cobalt, the uniaxial anisotropy has a preferred direction of spontaneous magnetisation parallel to the c – axis of the crystal at room temperature. As the magnetisation deviates away from the c – axis, the anisotropy energy increases with θ (°) which is the angle between the c – axis and the magnetisation vector. After this initial increase, the anisotropic energy then reaches a maximum value at $\theta = 90°$, and decreases to its original value at $\theta = 180°$. The anisotropy energy is minimum when the magnetisation points in either the + or – direction along the c – axis. The anisotropy energy (E_A) per unit volume can be shown as[8]:

$$\frac{E_A}{V} = K_1 sin^2\theta + K_2 sin^4\theta \qquad (13)$$

The coefficients K_1 and K_2 are called anisotropy constants and θ is the angle of magnetisation with the single axis. If these constants are positive as in the case of cobalt, the anisotropy energy E_A increases with increasing angle θ, which makes E_A minimum at $\theta = 0$. In other words, the material has a stable spontaneous magnetisation when it is parallel to the c – axis. This stable magnetisation is often referred to as an axis of easy magnetisation or an easy axis. On the other hand, if these constants are negative, E_A is maximum at the c – axis, which makes it unstable, and this is called an axis of hard magnetisation or simply a hard axis. Additionally, depending on the magnitude of the constants, the sample can have an easy axis (for large $|K_1|$, $K_1 > 0$), easy plane (for large $|K_1|$, $K_1 < 0$), and conical for intermediate values of the constants. These anisotropy constants have dimension of energy per volume (measured in J/m)[9].

1.6.2. Magnetic domains and domain walls

A ferromagnetic sample of macroscopic size has several regions called magnetic domains in its demagnetised state. Spontaneous magnetisation of the sample occurs when all of the atomic moments within each domain are aligned in one of the easy directions. A uniformly magnetised sample is divided into these magnetic domains to balance the contributions of the many different energy terms. These energy terms include the exchange energy, magnetocrystalline anisotropy and magnetostatic energy. The exchange energy tries to align all magnetic moments in the same direction, while the magnetocrystalline anisotropy tries to orient magnetic moments along specific directions (equation 13) and the magnetostatic energy aims to eliminate the magnetisation in the material[12].

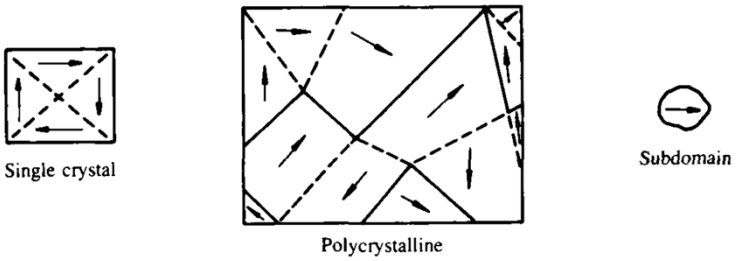

Figure 6: ferromagnetic domain structures for single-crystal, polycrystalline, and subdomain samples. Crystal walls are shown solid, domain walls dashed[5].

Figure 6 shows an illustration of the domains in a single – crystal, polycrystalline and subdomain material. As the number of magnetic domains is increased, the magnetostatic energy is reduced. However, an indefinite reduction of magnetostatic energy is not possible as domain walls, which are the transition regions between the domains, also cause an increase in exchange and anisotropy energy. Single domain materials do not represent the ideal image of a region where the magnetisation is identical at every point. This is because the demagnetizing field H_d varies from point to point in every sample that has a non – ellipsoidal shape. As a result, the equilibrium configuration of the magnetic moments in these samples are not homogeneous. The sample is still considered to be single – domain, including any magnetic object that does not have clearly defined domain walls. Two main types of domain walls exist, including Bloch walls and Néel walls and they differ in the way the atomic magnetic moments in the wall turn, which is perpendicular to the plane of the moments in adjacent domains for Bloch walls, or parallel to this plane for Néel walls[9]. The minimum particle or grain size which is magnetically stable against ambient thermal demagnetisation can be described using equation 14. For a spherical particle with $K_u = 10^5$ J/m^3, the superparamagnetic radii for stability over 1 year and 1 second, respectively, is as follows. Where k_B is Boltzmann constant, r is radii, and T is temperature.

$$r_0^{1\,yr} \approx \left(\frac{10k_BT}{K_u}\right)^{1/3} \approx 7.3\ nm,\ r_0^{1s} \approx \left(\frac{6k_BT}{K_u}\right)^{1/3} \approx 6\ nm \qquad (14)$$

In terms of a multidomain sample, an applied magnetic field can induce a displacement of the magnetic domain walls. For example, a magnetic field applied in the z direction will create a torque on the magnetic moments inside the walls which will generate a

magnetisation component perpendicular to the plane of the wall (the yz plane). This magnetisation component creates a demagnetising field also perpendicular to the wall with a consequential torque that rotates the moments of the wall in such a way to increase the size of the domain with magnetisation in the $+z$ direction. This describes the mechanism that induces domain wall motion under an applied field. In addition, the magnetic domains and domain walls are significantly influenced by point defects and edges, point defects, such as vacancies, interstitial atoms, or impurities, create local stress fields in the crystal lattice, which can alter the energy landscape of the material. In reality, domain walls do not move reversibly and grain boundaries, precipitates, inclusions, surface roughness, and other defects lower the wall energy at a specific position in the material. These defects can act as pinning centres that hinder the motion of domain walls, or they can place a barrier in front of the wall, preventing further wall motion.

1.6.3. Shape anisotropy

To understand the magnetic properties of a material, it is important to consider the several factors that affect the shape of its hysteresis loop. One such factor is magnetic anisotropy which implies that the magnetic properties of a material depend on the direction in which they are measured. Magnetocrystalline anisotropy is the only kind of anisotropy that is intrinsic to the material while the others are either extrinsic or induced. The focus of this section is shape anisotropy and how it affects the magnetic properties of the material composed of anisotropic magnetic nanoparticles (AMNP). A spherical magnetic nanoparticle differs from an AMNP as it can be magnetised homogenously in any direction while AMNPs are easily magnetised along their long axis than along their short axis. In other words, a demagnetising field, H_d that will demagnetise a sample composing AMNPs, is larger along the short axis than along the long axis[13]. This is represented in the following equation,

$$H_d = -N_d M \quad (15)$$

Where N_d is a demagnetising factor dependent on shape and direction of the magnetic nanoparticles. N_d is the same in all directions for a spherical particle but differs for different directions in AMNPs such as elongated and plate – like particles[14].

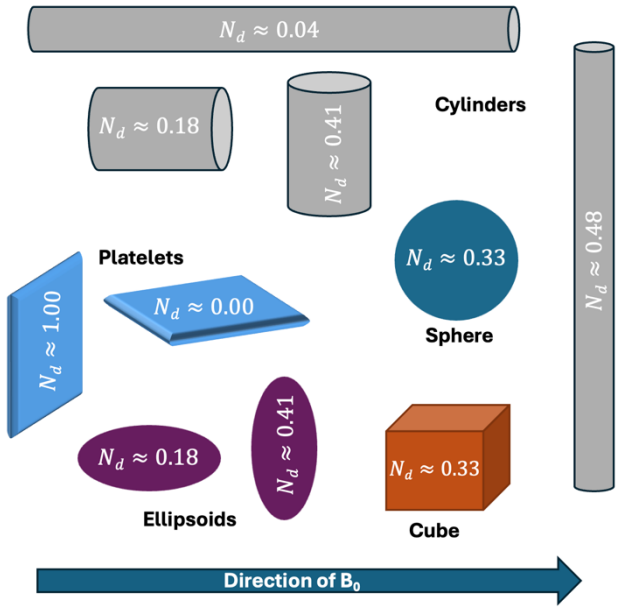

Figure 7: shows how the demagnetisation factor N_d changes with nanoparticle orientation depending on direction of B_0 for platelets, sphere, cube, ellipsoids and cylinder shapes.

The geometry of particles can also have a significant effect on its magnetic behaviour. The demagnetising factor is important here as H_d is strongly dependent on the shape and orientation of a ferromagnetic object in the external field. Different shapes of magnetic particles have different demagnetising factor, N_d values. Generally, particles with a large relative surface area facing the direction of the magnetisation field have a higher N_d value. For example, an idealised thin vertical plate perpendicular to the magnetisation field has a N_d value of 1.00 which is the highest possible value, whereas a plate parallel to the field has an N_d value of 0.00, as illustrated in **Figure 7**.

1.7. B – H loops

Ferromagnetic materials are known for their spontaneous magnetisation which is illustrated in their unique hysteresis loop, a phenomenon studied by James Ewing in 1881[2].

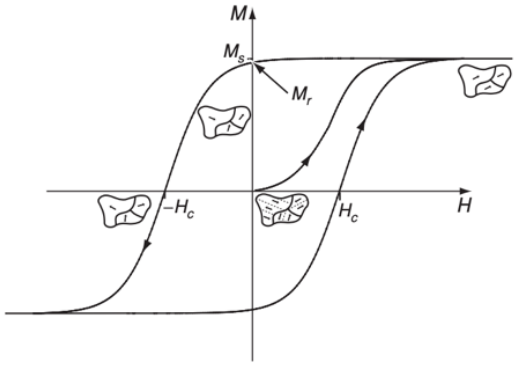

Figure 8: hysteresis loop of a ferromagnetic material, showing M_s, M_r and H_c[2]

The hysteresis loop of a ferromagnetic material shown in **Figure 8**, can be described as a closed curved of magnetisation verses magnetic field. This curve is observed by varying the field from H_{max}, which is a field that saturates a ferromagnetic sample, to - H_{max} and back to H_{max}. As the magnetic field is reduced from H_{max} to zero, the magnetisation varies from M_s (A/m), which is the saturation magnetisation to M_r (A/m), which is the magnetic remanence. The application of a weak field produces motion of the domain walls, causing volume expansion of the domains which have the largest component of M along H. The initial magnetic induction B produced in response to the small field H, defines the initial permeability $\mu_i = (B/H)$. At higher fields, B increases rapidly, and the permeability reached a maximum μ_{max}. When most domain wall motion is completed, some domains with nonzero components of magnetisation remain at right angles to the applied field direction. It is necessary to rotate the magnetisation of these domains into the field in order to minimize the potential energy. This process is energy costing, more so than wall motion as it involves rotating the magnetisation away from an easy direction (which is fixed due to magneto crystallography, sample shape or stress).

Magnetic saturation Ms is reached when the applied field is of sufficiently high magnitude and when the wall motion and magnetisation rotation is complete. As the magnitude of applied field is decreased, the magnetisation rotates back towards its easy directions, without hysteresis. A further decrease in the field causes domain walls to move back across the sample. Energy is lost from sudden domain wall changes from one energy minimum to the next. This results in the B – H loop to become apparent, i.e. hysteresis loop is produced.

The induction and magnetisation remaining in the sample when the applied field is zero are called residual induction Br and remanence Mr, respectively. The materials start to become demagnetised once the direction of the magnetic field is reversed, the reverse field needed to restore B to zero, i.e. demagnetise the material, is called coercivity or coercive field H_c (A/m). It can be thought of as a measure of how easy or difficult it is to magnetise a material. To conclude, a B – H loop is produced when a cyclic application of increasing and decreasing magnetic field is applied. It should be noted that the concepts presented are discussed in relation to magnetostatistics only which refer to situations where there is no time dependence[1].

1.8. Hard and soft magnetic materials

The measured value of coercivity is an indication of how magnetically hard or soft a material is. Typically, soft magnetic materials exhibit $H_c < 10^3$ A m^{-1}, while magnetically hard materials show $H_c > 10^4$ A m^{-1}. Soft materials such as Fe alloys and spinel ferrites based on $MeFe_2O_4$ (Me = bivalent transition metal) have low H_c and M_r values and exhibit a narrow, S - like magnetic hysteresis loops. In certain very soft magnetic materials such as some crystalline NiFe alloys or amorphous metallic alloys, the H_c can be as low as 1.0 A/m. These are temporary magnets which readily lose their magnetisation as soon as the external magnetic field is removed. On the other hand, hard magnetic materials are referred to as permanent magnets and are able to resist demagnetisation once magnetised. This is the case when the material has strong defects that disrupt wall motion or if it consists of single domain particles with such high magnetic anisotropy that the direction of magnetisation can only be changed by extremely large fields. In contrast to the narrow B – H loops of a soft material, hard magnetic materials generally produce a broad, square – like hysteresis loop. Hexaferrites such as barium hexaferrite are an example of hard or permanent magnets[1].

1.9. Size and geometric dependent properties

The magnetic properties of a material can be affected by many factors such as geometry, composition, and size. This section focuses on the size dependent magnetic properties and

how they can be characterised. Nanoparticles can be defined as particles with at least one dimension between approximately 1 and 100 nanometre (nm) and usually contain several hundreds to 10^5 atoms[15]. As the size of the particle decreases, the ratio of the surface area to the volume of the particle increases. This ratio is even more significant for nanoparticles as a large portion of the atoms will reside on the particle surface compared to the core of the particle. This large surface – to – volume ratio of the nanoparticles determines the novel physical, chemical and mechanical properties as opposed to the corresponding bulk material[16].

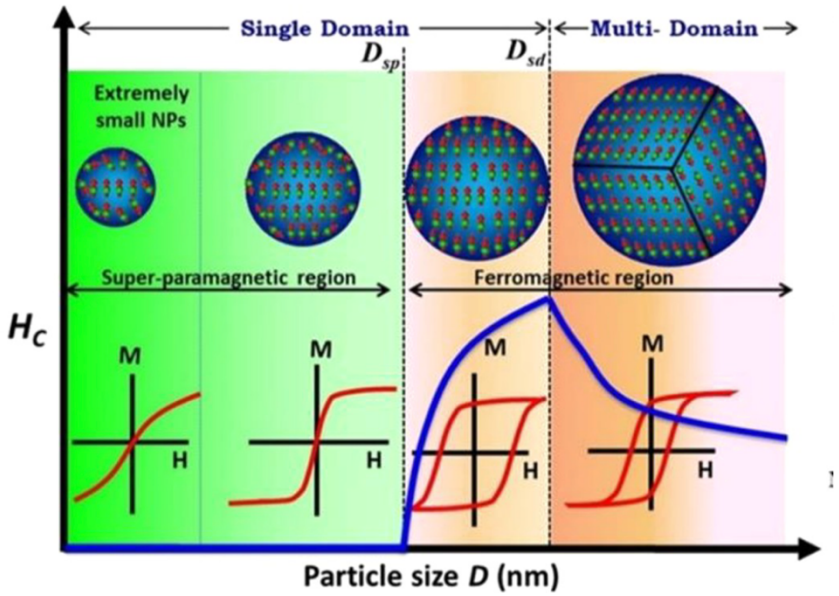

Figure 9: nanoparticle-size-dependent magnetisation and magnetic coercivity (Hc) for spherical (Fe_3O_4) particles[14].

The magnetic moment per atoms and magnetic anisotropy of nanoparticles can be different to that of the bulk magnetic material. Other magnetic properties such as the Curie temperature, Nèel temperature and coercivity field for nanoparticles are also found to be different from the bulk material. As discussed previously, a bulk ferromagnetic material composes small regions called magnetic domains. These magnetic domains exist due to a balance between several energy terms, which include, the exchange energy, magnetocrystalline anisotropy and the magnetostatic (or dipolar) energy. The magnetic properties of a bulk material are determined by anisotropic and coherent coupling among free electrons within magnetic domains and domain – domain interactions. As the

dimensions of the material is reduced to nanometre size, the magnetic properties of the material change as multiple domains no longer exist within the material structure, this is illustrated in **Figure 9**. Hence, at a specific critical diameter, the material can only support a single domain, and this specific diameter is called the single – domain diameter (D_{sd}). D_{sd} (nm) can be calculated using the equation below[17]:

$$D_{sd} = \frac{18(AK_1)^{1/2}}{\mu_0 {M_s}^2} \qquad (16)$$

Where *A* is the exchange stiffness (in J/m) and K_1 is the magnetocrystalline anisotropy (in J/m^3). The critical diameter (D_{sp}) at which a particle exhibits superparamagnetic properties can be defined as:

$$D_{sp} = \left(\frac{48 k_B T}{k_1}\right)^{1/3} \qquad (17)$$

Coercivity, H_c is an important parameter to consider when studying the relationship between size and magnetic properties. For particles with diameters well below D_{sd}, i.e. typically a few nanometres, the magnetic moment - M_s is not stable and hence their $H_c = 0$. For an intermediate diameter (typically 20 nm < D < 100 nm for a soft magnetic material), the moment is stable, and the particle is single domain. Single – domain particles prefer to be uniformly magnetised along one anisotropic easy axis, which produces a large coercivity. However, below D_{sd}, the magnetic anisotropy energy (K_1V (J/m^3), where V (m^3) is the volume of the particle) reduces and therefore the coercivity value also reduces. Nevertheless, coercivity for single domain particles will increase as their diameter increases. Depending on the magnetic hardness of the material, there may be a region where the coercivity falls due to vortex magnetic order. Finally, as the particle diameter continues to increase, particles with much larger diameters, typically above several micrometres, start to form a multidomain regime and the coercivity decreases with increasing diameter. This can also be seen in **Figure 9**.

1.9.1. Different shapes of magnetic nanoparticles

The previous section highlights the relationship between size and magnetic properties. In comparison, there are limited scientific reviews that collectively report the effect of shape on the magnetic properties of nanoparticles having the same volume or relevant parameter.

Table 1: shows different shapes of magnetic nanoparticles with an example, typical diameter (nm) of these shapes, magnetic hard/soft properties, and aspect ratio.

Shape	Example	Size/diameter (nm)	Hard/soft	Aspect ratio	N_d (-) Perpendicular to field
Sphere[18]	Fe_3O_4	10 – 100	Soft	Low	0.33
Cube[19]	$MnFe_2O_4$	10 – 50	Soft	Low	0.33
Ellipsoid[20]	λ-Fe_2O_3/SiO_2	200 - 300	Soft	High	0.41
Platelet[21]	$BaFe_{12}O_{19}$	30 – 150	Hard	High	1.00
Cylinders/rods[22]	Ni	10 – 100	Super paramagnetic	High	0.48

Table 1 shows the many different shapes of magnetic particles known, including spheres, cubes, ellipsoids, platelets, and cylinders/rods. An ideal example of isotropic particle geometry are spherical nanoparticles which are one of the most heavily researched in the field of magnetism, specifically iron oxide spherical nanoparticles as they are easily obtained according to reproducible experimental procedures[23,24]. When comparing spherical nanoparticles with cubic nanoparticles of the same composition and size, it has been reported that there is a large difference in coercivity between the two shapes[25]. This can be attributed to surface pinning which occurs due to missing coordinating oxygen atoms. Researchers compared $CoFe_2O_4$ cubic and spherical nanoparticles and hypothesised that cubic $CoFe_2O_4$ has fewer missing oxygen atoms and hence less surface pinning, possibly leading to lower coercivity for the cubic structures. On the other hand, cubic nanoparticles are found to have a higher saturation magnetisation than spherical nanoparticles of the same volume[26]. This disparity is believed to be a result of lower disordered spins in cubes giving a higher saturation, although this is not a universal observation[27].

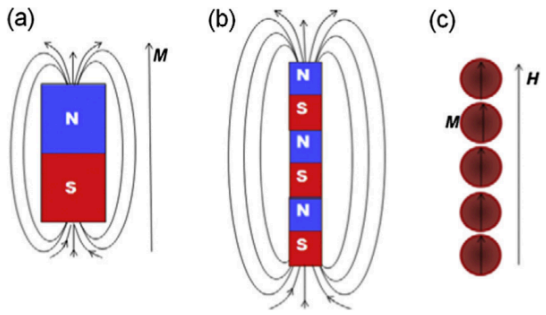

Figure 10: Schematic display of a bar magnet (a), and an elongated magnetic particle shown as an array of small magnets (b), as well as a magnetic nanochain (c)[21].

Interest in the synthesis routes of anisotropic nanoparticles which differ from the isotropic spherical shape is prevalent. In contrast to spherical particles, materials with an anisotropic shape display direction – dependent properties, high surface – to – volume ratio and particular crystal facets at the surface that can exhibit different reactivity[28]. Magnetic nanoparticles with a nanorod, nanowire, nanotube and ellipsoid geometry fall in the category of elongated anisotropic magnetic nanoparticles. Nanorods have diameter in the order of few nanometres and length up to 100 nm, nanowires have similar diameter but are much longer, while nanotubes are hollow nanorods. The shape of these elongated particles is determined by the synthesis method and generally composes Fe and Co alloys, as well as some Fe oxides. Elongated magnetic nanoparticles have several features which make them useful in the field such as, a strong shape anisotropy and being able to easily align when exposed to an external magnetic field[29,30]. Elongated magnetic nanoparticles can be presented as a magnetic bar made up of an array of small magnets aligned along the long axis as shown in **Figure 10**. This configuration is energetically most favourable as the magnetisation is parallel to the particle surface for the majority of its length[8]. The shape anisotropy of elongated nanoparticles determines the direction of the magnetisation along their long axis and the demagnetisation factor increases with the shape anisotropy. However, elongated particles with a size aspect ratio above 10,[31] the demagnetisation factor already approaches the maximum value possible. As a result, the M_s value also significantly affects the demagnetisation field of the elongated magnetic nanoparticles with a high aspect ratio (>10). Due to the shape anisotropy, elongated magnetic nanoparticles exhibit an anisotropic response to an applied field, i.e. a square – like hysteresis loop is observed when

magnetic field is applied parallel to the particle's long axis with a large coercivity and M_s = M_r. Conversely, when a field is applied perpendicular to the particle's long axis, an S – like response is observed with no hysteresis.

Plate – like magnetic nanoparticles in the form of thin disks or plates are also considered anisotropic. A well – known example of these are hexaferrites which crystallize and grow in a highly anisotropic structure. Otherwise, Co nanodiscs[32], Fe_3o_4 nanopaltes@graphene[33] and magnetic nanosheets composed of 2D ordered assemblies of superparamagnetic nanoparticles[34] are all examples of particles that can have a platelet geometry. The magnetisation of plate – like magnetic nanoparticles in a soft magnetic material lies within the basal plane and easily realigns in the basal plane. However, a stronger magnetic field is needed for the realignment of their magnetisation out of the plane. In contrast, plate – like particles incorporated in materials exhibiting a strong uniaxial magnetocrystalline anisotropy, such as hexaferrites, have a magnetic easy axis perpendicular to the basal plane. This strong uniaxial magnetocrystalline anisotropy is dominate over the shape anisotropy effect on the particle's magnetisation and hence a large magnetic field is required to realign the magnetisation in any other direction. The plate – like magnetic nanoparticles with a strong uniaxial magnetocrystalline anisotropy behave in the opposite way to an elongated magnetic nanoparticle or a typical soft – magnetic plate – like particle when exposed to a magnetic field. They show a square – like hysteresis loop when the applied magnetic field is perpendicular to the basal plane with the largest H_c, M_r and M_s in this orientation. The hysteresis of these plate – like magnetic nanoparticles decreases as the angle between the nanoparticle's plane and the magnetic field decreases. Eventually, H_c, M_r and M_s become zero for a single plate – like nanoparticle as the direction of the magnetic field is in the plane of the nanoparticle[21].

1.9.2. Hard, anisotropic magnetic nanoparticles

Hard magnetic nanoparticles and their specific response to a magnetic field is extremely relevant to the materials discussed in this thesis. Although soft magnetic materials excel in applications where rapid magnetisation and demagnetisation with minimal energy loss is required, hard magnetic materials and their characteristic response to an applied magnetic

field are of particular relevance to the materials examined in this thesis. Typical applications include permanent magnets used in data storage, magnetic sensors, and actuator systems. Once magnetised by applying a field $H \geq M_s$ sufficient enough to saturate the magnetisation, a hard magnetic material will remain in a magnetised state even after the field is removed. The high coercivity of hard materials compared to soft materials, makes them much more suitable for applications where the ability to resist demagnetisation is required, such as permanent magnets. Additionally, anisotropic hard magnetic nanoparticles are extremely unique in their magnetic behaviour in comparison to isotropic or spherical particles due to their direction – dependent chemical and physical properties. Intrinsic magnetic properties such as ferroelectricity, piezoelectricity, pyroelectricity, non – linear optical behaviour, circular dichroism, Faraday rotation, electromagnetic non – reciprocity, magnetic anisotropy, anisotropic mechanical properties, and anisotropic crystal growth all originate from the structural anisotropy of specific materials.

One such example of single – domain, anisotropic magnetic nanoparticles with hard properties are barium hexaferrites (BHF). The research findings presented in this thesis centres around the synthesis and characterisation of BHF nanoparticles due to their highly applicable anisotropic and hard magnetic properties. Their hexagonal platelet morphology and preferred growth in the ab direction provides a high aspect ratio and high demagnetisation factor compared to other magnetic geometries, making them a stable magnetic state. BHF nanoparticles exhibit a uniaxial magnetic anisotropy with the easy axis perpendicular to the platelet, which is a crucial property for the effective alignment of the dispersed BHF nanoparticles in an applied magnetic field. In comparison to spherical or rod-shaped nanoparticles which have a low aspect ratio and low magnetocrystalline anisotropy, BHF nanoparticles have a large magnetocrystalline anisotropy which is a prerequisite for a high coercivity, making it a very magnetically hard material suitable for permanent magnets. Furthermore, the ability to substitute large cations into the BHF unit cell makes BHF nanoparticles flexible structures that can easily incorporate ions during the synthesis process. This also means the size and magnetic properties of BHF nanoparticles can easily be controlled for many different applications[21]. The geometry, unit cell and magnetic behaviour of BHF nanoparticles is introduced in more detail in chapter 2.

To conclude chapter 1, it was important to firstly introduce basic parameters of magnetism and magnetic terms to understand their contribution towards nanoparticle behaviour. The central focus of this chapter is on the properties of dry magnetic particles and more importantly, the effect of particle anisotropies such as geometry and size. The concepts in this chapter establish a foundation for chapter 2 which introduces the Barium hexaferrite magnetic nanoparticles which are an integral part of the research described in the following chapters due to their unique anisotropic properties. Chapter 2 also describes the various synthesis methods commonly used to produce dry magnetic particles discussing the advantages of each technique and the factors that make some synthesis techniques more favourable.

Chapter 2: Synthesis and Colloidal Dispersion of Barium Hexaferrite Nanoparticles

Chapter 2 provides a comparative analysis of different synthesis methods for magnetic particles, with particular emphasis on their suitability for producing dry barium hexaferrite particles. The choice of synthesis route has a decisive influence on particle size, morphology, and dispersibility in solvents, all of which govern the resulting colloidal stability. Selecting an appropriate method is therefore critical to tailoring BHF particles for their intended applications.

2.1. Barium hexaferrites platelet magnetic nanoparticles

Hexaferrites are magnetic nanoparticles which grow in a platelet morphology. These are complex oxides usually composing a large bivalent cation such as Ba or Sr, and a bivalent transition metal. Hexaferrites have a highly anisotropic structure based on the mineral magnetoplumbite and have recently gained a lot of interest in the nanomagnetic field. Their ferromagnetic/ferrimagnetic properties, excellent chemical stability, mechanical hardness, and corrosion resistant make them suitable for a range of different applications[35]. Although the synthesis of numerous structural and chemical polytypes with different magnetic

behaviours is possible, the synthetic process is extremely challenging for some types of complex hexaferrites.

Table 2: shows some physical and thermal properties for SrM, BaM and PbM polycrystalline M ferrites. δ is density, T_m is melting point, the a and c axis are lattice parameters and v = cell volume from XRD. T_c is Curie temperature from standard molar heat capacity[35].

Material	δ (g cm^{-3})	T_m (K)	a (Á)	c (Á)	v ($Á^3$)	T_c (K)	Area of application
$SrFe_{12}O_{19}$[36]	5.101	1692	5.8844	23.0632	691.6	732	Electric motors
$BaFe_{12}O_{19}$[37]	5.295	1611	5.8876	23.1885	696.2	725	Bioimaging
$Ca_{0.5}Pb_{0.4}Yb_{0.1}Zn_{1.0}Fe_{11}O_{19}$[38]	5.708	1538	5.8941	23.0984	694.9	718	Photocatalyst

The simplest type of hexaferrites are M – type hexaferrites and they can be differentiated from other Y-, Z-, and Co-W types which have a planer magnetocrystalline anisotropy and require a large magnetic field to realign the magnetisation perpendicular to the basal plane, whereas the magnetisation of M – type hexaferrites lies perpendicular to the basal plane. The physical and thermal properties of some common polycrystalline M – type hexaferrites are compared in **Table 2.** It is important to note that both M – type strontium hexaferrites (SrM), $SrFe_{12}O_{19}$ and barium hexaferrites (BHF), $BaFe_{12}O_{19}$ have similar properties due to their magnetoplumbite crystal structure and hexagonal platelet morphology. Additionally, both BHF and SrM possess high uniaxial magnetocrystalline anisotropy, however, SrM typically display a large shape anisotropy, i.e. larger aspect ratio compared to BHF which can often result in a lowered coercivity as the two anisotropy fields oppose each other. For the purpose of this thesis, the discussion hereafter is restricted to BHF particles[39].

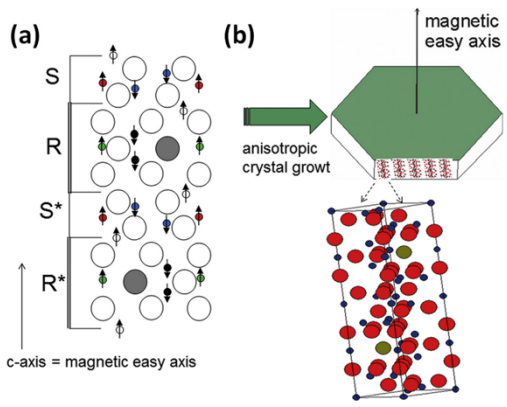

Figure 11: 2D presentation of the BHF unit cell structure where the large empty circles represent O^{2-}, large grey circles represent Ba^{2+} and small circles represent Fe^{3+}. Arrows denote directions of the magnetic moments of Fe^{3+} ions (a). A hexaferrite platelet particle with arrow showing magnetic easy axis (b)[21].

BHF anisotropic nanoparticles have been widely used as hard magnetic materials for permanent magnets since the beginning of their introduction by Philips[40]. These are ferrimagnetic particles with the basic chemical formula $BaFe_{12}O_{19}$ and a hexagonal platelet morphology. The magnetic properties of BHF particles arise from the interactions between metallic ions occupying particular positions relative to the oxygen ions in its hexagonal crystalline structure. It is important to understand the unit cell structure of BHF particles which is made up of two S and two R blocks, RSR*S*, where * denotes a rotation of 180° around the c – axis. The S block is a slice of a spinel structure in the [1 1 1] direction with two layers of cubic close – packed O^{2-} ions and Fe^{3+} ions which occupy the tetrahedral and octahedral sites. The R block is composed of three close – packed O^{2-} layers with the middle one containing Ba^{2+} in the place of one O^{2-}. This substitution with Ba^{2+} makes the R block become hexagonally close packed. The Fe^{3+} in the chemical structure occupies three crystallographic sites in the R block, including a bi – pyramidal site, octahedral sites in the R block interior and octahedral sites at the R – S interface. This hexaferrite unit cell structure is illustrated in **Figure 11**.

The BHF lattice structure is extremely flexible and allows for the incorporation of larger cations as a means to control particle size, size distribution and hence their magnetic properties. Typically, a variation of lanthanide (Ln^{3+}) ions are incorporated into the chemical structure for this purpose. For BHF nanoparticles, the Fe^{3+} ions in the unit cell is partially substituted for a larger cation, typically being In^{3+} or Sc^{3+}. This has shown to significantly narrow down the size distribution in BHF nanoparticles synthesised hydrothermally[41] by blocking secondary re – crystallisation or Ostwald ripening effect. For the specific case of BHF nanoparticles, it has been found that this chemical substitution of Sc^{3+} has the opposite effect on the magnetic properties of nanoparticles compared to the bulk. Previously it was suggested that substituting diamagnetic Sc^{3+} ions in BHF dilutes the magnetic Fe^{3+} ions, lowering the M_s[42]. However, when the Sc^{3+} ions substitute the Fe^{3+} ions in thin platelet shaped hexaferrite nanoparticles, the M_s value increases substantially. The M_s value was

shown to increase from 16 Am^2/kg in unsubstituted nanoplatelets to over 38 Am^2/kg in substituted BHF nanoparticles[43]. This substitution of large cations into the BHF unit cell has proven to be more successful for controlling size and size distribution of BHF magnetic particles as compared to other methods such as ligand – exchange which substantially lower the synthesis yield.

2.2. Coprecipitation

The synthetic route represents the most important step in the design of a nanoparticle used for a specific application, as it will determine the particle size/shape, the size distribution, the surface chemistry of the particles, and consequently their unique properties[44]. There are many routes for the synthesis of magnetic nanoparticles[45], one commonly used method is coprecipitation.

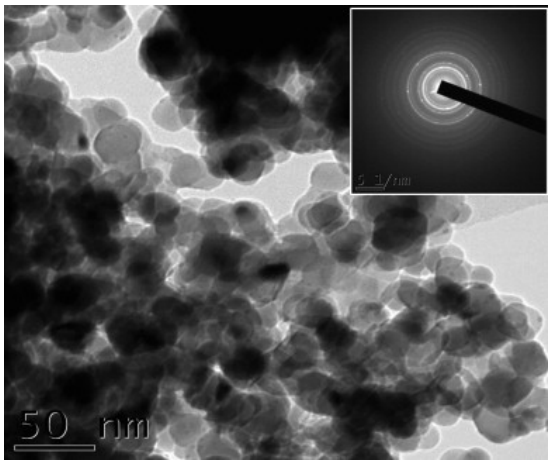

Figure 12: TEM image of $NiFe_2O_4$ nanoparticles prepared by co-precipitation route annealed at 1000 °C for 10 h[46].

Coprecipitation is a simple and convenient method for synthesising magnetic nanoparticles from aqueous salt solutions through the addition of a base as a precipitating agent at room temperature or at elevated temperatures. This method can be used to produce different shapes and compositions of magnetic particles. Coprecipitation has been used to synthesise ferrites since the early 1960s[47] such as nickel ferrite nanoparticles using stable ferric and nickel salts with sodium hydroxide as the precipitating agent[46]. **Figure 12** shows the Transmission Electron Microscopy - TEM image of $NiFe_2O_4$ nanoparticles prepared by co-precipitation. Additionally, coprecipitation is often used for the preparation of fine hexaferrite powders and can also be optimised for large – scale production. However,

powders produced using coprecipitation usually present inhomogeneity in particle size and microstructure due to the concentration gradient during the coprecipitation process and agglomeration as precursors are precipitated. Researchers have tried to overcome this major disadvantage by investigating the coprecipitation of BHF nanoparticles and the influence of varying parameters on its formation[48]. The process of BHF synthesis using coprecipitation methods can be described by the equations below. The A in these equations can represent a chloride, acetate, or nitrate group, a denotes the amorphous state, while the other phases are crystalline, the temperature ranges between 500 – 800 °C depending on the reaction conditions and, note that T1 < T2 < T3. The variables u, v, z, x, y are in the range of 0 – 1.

$$BaA_2 + 12FeA_3 \xrightarrow{NaOH,H_2O,alcohol} Ba(OH)_2(a) + 12FeO_x(OH)_y(a) \qquad (18)$$

$$Ba(OH)_2(a) \xrightarrow{air} BaCO_3 \qquad (19)$$

$$(1-v)Ba(OH)_2(a) + vBaCO_3 + 12FeO_x(OH)_y(a) \xrightarrow{T_1,-H_2O(g),-CO_2(g)}$$
$$5(1-u)(1-z)\alpha - Fe_2O_3 + 5u(1-z)\gamma - Fe_2O_3 + (1-z)BaFe_2O_4 + zBaFe_{12}O_{19} \qquad (20)$$

$$5u(1-z)\gamma - Fe_2O_3 \xrightarrow{T_2} 5u(1-z)\alpha - Fe_2O_3 \qquad (21)$$

$$5(1-z)\alpha - Fe_2O_3 + (1-z)BaFe_2O_4 \xrightarrow{T_3} (1-z)BaFe_{12}O_{19} \qquad (22)$$

Equations (18) and (19) outline the product of $BaCO_3$ by – product as well as the Ba and Fe precursors used to initiate equation (20). The variables in equation (20), x, y and z, depend on the reaction conditions such as type of alcohol, type of reagent salts, coprecipitation atmosphere, temperature and time of calcination. In general, z increases with the length of the alcohol chain and with the calcination temperature and time. It was found that if the coprecipitation reaction was carried out in argon or from chlorides, the intermediate phase, $BaFe_2O_4$ can be avoided (z = 1). Additionally, it was concluded that the major amount of $BaFe_{12}O_{19}$ (BHF) formed up to 600 °C, however, the formation of BHF is not complete even after 10 h at 600 °C. This confirms that the formation of BHF using this method involves two competitive mechanisms (equations 20 and 22)[49].

The synthesis of BHF nanoparticles has also been conducted under atmospheric oxygen to protect the oxidation of certain nanoparticles and hence the production of by - products.

The main advantage of using this method over others is that the precipitation process allows for a high yield of nanoparticles to be synthesised reasonably fast and there is no need for extra mechanical or microwave heat treatment. However, a significant downside here is the lack of control on particle size distribution as only kinetic factors are controlling the particle growth[50]. The coprecipitation reaction also uses high temperature processes at long periods of time which can be more energy and time consuming compared to other methods. However, this issue is recognised by researchers that have studied a possible low temperature coprecipitation synthesis of BHF nanoparticles from ethanol solutions instead of water solutions[51].

2.3. Sol – gel synthesis

Another route for the synthesis of magnetic nanoparticles is a wet – chemical process called sol – gel based on hydrolysis and polycondensation methods[52,53].

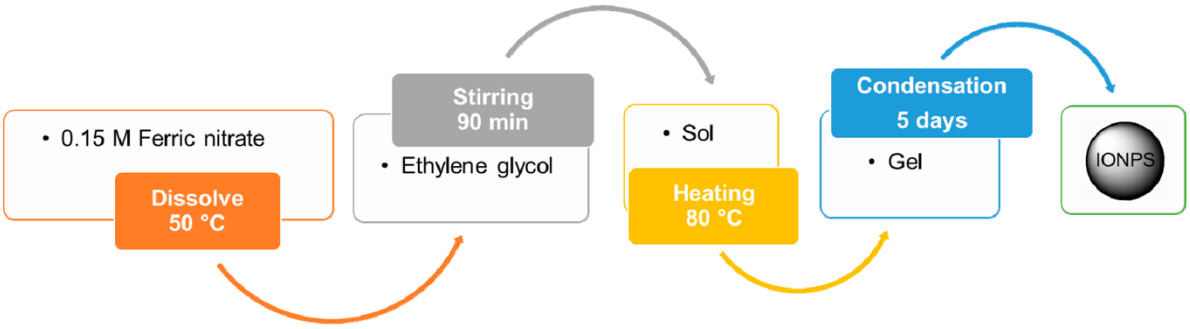

Figure 13: Flowchart for the sol – gel synthesis of iron oxide nanoparticles[52].

This process mixes precursors, which can be inorganic or metallo – organic, forming a colloidal solution of nanoparticles ("sol"). The material is further dried ("gel" formation) removing the solvent and condensed to a gel subsequently producing fine-grained polycrystalline ferrites with a narrow size distribution. This method of magnetic nanoparticle synthesis has been used for a range of different compounds and is a popular synthesis route in many areas of research. **Figure 13** shows a flowchart for the synthesis of iron oxide nanoparticles using sol – gel method. Sol – gel proves to be an advantageous method for the synthesis of magnetic nanoparticles as the process is economically and environmentally friendly. The method allows for control over particle size by changing the annealing temperatures, a higher average mean particle size is reported as the annealing temperature

increases. Additionally, it is claimed that morphology of the magnetic particles can be controlled when synthesised at specific temperatures[53]. Sol – gel has also been used to produce hexagonal ferrites by Pullar et al. Researchers developed a novel aqueous sol – gel synthesis route for the preparation of hexagonal ferrites from stoichiometric precursors[54]. Ferrites composing Sr[55] and Co[56] are commonly produced using sol – gel method.

Sol – gel method is commonly reported for the production of BHF nanoparticles, and it has been shown that the ratio of precursors used in this method to make BHF is extremely important. To be specific, a ratio of Fe:Ba of 10.5 produced BHF at 900 °C/1 h with grain size of only 200 nm[57]. The barium rich precursor yields pure BHF without any α-Fe_2O_3 as a second phase, however, a Fe:Ba ratio of less than 9 produces $BaFe_2O_4$ as a second precursor instead[58], indicating that there is a narrow compositional window for the formation of single phase BHF using this method. With a fixed Fe:Ba ratio, the formation of BHF from either nitrate or hydroxide sol – gel precursors were also investigated. It was found that the presence of a nitrate anion was important for the formation of the intermediate phases, α-Fe_2O_3 and $BaFe_2O_4$ over a wide range of temperatures. These non-magnetic phases can then be eliminated by preheating the gel to 450 °C/5 h to remove any organic compounds. BHF subsequently forms at 750 °C but the optimal magnetic properties were obtained at 950 °C [59]. Sol – gel method is a reasonably good choice for the synthesis of magnetic materials as it produces a monodisperse sample with control of microstructure, desired shape and size with high purity and good crystallinity of the products. However, the process involves prolonged reaction times, using toxic organic solvents and high chance of product contamination[60].

2.4. Hydrothermal synthesis

Hydrothermal synthesis is another reliable route for producing magnetic particles. Hydrothermal synthesis is one of the most commonly used methods for the preparation of magnetic particles[61]. This synthesis process can be used to prepare nanostructures and single – crystal materials with well – defined size and morphology for their specific applications. It can also be used for the crystalline growth of several inorganic compounds

and the synthesis of new phases or stabilisation of new complexes. It has been described as the most efficient method for the formation of nanocrystals as it exploits the solubility of some inorganic substances at specific reaction conditions. This supports the crystallisation of the dissolved precursors within the medium as the reaction conditions like temperature and pressure hugely affect and maintain the nucleation and distribution of particles[62]. The main process involves a precipitation of particles in solution followed by heating to initiate particle growth. The nanoparticles can be grown in a wide temperature range from room temperature to extremely high temperatures. This technique typically makes use of an autoclave to reach high temperatures and pressures. Researchers have used hydrothermal synthesis extensively for the production of particles such as Fe_3O_4 and even attribute the narrow size distribution of the particles to the hydrothermal synthesis used[63]. This method has also been reported to allow more control on the particle diameters and as a result researchers are able to tune the particle magnetic properties[64]. One advantage of this synthesis method is that it has been reported to give better morphological results with various shapes of Fe_3O_4 nanoparticles being made using hydrothermal synthesis, such as spheres, cubes and wires.

Hydrothermal synthesis allows the morphology of the particles to be controlled by adjusting the reaction temperature, solvent type, precursor salt, reducing agent or pressure conditions depending on the vapour pressure of the main composition in the reaction mixture. Torres – Gomez et al[61] presents a simple and efficient way to produce pure phase magnetite nanoparticles using hydrothermal synthesis and subsequently tune the morphology of the nanoparticles by changing the reaction temperature. The end product was pure phase Fe_3o_4 nanoparticles with a high level of crystallinity and uniform morphology at each temperature. The resulting shapes of the nanoparticles were shown to be quasi- sphere, octahedrons, and cubes with good saturation magnetisation. Cursaru et al[45] reported the physical – chemistry properties of magnetite particles produced using the hydrothermal method and found that crystallite size increases with increasing pressure and temperature with the hydrodynamic diameter only being affected by temperature. It is also important to note that the crystal formation depends heavily on the minerals in water, proper mixing of solvent and duration of mixing[65]. The majority of research into hydrothermal synthesis of hexagonal ferrites concentrated on M ferrites. It has been a particularly successful and popular method for BHF

nanoparticles often pure phase BHF nanoparticles are hydrothermally made from stoichiometric mixtures of iron and barium. Some researchers describe poor crystallinity of the product and include an additional annealing step at approximately 900 °C to allow the Ba^{2+} ions to diffuse fully from the surface into the M lattice[66]. Often the formation of $BaCO_3$ side product is reported when ratio below Fe:Ba = 10 is used during hydrothermal synthesis. This impurity forms as the barium reacts with CO_2 in the air during the reaction. Many factors and their effect on the BHF synthesis using this method have been studied to produce single phase BHF[67]. Factors such as the phase of Fe_2O_3 used in the process, ratio of precipitating agents, ratio of Fe to Ba, synthesis temperature and time are all considered. Liu et al[67], has studied these effects in detail and report that a Fe:Ba ratio, OH^- : NO^{3-} ratio of 2 and a reaction temperature of 230 °C/48 h was required for the best quality single phase BHF particles. Having said this, researchers will often adjust the reaction conditions to the feasibility of starting materials, size, and morphology of BHF particles needed.

To conclude, hydrothermal synthesis is an economical simple method and produces particles with high crystallinity, consistent composition and has a good control on the particle size and shape offering magnetic tuning and easy dispersion of the particles. However, the main disadvantage of hydrothermal synthesis is the need for high temperatures and pressures which requires expensive facilities. It is also more difficult to produce nanoparticles smaller than 10 nm using this method with slow reaction kinetics at high temperatures.

2.5. Chemical Reduction

Chemical reduction is a nanoparticle synthesis method which uses chemical – reducing agents. The substrates used in this method can be either natural compounds from plants or microorganisms or reagents/chemical reducing agents. The main chemical method used here for the synthesis of nanoparticles is the reduction of metal ions in solution. The same approach was used in early 1857, to produce colloidal gold using chemical reduction[68,69]. The metal ions can be reduced in both aqueous and organic solvents, while organic solvents are preferred since metal nanoparticles are particularly sensitive to oxidation[70]. It is also possible to control the size, shape, and size distribution of the particles by altering reaction

parameters[71]. The reduction of salts of a selected metal is done in the presence of a stabilizer[72] which protects the metal nanoparticles from assembling into larger aggregates. The first step of a chemical reduction process typically involves a redox reaction, whereby, electrons from the reducing agent are transferred to the metal atoms (equation 23), resulting in the formation of free metal atoms:

$$Metal^{n+} + n\ electrons^{-} = Metal^{0} \qquad (23)$$

This is followed by a nucleation process where the free metal atoms collide with one another and form stable nuclei. And finally, stabilizers are added in the last stage to allow for dispersion. This is a cost – effective, ecologically, and economically friendly method as the magnetic nanoparticles can be produced without the need for high temperatures and can also be used for a variety of metals[73]. Although this is not a popular route for the synthesis of barium hexaferrite nanoparticles, it is heavily used to manufacture iron based magnetic particles such as, FeCo which can be synthesised by simultaneous co – reduction of ferrous sulfate and cobalt chloride salts using sodium borohydride (equation 24)[74]:

$$FeSO_4 + CoCl_2 + 2NaBH_4 \rightarrow FeCo + 2NaCl + Na_2SO_4 + 2B + 4H_2 \qquad (24)$$

In addition, monodisperse ε-Co nanoparticles have also been prepared via the reduction of cobalt chloride using this method[75,76].

2.6. Pulsed Laser Ablation in Liquid (PLAL)

Apart from the chemical methods mentioned above, physical methods of magnetic particle synthesis are also commonly reported in literature. Pulsed Laser Ablation in Liquid (PLAL) is a physical synthesis method which is distinguished in terms of ease of particle production, and effectiveness in controlling particle size distribution. The PLAL synthesis method starts by directing a high – energy optical source (pulse laser radiation) in the perpendicular direction towards the solid bulk metal target submerged in a liquid medium, the laser source can also be directed from the top of side. Once the laser interacts with the metal, a series of

thermodynamic reactions occur. As the nanoparticles are synthesised in liquid, colloidal nanoparticles can be obtained faster compared to other synthesis methods. Pulsed laser ablation can also be performed in other mediums such as, air and vacuum[77,78], however, the use of a liquid medium is much more popular and has shown a prominent effect on the structural formation of nanoparticles[79].

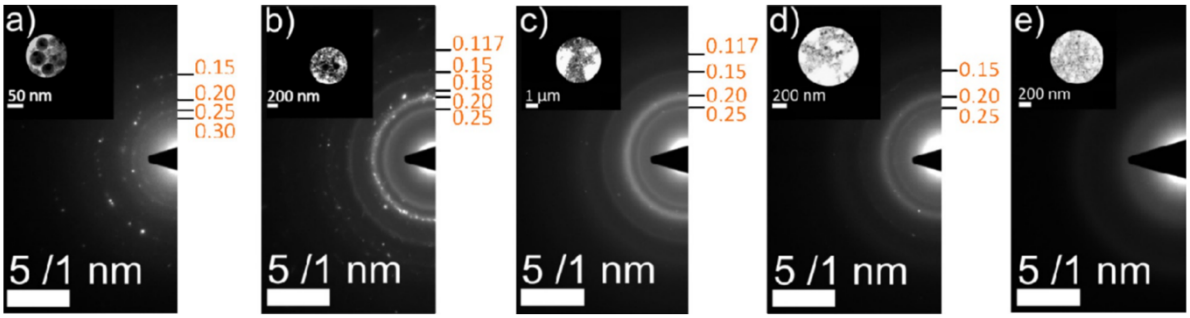

Figure 14: SAED analysis of nanoparticle ensembles generated in a) water, b) methanol, c) ethanol, d) acetone, and e) toluene.

PLAL was initially used to synthesise iron oxide nanoparticles by Patil et al[80] and, since then, it has been used for several different types of metallic nanoparticles applied in various commercial industries such as food, biomedical, electronics and optical. Several researchers investigated the production of iron based magnetic nanoparticles in different solvents and found that a variety of nanomaterials can be created using PLAL given the laser parameters and liquid solvents used[81]. **Figure 14** shows the Selected Area Electron Diffraction (SAED) analysis of iron – based nanoparticles, the results show that the nanoparticles become more amorphous as the carbon content of the liquid solvent increases. In addition, several reports of magnetic nanoparticles synthesised using PLAL have been published including the ablation of Co in water and ethanol[82,83] as well as magnetic alloys (such as Sm – Co and Ni – Fe) in cyclopentanone[84]. The Meunier group reported the production of core – shell structures with a diameter of 6.5 nm by irradiating a suspension of Au and Co nanoparticles[85], while Zeng et al[86] were able to produce FeO nanoparticles by ablation of an iron target in a water/poly(vinylpyrrolidone) solution. All the above reports synthesised magnetic nanoparticles which can be removed out of solution by a permanent magnet.

PLAL is a highly efficient method for the preparation of surfactant free stable nanofluids and has been recently explored for the synthesis of barium hexaferrite nanofluids. Although PLAL is an unpopular synthesis route for barium hexaferrite nanofluids, studies indicate that the nature of the solvent has a great influence on the nanoparticle size and optical properties of the resulting nanofluid. Hence, further optimisation of the PLAL process allows greater control on the size, morphology and magnetic properties of the particles. PLAL has several advantages over other methods, such as, reduced reaction time, absence of reducing agents, low toxicity, the process does not include a multistep synthesis, and the ease of product extraction as the nanoparticles are confined within a liquid zone. The process does not require any chemicals and thus eliminates the need for time – consuming purification steps and is relatively safe compared to other wet chemistry methods. It is also a contamination – free technique unlike conventional chemical methods where surfactants, catalysts, by – products, and ions are involved[87].

2.7. Microwave Irradiation

Microwave irradiation is a widely explored method for the synthesis of many different materials. The microwaves are electromagnetic waves with commercially used microwaves working at a frequency of 2.45 GHz. The microwave heating provides a fast transfer of energy through radiation rather than typical heat transfer methods or convection. This ensures a fast penetration of energy into the volume of materials transparent to microwave radiation. The nanoparticles are prepared in solvents such as water and organic solvents, polyols are especially popular due to their capability to act as both a reducing agent and solvent. The main advantage of this method is that it considerably reduces the reaction time of organic synthesis as well as increase yields and decrease energy and reagent consumption[88]. The use of microwaves for the production of nanoparticles is recently emerging and has many benefits, one of which is particularly important for nanoparticle synthesis - homogenous heating[89]. The use of microwaves ensures a uniform distribution of the heat in solution compared to traditional heating methods which tend to be more heterogenous and focused on the reaction flask walls. Homogenous heating of the solution allows for a narrow size distribution and controlled physiochemical properties in the

nanomaterial. This was shown by Seol et al[90], who studied the microwave – assisted synthesis of Au colloidal nanoparticles with diameters of 12 nm with a reaction time of a few minutes. They found that using high microwave power to increase the temperature ramping rate enables homogenous nucleation and particle growth, which reduces nanoparticle size and improves uniformity. Many have also synthesised Au nanoparticles using microwave irradiation method for biological applications[91,92]. Additionally, materials composing other metallic nanoparticles, such as Pt nanoparticles in aqueous solution[93], have been successfully produced by microwave irradiation for their use catalysis. This synthesis method has been described as highly efficient, energy – saving, and environmentally friendly in many chemical processes. Microwave irradiation methods have been used in conjunction with hydrothermal synthesis for the purpose of producing fine particles of barium ferrite[94]. The microwave – induced hydrothermal methods have been studied on various spinel ferrites, however, the mechanism for hexagonal barium hexaferrite is different from that of spinel ferrites as barium ferrite is formed through the intermediate phases of α-Fe_2O_3 and $BaFe_2O_3$. Using microwave irradiation methods, the crystallisation of the barium ferrite particles is promoted within a short time and rapid formation also supresses particle agglomeration. However, the thickness of the barium hexaferrite nanoparticles were found to be unusually low, causing a larger aspect ratio compared to conventional hydrothermal methods[95].

2.8. Summary of particle synthesis methods

Table 3: Summary and comparison of different particle synthesis methods.

Particle Synthesis Method	**Method summary**	**Advantages**	**Limitations**
Co – precipitation	Synthesis of magnetic nanoparticles from aqueous salt solutions through the addition of a base as a precipitating agent.	- Simple and convenient. - Can be optimised for large – scale production. - High yield of products.	- Inhomogeneity in particle size and microstructure. - Lack of control on particle size distribution. - Use of high temperature.
Sol – gel synthesis	Mixing of precursors forming a colloidal solution	- Economically and	- Prolonged reaction times.

	(“sol”) which is later dried (“gel”) producing fine-grained polycrystalline ferrites.	environmentally friendly - Monodisperse sample obtained. - Control of shape, and size. - High purity and good crystallinity of products.	- Use of toxic organic solvents. - High chance of product contamination.
Hydrothermal synthesis	Precipitation of particles in solution followed by heating to initiate particle growth.	- Economically friendly method - Produces particles with high crystallinity and consistent composition. - Control on the particle size and shape offering magnetic tuning	- Need for high temperatures and pressures. - Difficult to produce nanoparticles smaller than 10 nm.
Chemical reduction	Reduction of metal ions in solution to produce nanoparticles.	- Control of particle size, shape, and size distribution. - Cost – effective. - Ecologically, and economically friendly.	- Mainly used for iron oxide particle synthesis, limited research on BHF particle production.
Pulsed Laser Ablation in Liquid (PLAL)	Physical synthesis method initiated by directing a high – energy optical source towards a bulk metal target submerged in liquid which triggers thermodynamic reactions to occur.	- Control of particle size and shape. - Can be performed in other mediums such as, air and vacuum. - Reduced reaction time. - Low toxicity. - Ease of product extraction.	- Limited research on BHF particle production.

Microwave irradiation	The microwave heating provides a fast transfer of energy through radiation rather than typical heat transfer methods or convection. The nanoparticles are prepared in solvents such as water and organic solvents.	- Reduced reaction time. - Increased yield. - Decreased energy and reagent consumption. - Environmentally friendly.	- Less on control on particle size and shape.

Chapter 3: Colloidal Stability of Barium Hexaferrite Ferrofluids

Chapter 3 introduces ferrofluids and magnetorheological fluids which are typically produced after dispersing dry magnetic nanoparticles in an appropriate solvent or wet dispersed during the synthesis process. Colloidal stability is defined as the ability of suspended particles to remain uniformly dispersed over time without aggregation or sedimentation. For barium hexaferrite nanoparticles, magnetic dipole–dipole interactions act in addition to van der Waals forces, both of which promote particle attraction and aggregation. This chapter therefore examines how these interactions can be mitigated through the use of stabilising agents, ensuring long-term stability and functionality of BHF-based suspensions.

3.1. Fundamentals of Stability in Colloidal Ferrofluids

The content of Subchapter 3.1 is based on reference 97, namely “Ferrohydrodynamics” by R.E. Rosensweig.

3.1.1. Colloidal ferrofluids

Ferrofluids are a group of colloidal magnetic fluids composing homogenously dispersed particles suspended in a carrier fluid. A colloidal system can consist of evenly suspended particles in a continuous medium as well as suspensions that settle out slowly. However, a true ferrofluid does not settle out despite a slight concentration gradient which is often established after long exposure to a force field (gravitational or magnetic).

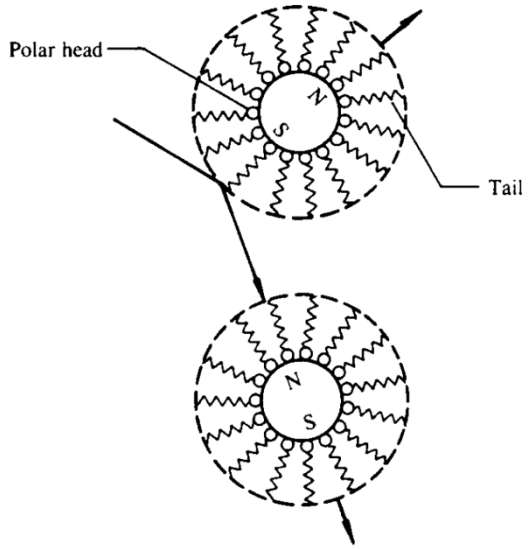

Figure 15: magnetic, single - domain particles with a surface coating of surfactant molecules in a colloidal ferrofluid[96].

Ferrofluids are composed of small (up to a few nanometres) particles of solid, magnetic, single – domain particles which are typically coated with a molecular layer of a dispersant and suspended in a non – magnetic liquid carrier fluid (**Figure 15**). The molecular layer coating is often a stabilising agent adsorbed onto the particle surface and has a principal role of preventing the particles from sticking or aggregating together. In addition, thermal agitation keeps the magnetic particles suspended in the carrier fluid due to Brownian motion. These ferrofluids are vastly different from the 'magnetic fluids' for clutches and brakes introduced in the late 1940s which compose of micron – and larger sized iron particles slurried in an oil. These clutch fluids solidify in the presence of an applied magnetic field while colloidal ferrofluids retain liquid flowability even when exposed to intense magnetic fields. A typical ferrofluid contains 10^{23} particles per cubic meter and is opaque to visible light[96]. Ferrofluids also differ significantly from magnetorheological fluids (MRFs) in terms of composition, particle size, and rheological behaviour. MRFs typically compose of multidomain particles, usually in the micrometre size range which are prone to

sedimentation. This difference in particle size leads to distinct magnetic and flow properties. When exposed to external magnetic field, MRFs undergo a reversible transition from a liquid to a semi – solid state, accompanied by a dramatic increase in viscosity which is not observed in ferrofluids[97].

3.1.2. Fundamentals of stability

The properties of a ferrofluid are largely affected by the Brownian motion of the dispersed particles as well as the magnetisation of each sub – domain particle. Brownian motion is a thermal effect (above 0 K) that describes the random movement of particles suspended in a liquid or gas. A third essential component of a colloidal ferrofluid is a long – chain molecular species which is typically adsorbed onto the magnetic particle surface. This long – chain molecule prevents agglomeration of the particles to each other by introducing repulsive interactions. It is essential to maintain the stability of colloidal systems like ferrofluids, as it ensures a well – defined material suitable for fluid applications and scientific studies.

It is useful to consider the simple physics of the mechanisms that are responsible for the stability of ferrofluids. To begin, the different energy contributions acting on an individual particle include:

$$\text{thermal energy} = kT$$

$$\text{magnetic energy} = \mu_0 MHV$$

$$\text{gravitational energy} = \Delta_\rho V g L$$

where k is Boltzmann's constant and equals 1.38×10^{-23} J K^{-1}, T is the absolute temperature in degrees Kelvin. μ_0 is the permeability of free space and has the value $4\pi \times 10^{-7}$ H m^{-1}, Volume $V = \pi d^3/6m^3$ for a spherical particle of diameter d, and L is the elevation in the gravitational field. Differentiation in the ratio of one term to another yields dimensionless quantities that can alter the stability of the ferrofluid.

3.1.3. Magnetic field effects on stability

To evaluate the stability of magnetic particles settling in a field gradient due to an external magnetic source, it is important to consider the competing influences acting on each particle. Particles are attracted to the regions of higher field intensity, while Brownian motion counteracts the particle tendency to accumulate at the high field regions. Brownian motion provides statistical motion that allows the particles to sample all portions of the fluid volume and remain uniformly dispersed. The magnetic energy term $\mu_0 MHV$ represents the reversible work required to remove a magnetised particle from a region within the fluid where the magnetic field strength is H to a location in the fluid that is outside the influence of the field:

$$W = -\int_H^0 \left(\mu_0 M \frac{dH}{ds} V\right) ds \approx \mu_0 MHV \qquad (25)$$

If some part of the fluid volume is located in a field – free region, then stability of the particles in the fluid is favoured as opposed to particle segregation in the fluid due to a high ratio of the thermal energy to the magnetic energy:

$$\frac{thermal\ energy}{magnetic\ energy} = \frac{kT}{\mu_0 MHV} \geq 1 \qquad (26)$$

To consider the volume of a sphere in the above equation gives an expression for the maximum particle size:

$$d \leq (6kT/\pi\mu_0 MH)^{1/3} \qquad (27)$$

3.1.4. Dipole – dipole energy and gravitational field effects

Magnetic particles dispersed in a carrier fluid are also subject to aggregation and settling under a gravitational field similar to a magnetic force, as described above. Gravity constantly pulls an individual particle downward in a vessel, while Brownian motion tends to constantly keep the particles homogenously dispersed throughout the volume of the carrier fluid. The relative influence of gravity to magnetism is described by the ratio:

$$\frac{gravitational\ energy}{magnetic\ energy} = \frac{\Delta\rho g L}{\mu_0 MH} \qquad (28)$$

Collisions between particles in a magnetic fluid are frequent and if the particles adhere together, agglomeration will be rapid. The maximum energy needed to separate a pair of aligned particles with permanent magnetisation and diameter *d* is given by the dipole – dipole pair energy, E_{dd}:

$$E_{dd} = \frac{\pi}{9}\frac{\mu_0 M^2 d^3}{(l+2)^3} \qquad (29)$$

Where $l = 2s/d$, with s being the surface – to – surface separation distance. Thus, when particles are in contact, the above equation reduces to the following form, giving the dipole – dipole contact energy:

$$E_{dd} = \frac{1}{2}\mu_0 M^2 V \qquad (30)$$

The effectiveness of Brownian motion disrupting the agglomeration of particles in dispersion can be governed by the ratio:

$$\frac{thermal\ energy}{dipole-dipole\ contact\ energy} = \frac{12kT}{\mu_0 M^2 V} \qquad (31)$$

In order for particles to avoid agglomeration, this ratio must be greater than unity, so the particle size is given by:

$$d \leq (72kT/\pi\mu_0 M^2)^{1/3} \qquad (32)$$

For magnetite particles dispersed in a carrier liquid, the above equation requires $d \leq 7.8$ nm. This estimate indicates that a typical magnetic fluid with a particle diameter in the range up to 10 nm lie very close to the agglomeration threshold but manage to stay sufficiently stabilised[96].

3.2. DLVO theory

The DLVO (Derjaguin-Landau-Verwey-Overbeek) theory describes the stability of any suspension that composes particles with a tendency to aggregate over time.

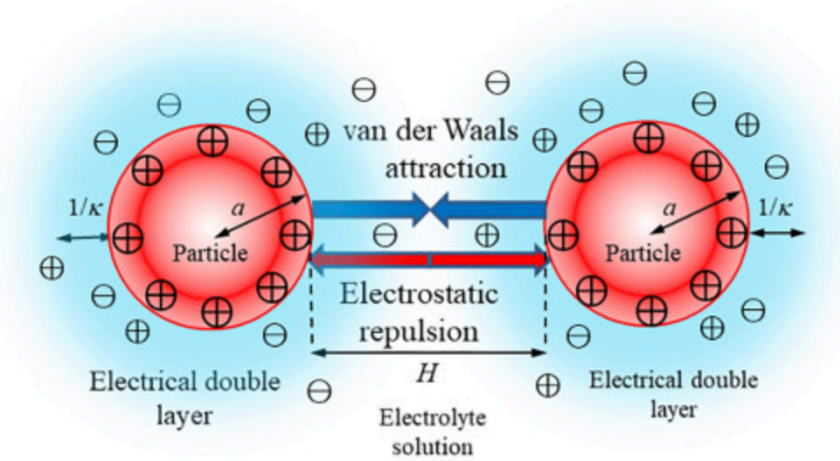

Figure 16: Electrostatic repulsion and van der Waals interaction forces acting between two approaching charged colloidal particles of radius a separated by a distance H[98].

The DLVO theory considers two fundamental interactions between approaching particles, these are electrostatic Coulomb and van der Waals interactions (**Figure 16**). The electrostatic repulsive force arise from like – charged particle surfaces or stabilising ionic layers on the particles, producing a long – range repulsion governed by Coulomb's law. In contrast, the van der Waals attractive force arise between neutral particles because of the fluctuating electric dipole – dipole forces that are always present. Van der Waals are generally short – ranged and independent of particle surface charge[96]. It is also important to consider the effect of the surrounding solvent or carrier fluid on the interactions between two surfaces or particles approaching closer than a few nanometres. The DLVO theory does not take into account the interactions between two solid surfaces in a liquid medium, these are generically called non – DLVO forces. When two particle surfaces approach each other, one layer of liquid molecules after another is squeezed out of the closing gap. The geometric constraining effect of the approaching particle wall on these molecules as well as the attractive interactions between the surface and liquid molecules cause the solvation forces between the two particle surfaces. When the solvent is water, this is referred to as hydration forces.

Hydration force is a strong, short – ranged force that decays exponentially with the distance between particles, D:

$$F_{SOL}(D) = Ke^{-D/l} \quad (33)$$

Where $K > 0$ relates to the hydrophilic repulsion forces and $K < 0$ relates to the hydrophobic attraction forces. l is the correlation length of the orientational ordering of water molecules[99,100].

The stability of a suspension is evaluated by the rate of particle aggregation. If the repulsive interactions between the particles are larger than the attractive interactions, the rate of aggregation will be slower and hence stability of the suspension is improved. It is important to note that the DLVO theory does not describe stable states in terms of thermodynamic stability but rather in the sense of aggregation rate being practically zero[98].

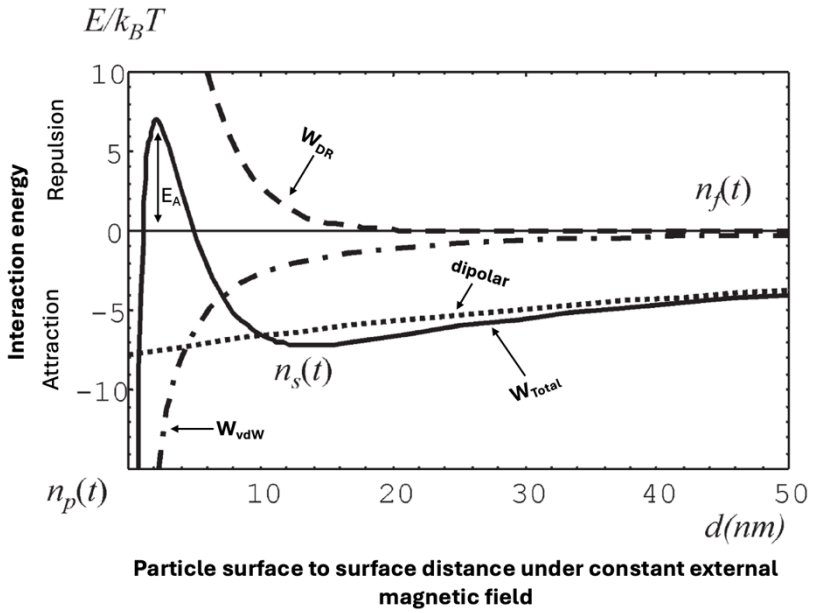

Figure 17: schematic representation of interaction energy between approaching magnetic particles under the influence of a constant external magnetic field. The curve is plotted as a function of the surface to surface distance, d[101].

The stability of a colloidal suspension is strongly dependent on the total potential energy, W_{Total}. The total interaction energy potential for two approaching magnetic particles in a suspension consist of a shallow secondary and a deep primary energy minimum that are separated by an energy barrier E_a of certain height. **Figure 17** shows a schematic plot of the

interaction energies between magnetic particles against particle surface to surface distance (nm). Magnetic particles can possess three different states when a magnetic field is applied: (i) aggregated in the primary minimum (close contact), (ii) aggregated in the secondary minimum (short distance), and (iii) unlinked (large distance). $n_p(t)$, $n_s(t)$, and $n_f(t)$ in **Figure 17** denote the number of primary, secondary, and open bonds (i.e. unestablished bonds).

W_{DR} represents the electrostatic interaction, while W_{vdW} represents van der Waals interaction between particles. The total potential energy, W_{Total} can be described as follows:

$$W_{DLVO} = W_{DR} + W_{vdW} \qquad (34)$$

$$W_{Total} = W_{DLVO} + dipolar \quad (35)$$

Particle aggregation can occur in the primary minimum, where the distance between particles is very small, or in the secondary minimum, where the neighboring particles within an aggregate are a short distance apart from each other. The height of the E_a is mainly determined by the electrostatic repulsion between the particles. In the case of a high E_a, particle aggregation is miniscule and the colloidal suspension remains stable. Whereas, a low E_a means that electrostatic repulsion between particles is weak which leads to destabilisation. Secondary minimum aggregation is reversible as the attractive magnetic interaction between the particles is reduced with elimination of the magnetic field. Hence, at large particle distances, the electrostatic repulsion seperates the particles giving rise to a breakdown of aggregates and improving stability. Aggregation in the primary energy minimum is typically irreversible, due to the close contact between particles allowing van der Waals interactions to maintain particle aggregation even when the external field is removed[101].

3.3. Colloidal stability in magnetic suspensions

In addition to the van der Waals attractive forces, magnetic nanoparticles can also be affected by magnetic dipole – dipole attractive interactions potentially leading to

aggregation and colloidal instability. Particles below a certain size (i.e. below 15 nm for iron oxide nanoparticles) can be considered superparamagnetic and do not display any remanent magnetisation. Hence there are no attractive magnetic interactions between the superparamagnetic nanoparticles in the absence of an external field and magnetic aggregation does not take place[102]. In contrast, colloidal stability in larger particles displaying permanent magnetic moments is very challenging. This is due to the dipole – dipole magnetic interactions between magnetic particles which significantly affect the colloidal stability of a ferrofluid by increasing particle aggregation. Dipole – dipole attractive forces are longer ranged (tens of nm) in comparison to other interparticle interactions such as van der Waal's which have a range of just a few nm[103,104]. The attractive interactions between two magnetic particles in a ferrofluid can additionally be affected by particle shape[105,106]. The centres of two adjacent plate – like particles are considerably closer than for two spherical or rod – like particles of the same volume, as a consequence the dipole- dipole magnetic interactions are stronger for a couple of plate – like particles[21].

The colloidal stability of a ferrofluid can be achieved by introducing sufficient repulsive interparticle interactions that counteract these attractive interactions. Electrostatic, steric or a combination of the two, i.e. electrosteric repulsion mechanisms can be applied to prevent aggregation of nanoparticles in the suspension[107]. To stabilise a ferrofluid via electrostatic repulsion mechanisms, the surface charge of the magnetic particles is typically altered. This can be done through the adsorption of ions from the isotropic carrier liquid such as OH^- from water, and/or by adsorption of specific charged species from the carrier liquid onto the particle surfaces. The electrostatic interaction energy depends on the particle surface potential (Ψ) the dielectric constant of the isotropic liquid, the presence of counter ions as well as ionic strength and pH. These factors will affect the Debye – Huckel parameter, which represents the distance to where the electrostatic interaction is significant between the particles[108,109]. Colloidal stability in ferrofluids can also be attained through steric repulsion through the adsorption of macromolecule stabilising agents onto the magnetic particle surface. Steric repulsion is only affective at a short distance and is short – ranged compared to electrostatic and dipole – dipole magnetic interactions. To provide colloidal stability in a ferrofluid through a combination of steric and electrostatic repulsive mechanisms, macromolecule stabilising agents carrying a charge can be adsorbed onto the magnetic

particle surface. A combination of repulsive mechanisms may be required for larger particles due to the electrostatic repulsion being insufficient as the particles get closer. The particle shape can also affect the electrostatic and steric repulsive forces which are much stronger in anisotropic, plate – like particles which have a much larger interaction surface than two spherical particles of the same volume. Therefore, to successfully stabilise a ferrofluid, the magnetic particle surface must be tuned according to particle size, shape, and carrier fluid.

3.4. Electrosteric stabilisation of BHF nanoparticles using dextran biopolymer

Barium hexaferrite (BHF) nanoparticles are a typical representation of anisotropic permanent magnetic nanoparticles in ferrofluids. Colloidal stabilisation of BHF nanoparticles is essential in ferrofluids due to their particle size, plate – like shape and permanent magnetic properties. As discussed above, colloidal stabilisation can be achieved through the modification of particle surface and introducing repulsive interaction mechanisms. The surface of particles can be modified using different methods to achieve colloidal stabilisation in ferrofluids. One such way is to functionalise a magnetic particle's surface with macromolecule stabilising agents such as charged surfactants, ligands or polymer brushes (such as cetyl trimethylammonium bromide (CTAB), stearic acid, linoleic acid, citric acid and dextran.)[110,111,112]. If these macromolecule stabilising agents are not irreversibly (covalently) bound to the nanoparticle surface, they can easily detach via adsorption/desorption mechanisms which can lead to particle aggregation and colloidal instability. However, an irreversible covalent attachment of the stabilising macromolecule to the nanoparticle surface ensures long - term colloidal stability as the covalent bond between the macromolecule stabilising agent and the particle surface is strong and not sensitive to changes in the environment (e.g. pH, ionic strength, temperature)[113].

In a previous study, hydrothermally synthesised BHF permanent magnetic nanoparticles were coated with a dextran polymer to produce a stable colloidal dispersion in complex biological media through electrostatic and steric repulsive mechanisms[104]. Dextran is one of the most widely used biopolymer for the coating of magnetic nanoparticles[114] due to its biocompatibility and low cytotoxicity[115]. Generally, a dextran coating on magnetic nanoparticles is achieved in – situ during the synthesis of the nanoparticles or through a

coating process post – synthesis which involves adsorption via the formation of hydrogen bonds between the dextran – OH groups and the Fe – OH on the nanoparticle surface. However, in – situ coating of dextran is not attainable with BHF nanoparticles as they are hydrothermally synthesised and preliminary tests of post – synthesis dextran coating onto BHF nanoparticle surface also did not prevent aggregation[104]. A stable aqueous suspension of the BHF nanoparticles was initially prepared by adsorbing citric acid onto the particle surface, followed by coating the nanoparticles with a thin layer of silica to improve the chemical reactivity of the BHF nanoparticles. The Si – OH bonds from the silica molecules form stable Fe – O – Si covalent bonds with Fe^{3+} ions on the BHF nanoparticle surface[113]. A separate mixture of dextran and a coupling agent/linker called Glycidoxypropyltrimethoxysilane (GLYMO) is first prepared to allow the epoxide rings of the GLYMO molecules to react with the OH groups of the dextran polymer. The product of this mixture is then grafted onto the silica – coated BHF nanoparticles. The purpose of the GLYMO linker is hence to ensure a covalent bond is formed between dextran and the BHF nanoparticle surface.

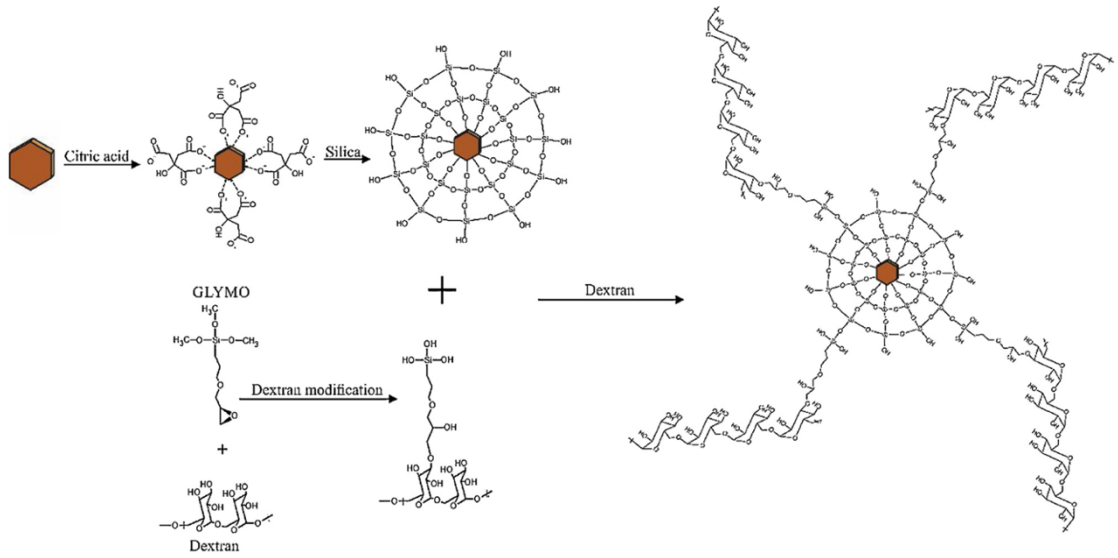

Figure 18: Schematic presentation of the barium-hexaferrite nanoplatelets functionalisation strategy with dextran[104].

The functionalisation of dextran onto BHF nanoparticles is illustrated in **Figure 18**. The dextran coated BHF nanoparticles were characterised using chemical, thermal and magnetic analytical techniques. The size and size distribution of the dextran coated BHF nanoparticles was compared with as – synthesised BHF nanoparticles and showed a general narrowing of

particle size distribution where the majority of as – synthesised BHF nanoparticles were on average 40 ± 18 nm wide, and the dextran coated BHF nanoparticles were on average 52 ± 12 nm wide. The size selection can be a consequence of processing the nanoparticle suspensions. Generally, a narrow size distribution produces an easier dispersion of magnetic nanoparticles in a liquid medium, however, the average size of both the as – synthesised and dextran coated BHF nanoparticles synthesised in this study can be considered small. The dextran coated BHF nanoparticles were dispersed in different physiological buffers and complex biological media containing all the substances that ensure a physiological balance (plasma protein, polypeptide, fat, carbohydrate, growth factor, hormones, and inorganic mineral). The chosen coating materials, silica and dextran, are biocompatible and FDA approved. 10 wt% of the dextran adsorbed onto the BHF nanoparticle surface was replaced with a modified version of dextran called DEAE – dextran which possess a ternary amine. The ternary amine provides a positive charge to the BHF nanoparticle surface aiding in electrostatic and steric repulsion for colloidal stability in biological media. The colloidal stability of the dextran coated BHF nanoparticles was measured using zeta potential. Dextran coated BHF nanoparticles produced a zeta value of -10 mV while the BHF nanoparticles grafted with the modified DEAE – dextran produced a value of +10 mV at neutral pH. The low zeta potential values suggest that the colloidal stability is ensured by steric repulsion as opposed to electrostatic repulsive mechanisms. However, this study provides a unique and versatile functionalisation strategy as it demonstrates that the surface charge of the BHF nanoparticle surface can be modified according to the demands of specific applications by adsorbing different forms of the dextran polymer. The colloidal stability of the BHF nanoparticles in biological media was also evaluated by visual assessment as well as Dynamic Light Scattering (DLS). However, visual assessment is not an objective measurement and DLS analysis does not give an accurate result for non – spherical particles. The colloidal stability of the as – synthesised and dextran coated BHF nanoparticles was evaluated at a low concentration of 0.1 mg/ml and does not report how stability of the particles in the liquid media is affected at higher concentrations. Nevertheless, this study presented substantial advancement in the colloidal stabilisation of permanent magnetic BHF nanoparticles as opposed to traditionally considered superparamagnetic nanoparticles and paves the way towards some biomedical applications and treatments[104].

3.5. Colloidal stabilisation of BHF magnetic nanoparticles in ferrofluids using DBSA surfactant

For the stability of any ferrofluid, it is crucial to tune the size, size distribution, and surface properties of the particles. Other than long chain polymers like dextran, surfactants are another type of macromolecules that can be used for colloidal stabilisation. Long – chain surfactants which provide for steric stabilisation of the suspension, can be used when the particle size and hence, the magnetic moments of the particles are relatively small. In the case of suspensions composing small particles, the average magnetic interaction between the particles at contact is weaker than the thermal energy in the absence of an applied magnetic field. However, under an applied magnetic field the magnetic interaction between particles becomes stronger than the thermal energy resulting in chain – like structures which causes an increased viscosity of the suspension[116,117,118]. Conversely, in the case of suspensions composing larger particles with larger magnetic moments, average contact magnetic interaction between the particles exceeds thermal energy significantly. This results in long chain – like aggregates forming already in the absence of an applied magnetic field and electrostatic in combination with steric stabilisation becomes necessary for colloidal stabilisation. Surfactants carrying a positive or negative ionic charge can be functionalised onto the surface of magnetic particles to provide for electrosteric repulsion.

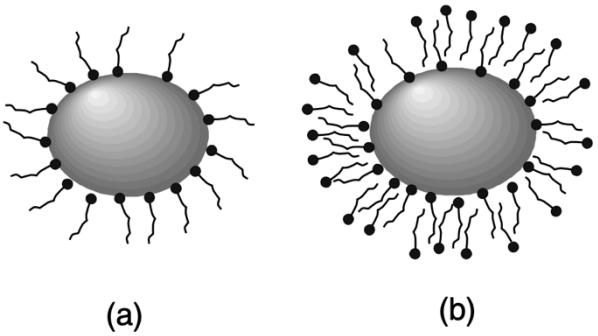

Figure 19: shows illustration of surfactant – functionalised particles with a single layer of surfactants (a) and a double – layer of surfactants (b)[119].

Figure 19 shows how surfactants arrange themselves in polar and non – polar solvents. If the nanoparticles are dispersed in a non - polar carrier liquid, the surfactant forms an external

hydrophobic layer around the nanoparticle surface. The polar head of the surfactant point towards the surface of the magnetic nanoparticles, while the alkyl chains align towards the non – polar solvent. Conversely, If the particles are dispersed in a polar solvent, such as water, a double layer of surfactant is necessary to create an external hydrophilic layer. For polar colloidal dispersions, including aqueous magnetic liquids, it is assumed that an excess of surfactant molecules is needed to form the second layer of surfactant molecules on the magnetic nanoparticle surface. The first (hydrophobic) layer is chemically adsorbed at the surface of the magnetic nanoparticles and the second (hydrophilic) layer, is physically adsorbed at the first surfactant layer. Due to the low bonding energy of the physically adsorbed second layer, free surfactant molecules remain dissolved in some excess in the polar carrier liquid[120,121]. Also, the balance between the adsorbed and free excess surfactant molecules within the double layer is constantly changing, hence, the colloidal stability of polar – based ferrofluids changes drastically upon dilution[122]. Additionally, the particles can aggregate if a surfactant with the opposite charge to the surface charge of the particles in the aqueous solvent is used. For the adsorption of oppositely charged surfactants onto the particle surfaces, the electrostatic and hydrophobic interactions between the surfactant molecules must be considered[123]. If the surfactant concentration is low, the particles will aggregate due to a strong hydrophobic force[124], leading to colloidal instability. This can be avoided by increasing the surfactant concentration as the particles become hydrophilic again once a bilayer surfactant coating is formed as shown in **Figure 19**. With a bilayer formation of the surfactants, the stability of the suspension improves due to electrostatic and steric repulsions[125].

In the case of BHF magnetic nanoparticles, the aggregates formed due to attractive van der Waals and magnetic dipolar interactions are usually columnar due to the magnetic easy axis being oriented perpendicular to the ab plane. Therefore, for the colloidal stability of BHF nanoparticles in a liquid carrier, it is essential to induce repulsive interactions between the nanoparticles. Long – chain surfactants with dielectric properties corresponding to the surrounding solvent can provide for electrosteric stabilisation[126,109]. A recent study has shown that surface modification of BHF nanoparticles with a double layer of dodecylbenzenesulfonic acid (DBSA) surfactant allows for the formation of stable colloidal suspensions in alcohols[126]. Initially, the first prepared suspensions of DBSA – modified BHF

nanoparticles in alcohol had short – term stability despite electrosteric repulsion provided by the DBSA. This was due to the diameter of the BHF nanoparticles being a few hundred nanometres in size, leading to aggregation and eventually sedimentation of particles. However, after narrowing the particle diameter distributions and eliminating large BHF nanoparticles by partial substitution of Fe^{3+} with Sc^{3+}, the DBSA surfactant provided for sufficient electrosteric stabilisation in different alcohols[41]. The parameters that affect the electrostatic interaction between the BHF nanoparticles in different alcohols including tert – butanol, 1 – hexanol, 1 – butanol, and 2 – propanol were studied[109].

Experimental findings showed that the first layer of the DBSA is adsorbed onto the positively charged BHF nanoparticle's surface[109]. The positive charge on the BHF nanoparticle surface comes from the protonated DBSA sulfonic groups which are formed by a proton exchange between the BHF nanoparticle surface and the DBSA molecule. Once the DBSA – coated BHF nanoparticles are hydrothermally synthesised, they start to show hydrophobic behaviour and aggregate in a strongly polar medium like water. The exchange of the water with alcohol causes partial desorption of the DBSA molecules from the surface of the BHF nanoparticles and a double – layer of DBSA surfactant forms. There is a dynamic equilibrium between the DBSA molecules in the double layer and the system, such that part of the desorbed DBSA molecules form the double layer, while another part is dissolved and partially dissociated in the alcohol suspension. This dynamic equilibrium is affected by the total fraction of the surfactant, the concentration of the nanoparticles, and the properties of the alcohol. It was found that the amount of dissolved DBSA surfactant is lower in more polar alcohols like 2 – propanol and 1 – butanol suspensions compared to less polar alcohols such as 1 – hexanol and tert – butanol suspensions. A decrease in the suspension concentration caused additional DBSA molecules to desorb from the BHF nanoparticle surface and dissolve in the alcohol suspension. Conductivity measurements showed that the dissociation of the DBSA surfactant molecules is higher in more polar solvents like 1 – butanol and 2 – propanol. The dissociated DBSA molecules weakly shield the BHF nanoparticle's charge resulting in stronger electrostatic repulsive forces and improved colloidal stability. Additionally, less polar solvents dissociate lower concentration of DBSA surfactant which makes the ionic strength of the suspension lower. Hence, more polar solvents may disperse DBSA – coated BHF nanoparticles better than less polar solvents producing a stable ferrofluid.

Key findings from the experiments conducted on DBSA – coated BHF nanoparticles have highlighted the importance of the total fraction of DBSA surfactant in stabilising the suspension. This is due to the dynamic equilibrium between the dissolved and adsorbed DBSA molecules. If the concentration of dissolved DBSA molecules is too high, this causes the nanoparticles to aggregate due to a high screening of the charge and the suspensions destabilises. The concentration of dissolved DBSA molecules affects the concentration of adsorbed DBSA to the BHF surface. If the latter is too low, the system cannot ensure efficient surface coverage of the BHF nanoparticles, leading to aggregation and colloidal destabilisation. DBSA has proven to be an extremely successful surfactant at stabilising BHF nanoparticles with the highest colloidal stability found in 1 – butanol due to a combination of high enough surface charge and low enough dielectric constant. DBSA also allowed a higher concentration of BHF nanoparticles to be dispersed in the alcohols including 1-butanol compared to previous studies exploring dextran as a stabilising agent for BHF nanoparticles in suspension.

Chapter 4: Experimental methods: Barium hexaferrite particle growth in response to temperature.

Understanding the growth mechanism of barium hexaferrite nanoparticles via hydrothermal synthesis is of great interest to optimise the structural and magnetic properties which impacts particle dispersion. A previously reported hydrothermal synthesis method for BHF nanoparticles was reproduced at varying temperatures following by a detailed analysis of particle size and morphology using Scanning Electron Microscopy (SEM) and Vibrating Sample Magnetometer (VSM). The purpose of this study was to identify an optimal hydrothermal synthesis temperature at a constant heating rate which yields BHF with platelet morphology, narrow size distribution, and applicable magnetic properties.

4.1. Introduction

Barium hexaferrite (BHF) nanoparticles are traditionally prepared using a solid – state synthesis method including a high – temperature treatment of precursors usually Fe_2O_3 and $BaCO_3$ at around 900 °C followed by milling[127]. Many different methods can be used for the precursor preparation, including chemical precipitation in aqueous media[128,129] reverse – micelle – based methods[130] and low – temperature combustion synthesis[127]. To decrease the formation temperature, the precursors containing a homogenous mixture of constituting ions are calcined to synthesise smaller crystallites. However, the calcination of the precursors prepared by most synthesis methods yield a broad particle size distribution even when the formation temperature is reduced to 500 °C[130]. Other methods such as glass crystallisation have been reported to produce BHF in the superparamagnetic size range using high temperatures[131,132], but these can be relatively complex, unsuitable for large – scale production and very expensive. Alternatively, BHF nanoparticles can be obtained at low – temperatures using an in – situ hydrothermal synthesis[133,134] at a much lower cost than the above-mentioned methods. The low temperature is facilitated by strongly increasing the concentration of hydroxyl (OH^-) ions relative to the metal ion precursors (Ba^{2+} and Fe^{3+}). The iron hydroxide ($Fe(OH)_3$ is amphoteric and forms tetrahydroxoferrates (III) $[Fe(OH)_4]^-$, in an alkaline medium. The high concentration of hydroxyl ions favours the association of $[Fe(OH)_4]^-$ ions into iron – rich aggregates of $[Fe(OH)_4{}_n^{n-}]$ [135]. This aids in the formation of the hexaferrite as $[Fe(OH)_4{}_n^{n-}]$ complexes easily combine with one Ba ion to form $BaFe_{12}O_{19}$ (i.e. barium hexaferrite) compared to 12 individual $[Fe(OH)_4]^-$ ions. Hence, the supersaturation and consequently, the nucleation of hexaferrite is allowed at lower temperatures.

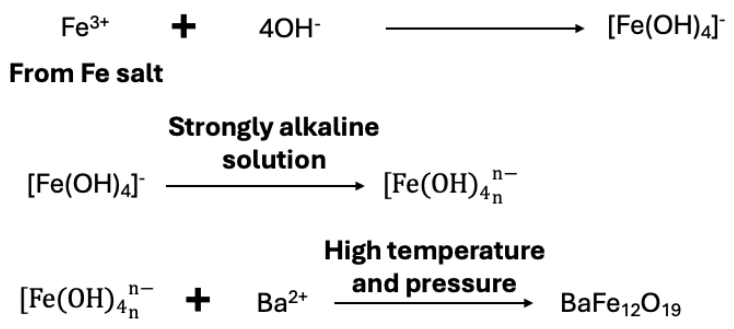

Figure 20: chemical reactions between Fe^{3+} and Ba^{2+} precursors to form $BaFe_{12}O_{19}$ using low temperature hydrothermal synthesis facilitated by an exceess of OH^-.

Figure 20 shows the chemical reactions involved between Fe^{3+} and Ba^{2+} precursors in the hydrothermal synthesis of $BaFe_{12}O_{19}$. In this chapter, experimental findings are presented on particle size and magnetic properties of Sc – substituted BHF nanoparticles coated with DBSA surfactant which were hydrothermally synthesised at varying temperatures in an excess of hydroxyl (OH^-) ions relative to metal ions.

4.2. Experimental

4.2.1. Materials

Barium nitrate (99%) and nitric acid (70%) were obtained from Thermo-Fisher scientific. 1-butanol (99%), scandium (III) nitrate hydrate (99%) and iron (III) nitrate nonhydrate (98%) were obtained from Alfa-Aesar. Sodium hydroxide (98%) and DBSA (95%) were obtained from Sigma-Aldrich.

4.2.2. Synthesis of the nanoparticles:

Sc-substituted BHF nanoparticles were hydrothermally synthesised at varying temperatures following a previously reported "state of the art" procedure[41,109]. The previously reported hydrothermal synthesis produces Sc – substituted BHF nanoparticles with hard magnetic properties at a temperature of 240 °C with DBSA surfactant adsorbed onto the BHF particle surface. To assess how the size and shape of these Sc – substituted BHF particles changes with temperature, the previously reported hydrothermal synthesis process was repeated at varying temperatures of 120 °C – 270 °C.

For the preparation of BHF nanoparticles, the barium (0.62 g), iron (III) (4.36 g) and scandium (III) (0.35 g) nitrates were dissolved in deionised water in a molar ratio of 1:4.5:0.5. An excess of sodium hydroxide (26.2 g) was gradually added after which precipitation occurs and the solution was allowed to cool to room temperature. A solution of DBSA (1.80 g) is then dissolved in 25 ml of acetone and gradually added to the reaction mixture over a

period of 30 minutes, the mixture was subsequently allowed to stir for 30 min. The suspension of precipitated precursors was sealed in an autoclave vessel and heated with a heating rate of 3 °C /min to various synthesis temperatures including 120 °C (BHF-120°C), 160 °C (BHF-160°C), 170 °C (BHF-170°C), 190 °C (BHF-190°C), 220 °C (BHF-220°C), 240 °C (BHF-240°C), 270 °C (BHF-270°C). After reaching the desired synthesis temperature, the autoclave is immediately allowed to cool to 20 °C at 3 °C/min. The resultant nanoparticles were centrifuged at 201 rcf for 5 min and washed with water. The nanoparticles were dispersed in 60 ml of water and the pH was adjusted to 1.5 using nitric acid. The mixture was then heated to 100 °C for 2 h on stirring. The nanoparticles were centrifuged and washed with water and acetone to remove excess surfactant and dried at 60 °C. The dry nanoparticles were then dispersed in 1-butanol to create a ferrofluid at a concentration of 100 mg/ml using ultrasonication (Fisherbrand) at 35 W for 2 h.

4.2.3. Characterisation of materials:

The magnetic properties of dry DBSA – coated BHF nanoparticles were measured using Vibrating-Sample Magnetometer – VSM (LakeShore 7400). VSM samples were prepped by measuring a few milligrams of BHF dry powder into a non – magnetic plastic capsule. The powder is gently compacted into the capsule to avoid movement during measurement. It is important to ensure that the powder completely fills the sample holder to remove any air gaps.

The structural properties of the BHF nanoparticles were studied using Scanning Electron Microscopy – SEM (Carl Zeiss Gemini). SEM samples were prepared by drop – depositing a 1mg/ml ferrofluid onto a Cu – grid support, the carrier solvent was allowed to evaporate at 200 °C on a magnetic plate for 24 h. The size of the BHF nanoparticles were microscopically analysed for each hydrothermal synthesis temperature.

4.3. Results and discussion

Sc – substituted BHF nanoparticles coated with DBSA surfactant were hydrothermally synthesised at temperatures between 120 – 270 °C. The hydrothermal synthesis process starts with coprecipitation of the dissolved cations i.e., Ba^{2+}, Fe^{3+} and Sc^{3+} at room temperature prior to the barium hexaferrite formation. Barium hexaferrite precursors are amorphous coprecipitates of the cations and can precipitate as homogenous mixtures of hydroxides or form an intermediate phase. The precipitation temperature is too low for the BHF nanoparticles to form, and elevated synthesis temperatures are required for the BHF nanoparticles to grow[48,136]. Many synthesis parameters can be adjusted to optimise BHF particle size and size distribution, such as, synthesis temperature, synthesis time, precursor concentration and hydroxyl ion to metal precursor ion concentration ratio which will ultimately determine the long – term stability of the particles in dispersion. Synthesis time is not treated as a variable in the hydrothermal synthesis process, as the reaction is cooled to room temperature immediately upon reaching the target peak temperature. Synthesis temperature is an extremely important factor for BHF particle growth and dispersion as it directly affects Particle Size Distribution (PSD) and enables secondary recrystallisation for larger particles to grow. Hence, it is important to identify the optimal synthesis temperature for Sc - substituted BHF particles coated with DBSA surfactant.

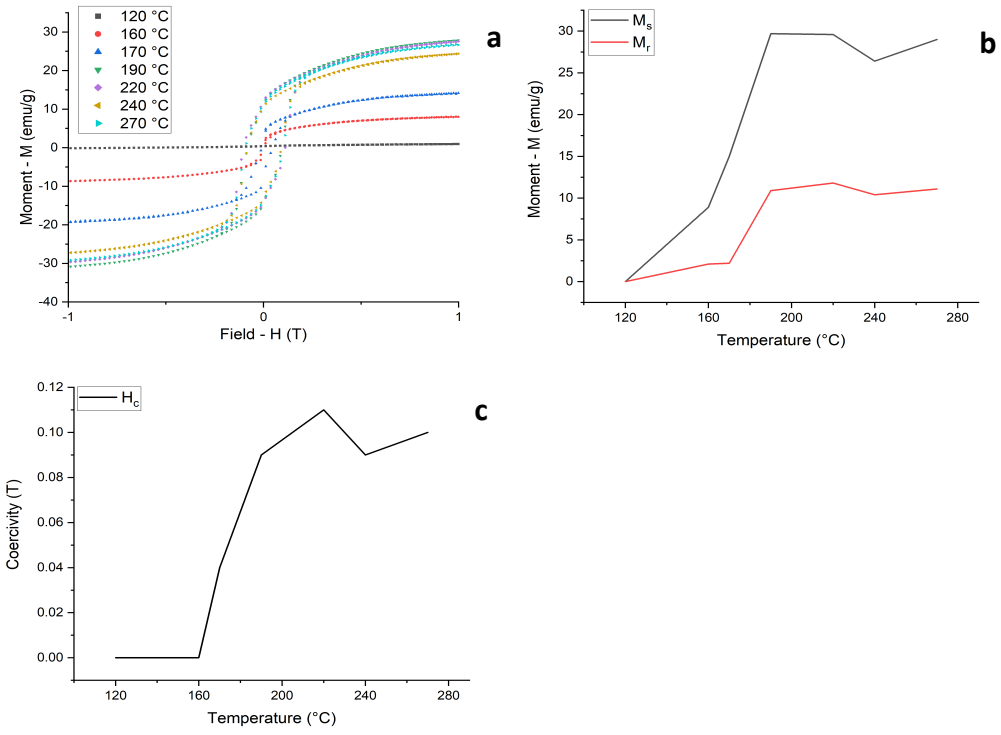

Figure 21: a) the applied Field – H against Moment – M of barium hexaferrite nanoparticles synthesised between 120 – 270 ℃, b) the magnetic saturation and remanence for 120 – 270 ℃, c) coercivity for 120 – 270 ℃.

Figure 21 shows the magnetic properties of Sc – substituted BHF particles coated with DBSA surfactant hydrothermally synthesised at temperatures between 120 – 270 °C. BHF particles synthesised at 120 °C i.e. BHF-120 °C, showed a negligible magnetic response below 20 emu/g measured at 2 T (**Figure 21a**). Ultrafine hexaferrite nanoparticles form at temperatures below 100 °C and are around 10 nm wide and approximately 3 nm thick with a discoid shape[137,127]. When dispersed in a polar solvent like 1 – butanol, BHF-120 °C were stable for many months but a visual response to an external magnet was not observed due to the small particle size. The long – term stability of the particles can be explained due to insignificant magnetic dipole – dipole interactions between the particles. This is consistent with previous studies[137] which state that BHF particles do not grow significantly with increased temperature until hydrothermally treated at temperatures above approximately 150 °C. After nucleation, the hexaferrite nanoparticles experience limited growth due to the precursors being consumed by the hexaferrite formation reactions, in which case, elevated temperatures are needed for further particle growth[138]. At synthesis temperatures above 150 °C, the BHF start to grow exaggeratedly through a mechanism of secondary recrystallisation called Ostwald ripening[139,140]. Ostwald ripening is the process by which larger particles grow at the expense of smaller ones, i.e., smaller particles redissolve in solution while the larger particles keep growing.

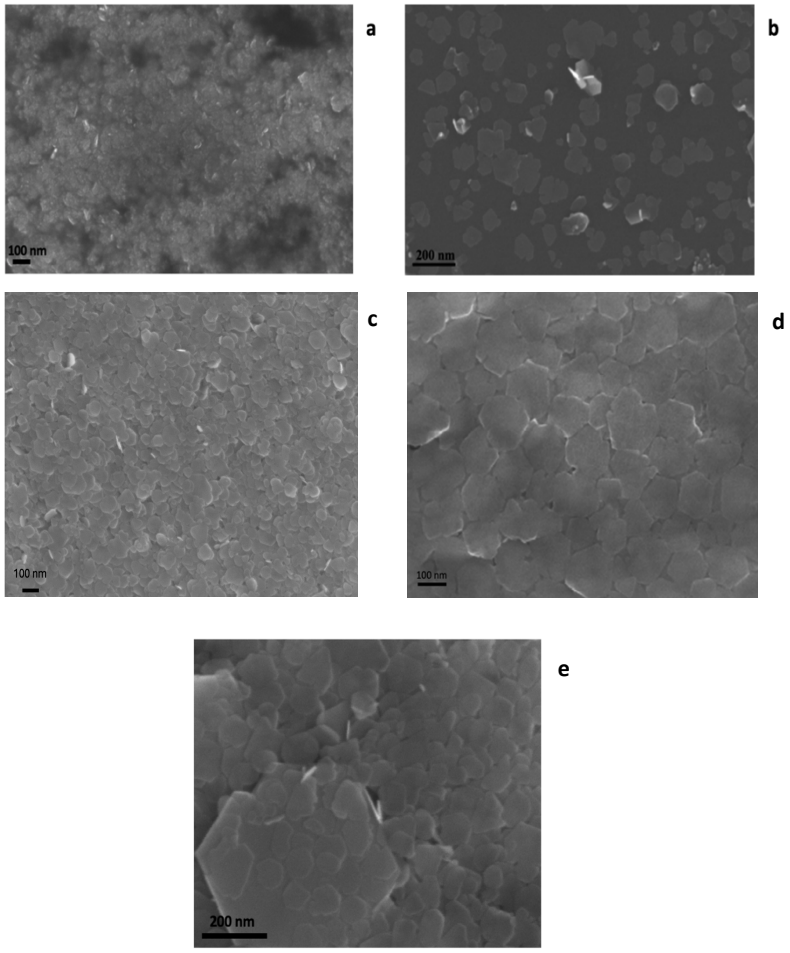

Figure 22: SEM images of BHF synthesised at 170 ℃ (a), 190 ℃ (b), 220 ℃ (c), 240 ℃ (d), and 270 ℃ (e).

BHF-160 °C and BHF-170 °C display a higher magnetic saturation compared to BHF particles synthesised at 120 °C (**Figure 21b**). Both BHF-160 °C and BHF-170 °C display hysteresis loops reminiscent of a soft magnetic material which uncharacteristic of BHF nanoparticles. A significant difference between synthesis temperatures 160 °C and 170 °C was observed, whereby the remanence magnetisation remains almost constant, but both magnetic saturation and coercivity are much higher for 170 °C than 160 °C despite only a 10 °C increase in temperature. This difference is not observed at higher temperatures (190 – 270 °C). **Figure 22** shows SEM images of BHF-170°C, BHF-190°C, BHF-220°C, BHF-240°C, BHF-270°C. The SEM images of BHF-170 °C shows BHF nanoparticles with an irregular, discoid shape which means that a much higher synthesis temperature is needed to produce homogenous hexagonal BHF nanoparticles. The particle size of BHF-160 °C and BHF-170 °C was not measured using the SEM images obtained for both synthesis temperatures due to an overpopulation of small discoid shaped particles. However, previous studies using

advanced imaging techniques like HAADF STEM have suggested the presence of a two – size population of BHF nanoparticles hydrothermally synthesised at 160 °C containing small, discoid primary nanoparticles and larger, exaggerated grown (secondary) nanoparticles[137] which coincides with the relatively low saturation magnetisation obtained for both 160 °C and 170 °C (**Figure 21b**). Low dipole – dipole magnetic interactions between the BHF particles synthesised at 160 °C and 170 °C allowed easy dispersion of these particles in 1 – butanol with long – term stability. When the temperature of the hydrothermal treatment is increased from 170 °C, the size of the exaggeratedly growing particles rapidly increased and the content of the small, primary discoid nanoparticles decreased. This can be clearly observed in the SEM images of BHF-190 °C (**Figure 22b**) showing a majority of large particles compared to BHF-170 °C (**Figure 22a**). The hysteresis loop of BHF-190 °C, BHF-220 °C, and BHF-240 °C, represent a hard magnetic material which is typical of BHF particles, signifying much larger particles produced at 190 – 240 °C compared to 170 °C. As the hydrothermal synthesis temperature is increased above 170 °C, secondary growth via the Ostwald ripening effect is much more likely to occur. Temperatures studied above 170 °C i.e., 190 – 270 °C, produced a much higher magnetic moment in response to an external magnetic field with BHF nanoparticles synthesised at 240 °C showing an unexpected drop in magnetic moment and coercivity.

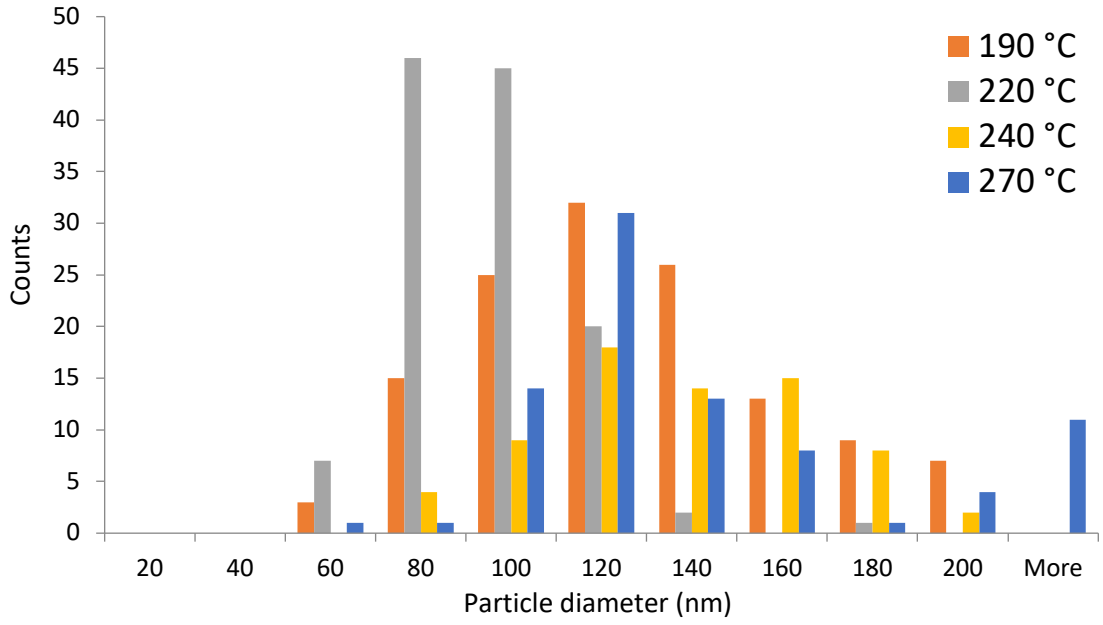

Figure 23: Particle size distribution for BHF-190 ℃ (orange), for BHF-220 ℃ (grey), for BHF-240 ℃ (yellow), and for BHF-270 ℃ (blue).

The particle diameters of BHF particles synthesised at 190 – 270 °C was manually measured using SEM images of approximately 200 – 300 particles and the particle size distribution at these temperatures is displayed in **Figure 23**. BHF-190 °C showed an average particle diameter of 116 nm while the average particle diameter for BHF-220 °C was 84 nm which is surprisingly smaller than BHF-190 °C. Similar to BHF-190 °C, BHF-240 °C produced an average particle diameter of 126 nm. When suspended in 1- butanol, BHF-190 °C, BHF-220 °C and BHF-240 °C particles were easy to disperse and showed long – term stability over several months undisturbed. Ferromagnetic behaviour of BHF-190 °C, BHF-220 °C and BHF-240 °C in 1-butanol can also be visually observed in the presence of an external magnet. In contrast, BHF-270 °C produced a much higher average particle diameter of 195 nm. The PSD of BHF-270 °C shown in **Figure 23** is much wider than the other experimented synthesis temperatures with a particle size range of 1139 nm. The range of particle size for BHF-270 °C is much larger than BHF-190 °C, BHF-220 °C and BHF-240 °C which all produced a range between 123 – 145 nm. The substitution of Sc^{3+} for F^{3+} has also been shown to narrow down the size distribution of BHF particles[41,43] by blocking Ostwald ripening. However, for hydrothermal synthesis temperatures as high as 270 °C, the Sc – substitution is ineffective at preventing secondary recrystallisation and temperature dominates as a factor for particle growth. **Figure 22(e)** shows BHF-270 °C particles as big as 1.1 µm with smaller nanoparticles deposited on top. The growth rate of these exaggerated particles is relatively fast which makes particle size harder to control. When dispersed in 1 – butanol, BHF-270 °C particles immediately aggregated when introduced into the solvent and showed no signs of visual colloidal stabilisation. From these results, an optimal synthesis temperature for BHF nanoparticles can be identified between 190 – 220 °C at a rate of 3 °C /min as similar structural and magnetic properties are produced with a narrow size distribution to aid dispersion. Although a hydrothermal synthesis of BHF nanoparticles at higher temperatures would be of interest, since at higher temperatures better structural order and consequently better magnetic properties can be expected. However, the mechanism of secondary re-crystallisation must be suppressed in order to maintain a narrow, mono – modal size distribution of the synthesised particles.

4.4. Conclusions

A study of the temperature dependent magnetic and structural properties of hydrothermally synthesised barium hexaferrite nanoparticles is reported. The synthesis of Sc – substituted BHF particles coated with dodecylbenzenesulfonic acid surfactant were synthesised at temperatures between 120 – 270 °C and characterised using Scanning Electron Microscopy and Vibrating-Sample Magnetometer techniques. The average size of the barium hexaferrite nanoparticles were found to increase with increased synthesis temperature with a wider particle size distribution at higher temperatures. Specially, optimal magnetic and structural properties were identified between 190 – 220 °C while 240 °C shows an unexpected drop in magnetic saturation and coercivity. Synthesis temperature 270 °C produced an extremely wide particle size distribution with particles as wide as 1.1 µm which largely compromises the dispersion of the barium hexaferrite nanoparticles in a liquid medium.

Chapter 5: Synthesis of barium hexaferrite nano-platelets for ethylene glycol ferrofluids

5.1. Introduction

This chapter describes a surfactant – assissted hydrothermal synthesis method of BHF nanoparticles. Surfactants hexadecyltrimethylammonium bromide (CTAB) and sodium dodecyl sulfate (SDS) were both studied and compared in stabilising BHF nanoparticles in varying non – magnetic solvents. The focus of this chapter is then shifted towards a CTAB – assissted hydrothermal manufacturing method and dispersion of BHF nanoparticles in ethylene glycol to produce a ferrofluid characterised using magnetic, microscopic, and electrostatic techniques. The proposed ethylene glycol based ferromagnetic-ferrofluid exhibits great stability and low volatility with excellent thermal properties, and therefore opens the way for commercial applications.

5.2. Sodium Dodecyl Sulfate (SDS) surfactant

For the stability of any ferrofluid, it is crucial to tune the size, size distribution, and surface properties of the BHF particles. In the case of particles with a relatively small magnetic moment, surfactants which provide for steric stabilisation of particles in suspension will suffice. However, particles in suspension with a larger magnetic moment for which average contact magnetic interaction between the particles exceeds thermal energy significantly, both electrostatic and steric repulsion is needed for colloidal stability. This is due to the long chain – like aggregates that form already in the absence of an external magnetic field. Long – chain ionic surfactants that exhibit a charge upon functional group dissociation can provide for both electrostatic and steric, i.e. electrosteric repulsion between particles. In addition, long – chain ionic surfactants with dielectric properties corresponding to the surrounding solvent can successfully counteract attractive forces between particles[109].

Different combinations of surfactants were trialled for the functionalisation and dispersion of BHF particles in a suitable solvent. The surfactants were trialled on the basis of chain – length, surfactant charge, and thermal stability, as these factors affect the efficiency of adsorption onto particle surface and hence, affect the long – term stability of the ferrofluid. The chemical and thermal properties of the carrier fluid were also considered, including boiling point, volatility, polarity, and dielectric constant. The potential functionalisation of BHF particle's surface with Sodium Dodecyl Sulfate (SDS) surfactant was investigated using a previously described hydrothermal synthesis method[109]. This was followed by testing the dispersion of the resulting particles in a range of solvents with differing polarities. SDS is a long – chain anionic surfactant with the formula $C_{12}H_{25}NaO_4S$.

*Table 4: shows the polarity and dielectric constant of solvents tested for homogenous dispersion of dry SDS treated BHF nanoparticles. *A poor dispersion of nanoparticles in a solvent can be deciphered by the an instant rejection of the nanoparticles once introduced into the solvent, this can be observed through a clear separation between nanoparticles and solvent which remains upon ultrasonication for ~2 hours. A moderate dispersion of nanoparticles in a solvent is usually observed as a separation between the nanoparticles and solvent after ultrasonication for ~2 hours. A successful dispersion can be observed as the nanoparticles easily disperse within the solvent without the need for extended ultrasonication and without separation of nanoaprticles and solvent, even in the presence of a magnetic field.*

Solvent	Polarity [-]	Dielectric constant [-]	Successful dispersion?*
Iso – hexane		1.89	Poor
Heptane		1.92	Poor
Decane		2.00	Poor
Cyclohexane		2.02	Poor
Benzene		2.27	Poor
Toluene		2.38	Poor
Diethyl ether		4.33	Poor
Butanol		17.8	Moderate
Propanol		20.1	Poor
Ethanol		24.5	Poor
Methanol		32.7	Poor
Ethylene glycol		37.0	Poor
Water		80.1	Poor

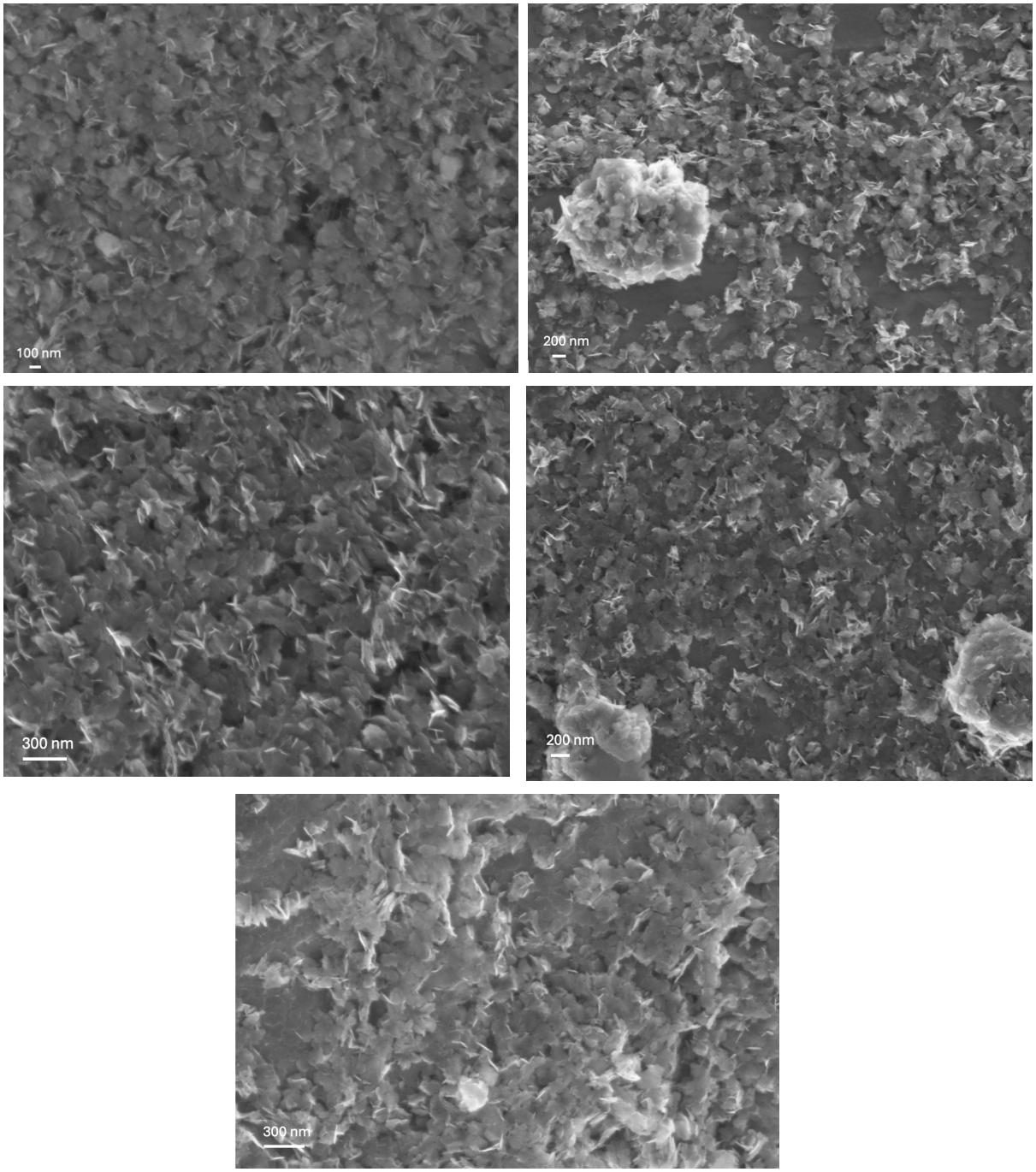

Figure 24: SEM of SDS – coated BHF nanoparticles in butanol (top left), propanol (top right), ethanol (middle left), methanol (middle right), and ethylene glycol (bottom).

Hydrothermal synthesis of BHF nanoparticles is initiated by precipitating barium nitrate (0.62 g), iron nitrate (4.36 g), and scandium nitrate (0.35 g) in a molar ratio of 1:4.5:0.5. Approximately 72 mg/ml of SDS surfactant is added into the reaction mixture prior to heating. Once the surfactant is mixed into the precipitated solution for 30 mins, the solution is placed in an autoclave and heated to 245 °C at 3°C/min. A temperature of 245 °C was used with a heating rate of 3°C/min to replicate the experimental conditions in previously reported hydrothermal synthesis[109]. After reaching the desired synthesis temperature, the autoclave is immediately allowed to cool to 20 °C at 3 °C/min. The resultant nanoparticles were centrifuged at 201 rcf for 5 min and washed with water. The nanoparticles were dispersed in 60 ml of water and the pH was adjusted to 1.5 using nitric acid. The mixture was then heated to 100 °C for 2 h on stirring. The nanoparticles were centrifuged and washed with water and acetone to remove excess surfactant and dried at 60 °C. The dry nanoparticles were then dispersed in a solvent to create a ferrofluid at a concentration of 100 mg/ml using ultrasonication (Fisherbrand) at 35 W for 2 h.

Table 4 shows the attempted dispersion of BHF nanoparticles treated with SDS surfactant in solvents with varying polarities. Successful adsorption of the SDS surfactant molecules on the BHF nanoparticle surface can only be assumed if dispersion is successful. Objective colloidal stability analysis techniques such as zeta potential can subsequently be utilised once the BHF nanoparticles show visible signs of homogenous dispersion and show stability over a prolonged period. Visible signs of dispersion include magnetic manipulation of the BHF nanoparticles using an external magnet and an opaqueness of the ferrofluid to visible light. **Table 4** shows no correlation between increasing polarity an improved dispersion of the BHF nanoparticles in the solvent. A poor dispersion is represented by an immediate collapse of the nanoparticles as they are introduced into the solvent, even at low concentrations, with no visible benefit of sonication. This was attributed to the low polarity of these solvents and low dielectric constants which as a result cannot effectively solvate the charged sulfate groups leading to colloidal instability. **Figure 24** shows SEM results for SDS – treated BHF particles in polar solvents with a dielectric constant higher than 4.33, including, butanol, propanol, ethanol, methanol, and ethylene glycol. SEM results for all solvents show agglomerated particles, however, the nanoparticles did not show visible signs of instability

as soon as the particles were introduced into butanol analogous to the other solvents tested. In addition, sonication of the particles for a 1 h promoted dispersion of the particles to some extent in the laboratory. Long – term stability of the SDS treated BHF nanoparticles was not observed in any of the trialled solvents which could be due to little to no coverage of the SDS surfactant molecules on the BHF nanoparticles surface leading to insufficient electrostatic and steric repulsion of the particles in the solvent.

The functionalisation of BHF particles and subsequent dispersion in a variety of solvents was concluded to be unsuccessful and SDS, hence no further experiments with SDS surfactant were performed. A cationic surfactant called Hexadecyltrimethylammonium bromide (CTAB) was studied for the stabilisation of BHF nanoparticles. The experimental details for CTAB – coated BHF nanoparticles and their colloidal stability results are described below.

5.3. Experimental

Barium hexaferrite – BHF ($BaFe_{12}O_{19}$) nano-platelets were manufactured via hydrothermal synthesis from: barium nitrate (99%), nitric acid (70%) and ethylene glycol (99%) were obtained from Thermo-Fisher scientific. 1-butanol (99%), scandium (III) nitrate hydrate (99%) and iron (III) nitrate nonhydrate (98%) were obtained from Alfa-Aesar. Sodium hydroxide (98%), DBSA (95%) and CTAB (98%) were obtained from Sigma-Aldrich.

5.4. Synthesis and preparation of the ferrofluids:

Sc-substituted BHF nanoparticles were hydrothermally synthesised at 190 °C at a heating rate of 3 °C/min following a previously reported procedure[41]. A synthesis temperature of 190 °C at a heating rate of 3 °C/min was used following the results reported in chapter 4. The BHF nanoparticles were functionalised with either DBSA or CTAB (surfactant). For the preparation of BHF nanoparticles, the barium (0.62 g), iron (III) (4.36 g) and scandium (III) (0.35 g) nitrates were dissolved in deionised water in a molar ratio of 1:4.5:0.5. An excess of sodium hydroxide (26.2 g) was gradually added after which precipitation occurs and the solution was allowed to cool to room temperature. After precipitation, a solution of DBSA

(1.80 g in 25 ml of acetone), or CTAB (1.80 g in 25 ml of water, due to imporved solubility of CTAB surfactant in water), was gradually added to the reaction mixture. To produce DBSA – coated BHF nanoparticles, this mixture is allowed to stir for an additional 30 minutes whereas for CTAB – coated BHF nanoparticles, the mixture is stirred overnight. This overnight stirring of CTAB – coated BHF nanoparticles is essential to reduce the viscosity of the mixture. The autoclave was heated to 190 °C at a heating rate of 3 °C/min after which it was allowed to cool to 20 °C at 3 °C/min. Identical growth conditions were maintained for both surfactants while maintaining a low synthesis temperature to prevent surfactant degradation. Subsequently, it was confirmed that a synthesis temperature of above 150 °C is required to produce magnetically applicable BHF nanoparticles[137]. The resultant nanoparticles were centrifuged at 201 rcf for 5 min and washed with water. The nanoparticles were dispersed in 60 ml of water and the pH was adjusted to 1.5 for DBSA - coated BHF nanoparticles and 4.6 for CTAB - coated BHF nanoparticles using nitric acid. A higher pH of 4.6 is maintained for CTAB – coated BHF nanoparticles as the particles were observed to coagulate at a lower pH, possibly due to the cationic nature of the surfactant. The mixture was heated to 100 °C for 2 h on stirring. The nanoparticles were centrifuged, the DBSA coated nanoparticles were washed with water and acetone while the CTAB coated nanoparticles are only washed with water (due to reduced solubility of CTAB molecules in acetone). The DBSA coated nanoparticles were dried at 60 °C and subsequently dispersed in 1-butanol to create a ferrofluid which is herein referred to as DBSA/BHF. CTAB coated nanoparticles were dispersed in ethylene glycol without prior drying to create a ferrofluid referred to as CTAB/BHF in this report. Ultrasonication (Fisherbrand) at 35 W for 2 hours was used to disperse the dry surfactant coated nanoparticles and make up a concentration of 100 mg/ml DBSA/BHF and CTAB/BHF ferrofluid.

5.5. Characterisation of CTAB – functionalised BHF nanoparticles:

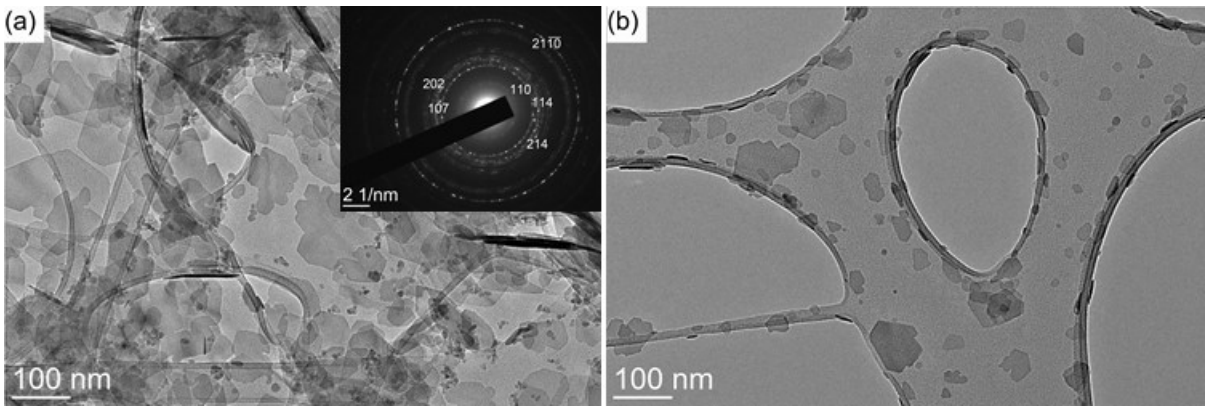

Figure 25: TEM images of the nanoplatelets coated with: (a) CTAB dried from ethylene gylcol and (b) DBSA dried form 1-butanol. Insertion in panel (a) shows SAED with indices corresponding the barium hexaferrite structure, space group $P6_3/mmc$ (194).

Figure 25 shows the Transmission Electron Microscopy – TEM scans (TEM, Jeol2100) of the (a) CTAB dried from ethylene glycol and (b) DBSA dried form 1-butanol BHF samples. A drop of the diluted suspension was deposited on a Cu-coated TEM supporting grid and left to dry. Most of the nanoplatelets lie flat on the TEM grid showing a broad distribution. The BHF particle size is defined as the maximum, or equivalent, diameter of a hexagonal particle in this report and the size distribution was determined using DigitalMicrograph® software. More than 500 particles were accounted for statistics. The CTAB-coated BHF nanoplatelets dispersed in EG had a very broad distribution of their diameters (**Figure 25**). The largest CTAB-coated BHF nanoplatelets had diameters of few hundreds of nanometres while the smallest discoids had diameters of 10 nm or less. The hexaferrite structure and ferrimagnetic order is confirmed by the Selected Area Electron Diffraction – SAED inset in **Figure 25a** with indices corresponding to barium hexaferrite structure space group $P6_3/mmc$ (194) for particles greater than 10 nm diameter while smaller particles do not evolve in the discoids[141].

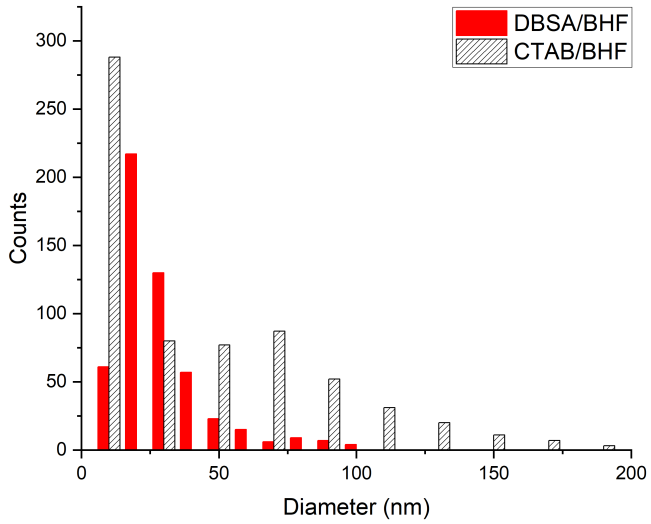

Figure 26: Diameter distribution of the nanoplatelets produced at 190 °C: CTAB/BHF dispersed in ethylene glycol and DBSA/BHF dispersed in 1-butanol.

Figure 26 shows the particle size distribution of the BHF nanoparticles DBSA/BHF and CTAB/BHF. The size distribution of DBSA coated nanoparticles shows particle diameters of up to 100 nm compared to CTAB coated nanoparticles with diameters of up to 180 nm. Samples with a broader size range were found to sediment in solvent much faster than samples with a narrow size distribution despite the electrostatic repulsion provided by the surfactant. Subsequently, it has also been observed that nanoparticles with diameters of a few hundred nanometers aggregate before sedimenting[109]. The DBSA-coated nanoplatelets dispersed in 1-BuOH also had a thickness of few nanometres but smaller diameters than the CTAB-coated nanoplatelets. The resulting mean diameter was 32 nm with a standard deviation of 26 nm for DBSA/BHF while CTAB/BHF had a mean diameter of 26 nm with a standard deviation of 52 nm.

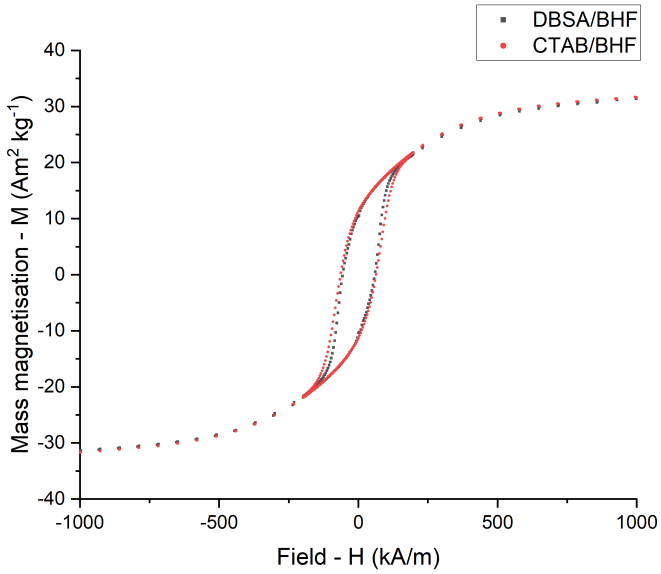

Figure 27: *Mass magnetisation – M against Applied Field – H of Barium Hexaferrite nanoparticles coated with DBSA and CTAB.*

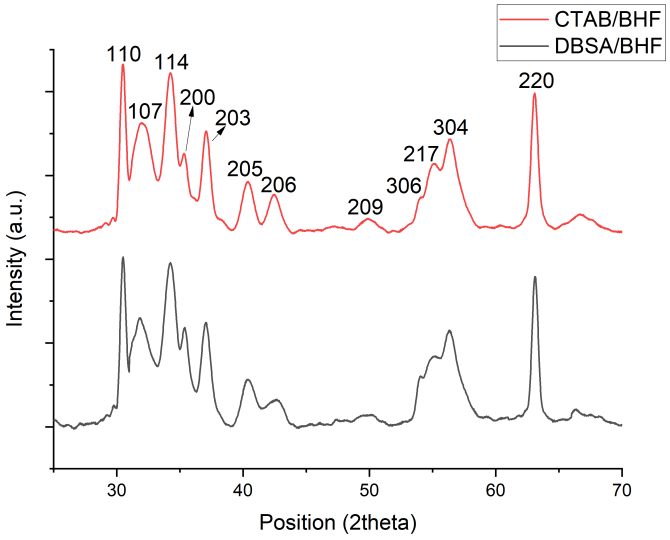

Figure 28: XRD patterns of DBSA/BHF and CTAB/BHF coated Barium Hexaferrite with labelled crystallographic planes corresponding to hexagonally crystal symmetry (space group $P6_3/mmc$) BHF nanoparticles.

The synthesised DBSA and CTAB-coated BHF nanoparticles were magnetically analysed using Vibrating-Sample Magnetometer – VSM (LakeShore 7400). The VSM samples were prepared into 3 mm wide tablets with an applied mechanical force of approximately 1000 N/mm^2 for 5 seconds. **Figure 27** shows a distinct magnetic hysteresis loop at excitation fields between -1000 kA/m and +1000 kA/m for the DBSA/BHF and CTAB/BHF dry particles which is typical of

a hard ferrimagnetic material. The pressed tablets exhibit specific magnetic remanence M_r = 10.4 $Am^2\ kg^{-1}$, coercivity H_c = 72 [kA/m] and magnetic saturation M_s = 32.8 $Am^2\ kg^{-1}$. The reported values correspond with previous findings for Sc-doped BHF nanoparticles for remancence, coercicity and saturation [21]. For comparison the crystallographic structure of dry DBSA and CTAB-coated BHF nanoparticles was analysed using X-Ray Diffraction – XRD (Panalytical Xpert Pro XRD). **Figure 28** shows the XRD diffraction patterns of DBSA and CTAB – coated BHF nanoparticles with labelled crystallographic planes. Both DBSA/BHF and CTAB/BHF show a similar diffraction pattern corresponding to hexagonally shaped BHF nanoparticles. BHF has the magnetoplumbite crystal structure and is highly anisotropic with a = 0.589 nm and c = 2.32 nm, because of which they have a preferred growth in the ab-plane with limited growth in the c-direction. The crystal structure is identified by the stacking sequence RSR*S* of the basic blocks S and R, where the asterisk denotes the rotation of the block by 180° around the hexagonal c-axis[142]. The Ba^{2+} ions within this sequence are located within the middle of the R block, while the Fe^{3+} ions occupy five different crystallographic sites within the R and S blocks. The (hk0) peaks (110) and (220) are relatively sharp which indicates the presence of large BHF nanoparticles, whereas the broad (hkl where l≠0) relate to the thickness of the nanoparticles[127]. The (hk0) peaks have a much larger intensity which agrees with the growth mechanism and TEM results in **Figure 25** showing the width of the nanoparticles being larger than the thickness (10 nm).

The Scherrer formula was used to calculate the average crystallize size of DBSA – coated BHF nanoparticles and CTAB – coated BHF nanoparticles using **Figure 28**:

$$D = \frac{k\lambda}{\beta cos\theta} \qquad (36)$$

Where, D is the average crystallite size, k is the Scherrer's constant and equals to 0.89 for the hexaferrite, λ is the x – ray wavelength and equals to 1.5405 Å, β is the width of the peak at half maximum and was extracted by direct linear interpolation at he half – maximum intensity. β is measured in radians. Finally θ is the position of the peak on the XRD spectra. Using several peaks, the average crystallite size for DBSA – coated BHF nanoaprticles was found to be 11.87 nm and the average crystallite size for CTAB – coated BHF nanoaprticles

was found to be 11.20 nm. **Figure 26**, shows the mean particle diameter of DBSA – coated and CTAB – coated BHF nanoparticles found to be 32 nm and 26 nm, respectively. In comparison, the crystallite size for both DBSA and CTAB – coated BHF nanoparticles is smaller than the particle size suggesting a polycrystalline nature[143]. This is consistent with previous studies which also found a smaller crystalline size compared to particle size for BHF nanoparticles[144].

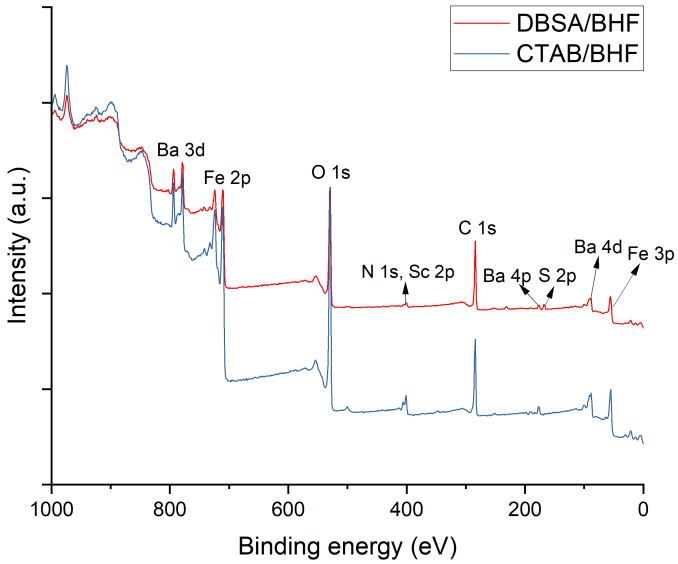

Figure 29: XPS spectra of dry DBSA and CTAB coated BHF nanoparticles

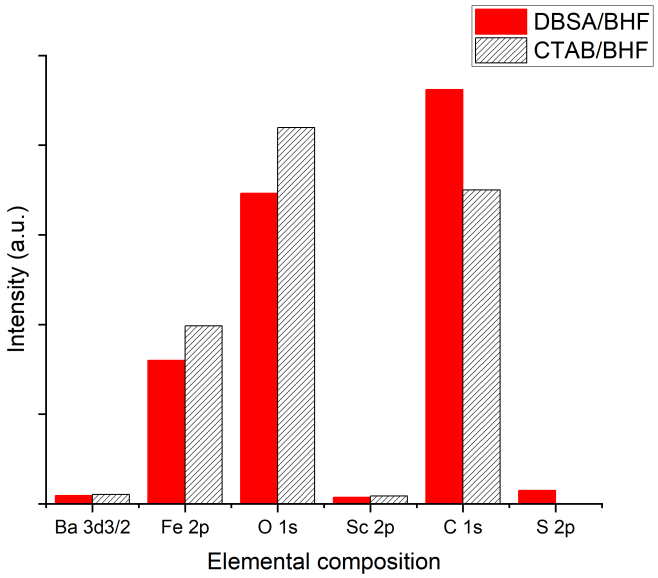

Figure 30: Surface elemental composition of dry DBSA and CTAB coated BHF nanoparticle powders

The functionalisation of both DBSA and CTAB surfactant to the surface of BHF nanoparticles can be studied using X-ray Photoelectron Spectroscopy – XPS (Kratos Axis Ultra DLD) measurements on dry nanoparticles using monochromatic AI Kα X-ray source (photon energy 1486.6 eV) operating at 120 W (10 mA x 12 kV). All samples were pressed into recesses of a modified Kratos Axis Ultra standard sample bar and pressed flat with an iso-propyl alcohol cleaned glass slides before insertion into the spectrometer. **Figure 29** shows the XPS data for both DBSA/BHF and CTAB/BHF with characteristic peaks for Ba/3d (779 eV), Fe/2p (711 eV), O/1s (530 eV), Sc/2p (402 eV) (originating from the BHF nanoparticles) and C/1s (284 eV) which is considered a reference peak. For DBSA/BHF an extra peak for S/2p (168 eV) is observed and attributed to the sulfur head group of the DBSA surfactant, this peak is not observed in the XPS data for pure BHF nanoparticles or CTAB/BHF[145,146]. For CTAB/BHF, the C - NH_2 peak corresponding to the CTAB surfactant head group occurs at 400 eV near the Sc/2p peak. XPS data for pure BHF nanoparticles generally show a carbon concentration of approximately 24%, this also increases as the surfactants adsorb onto the particle surface to 46% for DBSA/BHF and 35% for CTAB/BHF (**Figure 30**).

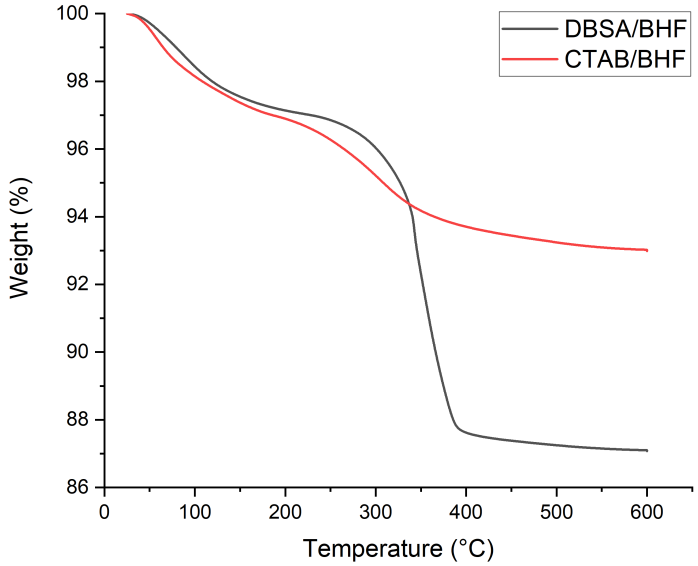

Figure 31: Thermal decomposition (TGA) curves of DBSA/BHF and CTAB/BHF powder samples heated from 25 ℃ to 600 ℃ at 10 ℃/min in air.

The thermal decomposition of DBSA/BHF and CTAB/BHF powder samples were analysed using thermogravimetric analysis – TGA (Mettler Toledo) shown in **Figure 31**. The samples

were heated from 25 °C to 600 °C at 10 °C/min under an inert atmosphere (air) with gas flow of 100 ml/min. According to **Figure 31**, the mass fraction of surfactant molecules, i.e. the total molar concentration of surfactant molecules present around the particles (c-tot), is later used to calculate the amount of surfactant molecules adsorbed onto the nanoparticle surface once dispersed in solvent. DBSA surfactant decomposed at approximately 265 °C with a mass fraction of approximately 13% while CTAB decomposes at approximately 235 °C with a mass fraction of 7% [104]. According to 6, there is also a greater increase of surface carbon for DBSA/BHF which agrees with the TGA data showing a higher average adsorption of DBSA on the BHF surface than CTAB. The Ba/Fe atomic ratio (0.05) was lower than the stoichiometric value (0.13 in $BaFe_{12}O_{19}$) which suggests that the surface of nanoparticles is rich in Fe[147].

5.6. Results and Discussion

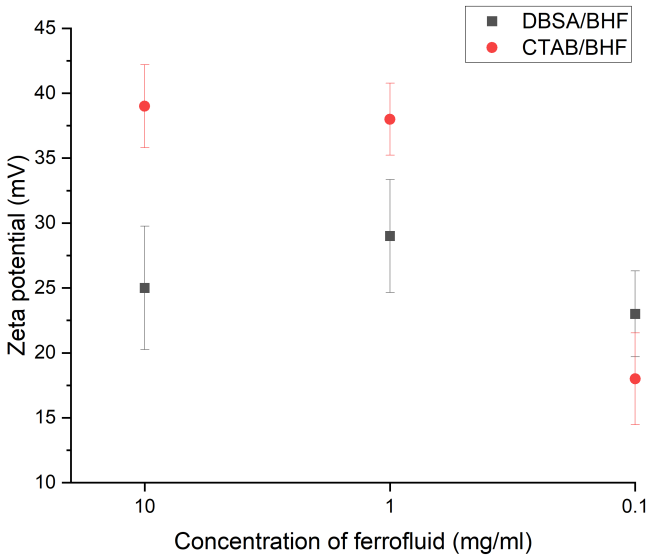

Figure 32: Zeta potential data for the DBSA/BHF ferrofluid in butanol and CTAB/BHF in ethylene glycol with standard deviation for zeta potential-measurements.

Colloidal stability is crucial for a ferrofluid because long reaching magnetic forces between individual particles quickly lead to aggregation and sedimentation. In order to compare the manufactured suspension stability, and therefore determine the quality of the ferrofluid, electrophoretic mobility and zeta potential measurements were obtained for both DBSA/BHF and CTAB/BHF products [109]. The zeta potential values of 1 mg/ml DBSA/BHF and CTAB/BHF suspensions in butanol and ethylene glycol respectively were measured on a

Malvern Nano-Z zeta analyser using a disposable capillary folding cell at an applied electric field of 20 V/mm. Equation 37 shows the Helmholtz-Smoluchowski equation used to calculate the zeta potential from electrophoretic mobility, where ζ (mV) is the zeta potential and μ_e (μmcm/Vs) is the electrophoretic mobility of the particles, η (mPa.s) is the viscosity of the medium and $f(\kappa a)$ is the Debye function set to 1.5, as follows:

$$\zeta = \frac{4\pi\eta}{\varepsilon} f(\kappa a) \cdot \mu_e \quad (37)$$

100 mg/ml samples of DBSA/BHF in butanol and CTAB/BHF in ethylene glycol were diluted with pure solvent to make 10, 1 and 0.1 mg/ml nanoparticle weight to volume concentrations for zeta potential measurements to be conducted at 25 °C. According to **Figure 32**, the zeta potential for DBSA/BHF was found to be 29.9 ± 4.4 mV and lower than the 38.3 ± 2.8 mV for CTAB/BHF ferrofluid using pure solvent permittivity and viscosity values from **Table 5**, which indicates a weaker electrostatic repulsion for DBSA coated BHF nanoparticles. The zeta potential values for both DBSA/BHF and CTAB/BHF suggest that the resulting ferrofluids are reasonably stable with the BHF nanoparticles fully dispersed in their respective carrier fluids[148]. The positive zeta potential values for both ferrofluids are due to a protonation of the surface groups at the particle - solvent interface. For the CTAB/BHF ferrofluid, the zeta potential stays constant from 1 – 10 mg/ml and significantly depletes at 0.1 mg/ml (**Figure 32**). This depletion could be due to an over-dilution of the ferrofluid leading to a lack of surfactant molecules on the surface of the BHF nanoparticles. A similar zeta potential is observed at 0.1 mg/ml for DBSA/BHF ferrofluid while there is an expectedly low zeta potential observed at 10 mg/ml with the highest value measured at 1 mg/ml.

Table 5: Electrophoretic mobility and zeta potential of the DBSA/BHF in butanol and CTAB/BHF in ethylene glycol.

Ferrofluid	Relative permittivity of the solvent ε_r [-]	Viscosity η of the solvent (mPa.s)	Conductivity (μS/cm)	$\boldsymbol{\mu_e}$ (μm cm/Vs)	$\boldsymbol{\zeta}$ (mV)
DBSA/BHF	17.6	2.6	$0.00108 \pm 0.001\%$	0.221	29.9 ± 4.4

CTAB/BHF	37.0	16.2	$0.00252 \pm 0.001\%$	0.080	38.3 ± 2.8

The surface modification of the BHF nanoparticles with a layer of surfactant allows for the formation of a stable colloidal suspension. The surfactant molecules are adsorbed onto the nanoparticle surface which is created through dissociation of the surfactant head group counterion in water during the synthesis stage. To determine the quantity of the CTAB surfactant adsorbed onto the BHF nanoparticle surface and the amount dissolved in the ethylene glycol liquid carrier, the molar concentration of dissolved CTAB surfactant (c-dis) was determined through electrical conductivity σ (μS/cm) measurements (Mettler Toledo, LE703). The conductivity of CTAB/BHF in ethylene glycol and DBSA/BHF in butanol was measured at 10 and 100 mg/ml at room temperature. The amount of dissolved CTAB c-dis was determined through an addition method by gradually adding equal amounts of powder CTAB surfactant into the suspension while continuously stirring the solution. The conductivity was measured after each addition of surfactant and found to linearly increase with the increase of c-dis. The linear equation $\sigma = a + (b \times (\Delta c\text{-dis}))$ was used to calculate c-dis as a quotient of 'a' and 'b' (**Table 6**). The amount of CTAB surfactant adsorbed (c-ads) on the surface of the BHF nanoparticles was calculated from the difference between the total molar concentration of CTAB (c-tot) and c-dis. The mass fraction of CTAB in a known sample mass of dry BHF nanoparticles was determined by TGA for adsorbed surfactant calculations. Conductivity measurements (**Table 6**) for CTAB/BHF ferrofluid show that c-ads is unaffected by concentration and the ratio of c-ads/c-tot remains 0.85 for 10 and 100 mg/ml. This is consistent with the zeta potential for CTAB/BHF ferrofluid being constant for 1 – 10 mg/ml, as the amount of CTAB surfactant on the BHF nanoparticle surface remains the same. On the other hand, c-ads varies between concentrations for DBSA/BHF ferrofluid as the ratio of c-ads/c-tot at 100 mg/ ml was comparable with CTAB/BHF but significantly lower at 10 mg/ml. This indicates that the CTAB surfactant is more strongly bonded to the BHF nanoparticle surface than DBSA as the dilution of ferrofluid does not increase c-dis. However, visual observations of both DBSA/BHF and CTAB/BHF ferrofluids remain stable between 10 – 100 mg/ml indicating other factors such as dielectric constant of solvent, particle size distribution, and an equilibrium between c-dis and c-ads ensure stability of ferrofluid.

Table 7 shows the surface area (nm^2) covered by a single molecule of DBSA and CTAB surfactant on a BHF particle. The surface area per surfactant molecule (nm^2) was calculated using equation 38 and equation 39 and the c-ads values (**Table 6**) for DBSA and CTAB surfactants. The dimensions of the BHF were assumed to be 100 nm diameter with a 10 nm thickness for simplicity and the particle surface area of a BHF particle was approximated as a cylinder. The calculated surface area covered by a single molecule of DBSA and CTAB (**Table 7**) are much smaller than the expected molecular footprint of a long – chain surfactant like DBSA and CTAB[149]. This supports the idea that a likely multi – layer of the DBSA and CTAB surfactant exists around the BHF particles for their stabilisation in 1 – butanol and ethylene glycol, respectively.

$$surface\ coverage = \frac{number\ of\ DBSA\ molecules}{total\ surface\ area\ of\ a\ particle} \qquad (38)$$

$$area\ occupied\ by\ one\ surfactant\ molecule = \frac{1}{surface\ coverage} \qquad (39)$$

Table 6: Concentrations of the dissolved (c-dis) and adsorbed (c-ads) DBSA/BHF in 1-butanol and CTAB/BHF in ethylene glycol suspensions at 10 and 100 mg/ml.

	c-dis (mM)		c-ads (mM)		c-ads/c-tot	
Ferrofluid concentration (mg/ml)	DBSA/BHF	CTAB/BHF	DBSA/BHF	CTAB/BHF	DBSA/BHF	CTAB/BHF
10	2.5	0.37	1.21	1.99	0.32	0.85
100	6.1	3.57	26.2	19.6	0.81	0.85

Table 7: surface area (nm^2) covered by single molecule of DBSA and CTAB surfactant on BHF particle.

Ferrofluid concentration (mg/ml)	c-ads (mM) for DBSA	Area per surfactant molecule (nm^2) for DBSA	c-ads (mM) for CTAB	Area per surfactant molecule (nm^2) for CTAB
10	1.21	9.52×10^{-4}	1.99	5.77×10^{-4}
100	26.2	4.41×10^{-4}	19.6	5.88×10^{-4}

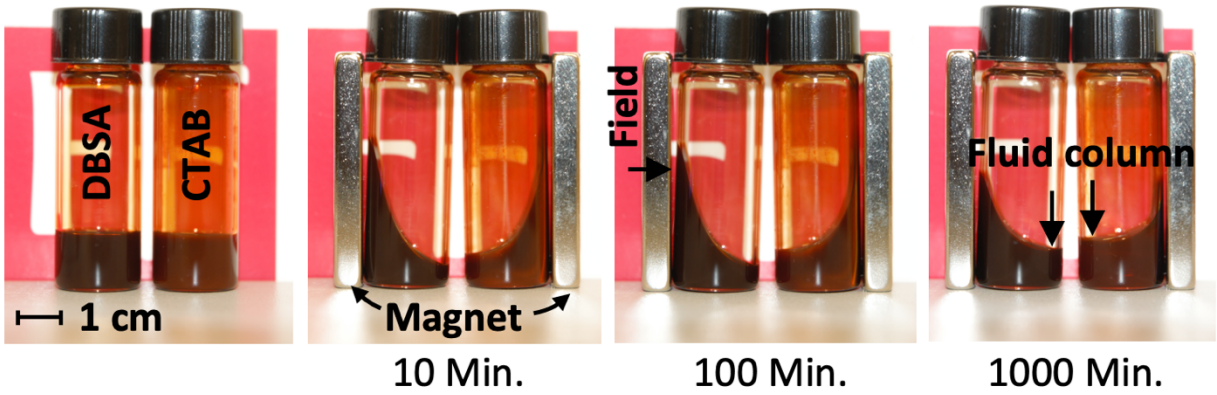

Figure 33: Experimental destabilisation times of DBSA/BHF and CTAB/BHF ferrofluid (40 mg/ml) exposed to a permanent magnetic field (0.3 T).

Figure 33 shows a simple visual experiment to compare the stability of both CTAB/BHF and DBSA/BHF ferrofluids which was conducted by exposing the ferrofluids to a strong permanent external magnetic field and inspecting the time it takes to separate magnetic nanoparticles from the liquid carrier. The experiment was carried out by placing a permanent magnet (permanent external magnetic field = 0.3 T) against the side of each vial filled with the synthesised ferrofluid which attracts most of the ferrofluid creating a vertical sloped gradient perpendicular to gravity acting downwards. A concentration of 40 mg/ml was selected where the magnetic energy is equal to the gravitational energy creating a gradual slope. This slope shortens overtime while the volume of the carrier fluid rises at the bottom of the vial as the BHF nanoparticles precipitate out of the medium. For an identical volume of 1 ml and concentration of 40 mg/ml for DBSA/BHF – butanol and CTAB/BHF – ethylene glycol ferrofluid, the height of the carrier fluid remaining at the bottom of the vial after 1, 10, 100, and 1000 minutes were determined from photographs, and taken as a relative indicator of destabilisation over time when exposed to an external magnetic field. Although both ferrofluids show destabilisation at each increment measured, it can be argued that despite difference in carrier fluid viscosity the DBSA/BHF ferrofluid is more stable as it showed a smaller rise in carrier fluid column from 1 – 100 minutes, compared to CTAB/BHF. Overall, both DBSA/BHF and CTAB/BHF showed a gradual destabilisation from 1 – 100 minutes meaning that the BHF nanoparticles retained some degree of dispersion within their carrier fluids. After 1000 minutes, both ferrofluids were mostly destabilised only showing a shallow gradient compared to the image taken after 10 minutes but can be redispersed by sonication. Finally, the CTAB/BHF ferrofluid in ethylene glycol has a boiling

temperature of 197.35 °C exhibiting superior thermal properties compared to DBSA/BHF ferrofluid in butanol with a boiling temperature of 117.45 °C[150]. Since ethylene glycol is commonly used as a plasticizing agent, automotive antifreeze, and other heat transfer applications the proposed ferrofluid can be explored in various real world engineering applications. Finally, ethylene glycol also has a low vapour pressure and low volumetric expansion coefficient potentially opening the way into new ferrofluid applications.

5.7. Conclusions

A new barium hexaferrite (BHF) based ferrofluid was developed and stabilised using hexadecyltrimethylammonium bromide (CTAB) surfactant through electrostatic and steric repulsion. Dry hexadecyltrimethylammonium bromide coated barium hexaferrite nanoparticles with an average size up to 200 nm were characterised using powder X-ray diffraction (XRD), Transmission Electron Microscopy (TEM), Thermogravimetric Analysis (TGA), and Vibrating-Sample Magnetometer (VSM) techniques. Surface properties of the nanoparticles was analysed through X-ray Photoelectron Spectroscopy (XPS). Despite differences in size distribution and surface properties, the synthesised nanoparticles exhibit identical magnetic properties compared to previously reported dodecyl benzene sulphonic acid (DBSA) coated nanoparticles. Subsequently, the surfactant coated barium hexaferrite nanoparticles were dispersed in ethylene glycol to create a ferrofluid and the colloidal stability was measured using zeta potential and compared with that of a butanol ferrofluid at different concentrations. Zeta potential for hexadecyltrimethylammonium bromide coated nanoparticles was consistently higher than dodecylbenzenesulfonic acid coated barium hexaferrite nanoparticles at the same concentration. Through conductivity measurements, hexadecyltrimethylammonium bromide was found to be more strongly bonded to the nanoparticle surface than dodecylbenzenesulfonic acid as the amount of surfactant adsorbed stays consistent despite dilution of the ferrofluid. Colloidal stability is best observed in the laboratory through identifying signs of sedimentation and flocculation of nanoparticles with and without the presence of an external magnetic field. Both hexadecyltrimethylammonium bromide and dodecylbenzenesulfonic acid coated barium hexaferrite nanoparticles produce ferrofluids that are stable for a sufficiently long period of

time. The applicability of both ferrofluids can be compared with regards to their carrier fluid, as the proposed ethylene glycol solvent is much more useful than previously reported butanol because of its higher boiling point and miscibility in water, whereas butanol is an extremely volatile solvent and has limited miscibility in water. This ensures the potential for a variety of applications for barium hexaferrite ferrofluids stabilised with hexadecyltrimethylammonium bromide as opposed to dodecylbenzenesulfonic acid surfactant because of its stable dispersion in ethylene glycol. Since the exchange of carrier fluids also has rheological implications, future work also includes rheological measurements for ethylene glycol based BHF ferrofluids.

Chapter 6: In-Situ Polymerisation of Barium Hexaferrite Ferrofluids for Poly(Ethylene) Succinate Magnetic Nanoparticle Composites

Chapter 6 presents a magnetic polymer composite material manufactured from the CTAB/BHF ferrofluid in ethylene glycol presented in chapter 5. The novelty of the results obtained arise from the useful physical and thermal properties of ethylene glycol as a solvent. The high boiling point of ethylene glycol allowed a condensation polymerisation of the CTAB/BHF ferrofluid to produce a Polyethylene succinate (PES) matrix with homogenously integrated BHF nanoparticles. The biodegradable and biocompatible properties of the PES polyester combined with the hard magnetic properties of BHF nanoparticles is extremely exciting for future investigations. Additionally, the synthesised thermoplastic polymer composite shows excellent magnetic properties, opening the way to advanced 3D magnetic printing and biomedical applications.

6.1. Introduction

Magnetic composite materials have magnetic particles embedded in a continuous polymer matrix and combine properties which are not possible in a single phase, such as a hard magnetic moment in a malleable and lightweight polymer structure[151]. Recent advances in magnetic particle and polymer synthesis enable a wider range of applications including three dimensional (3D) printing[152], self-healing materials[153], environmental and process

engineering[154], and biology[155]. Magnetic nanocomposites, where at least one geometry dimension is in the nanometre range, are of particular interest due to the high level of dispersion leading to a homogeneous, or isotropic, composite material. The dispersion of magnetic particles within the matrix occurs by counteracting the attractive interactions between the particles through electrostatic and steric repulsive forces through the incorporation of stabilising agents, such as surfactants, during the synthesis process. While the dispersed particles exhibit application specific properties, the polymer matrix also contributes to the material processability and performance[156].

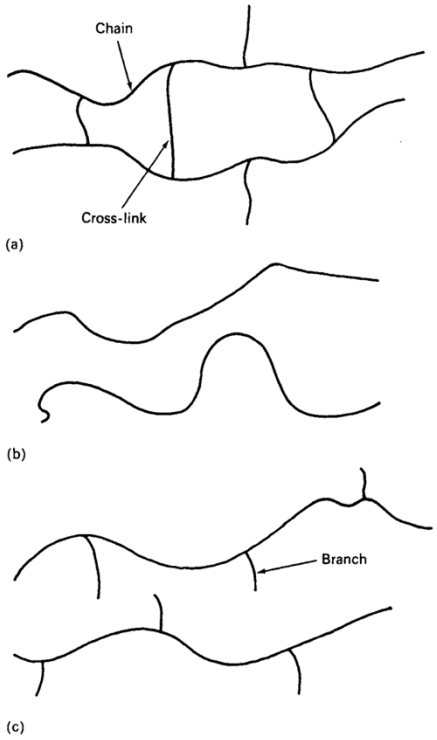

Figure 34: Cross – linking or strong covalent bonds between polymer chains (a), linear polymer chains without cross - linking (b), and branched polymer chains (c)[157].

Different types of polymer matrix composites (PMCs) are available such as thermosets, thermoplastics, or rubbers with thermosetting polymers being the most common. Thermosetting polymers readily form cross – links (**Figure 34a**), or strong covalent bonds between polymer chains, which restricts movement and consequently increases the glass transition temperature to above room temperature and prevents the remoulding of PMCs which can burn, or degrade, upon reheating. Thermoplastics differ from thermosets by

forming linear (**Figure 34b**) or occasionally branched (**Figure 34c**) polymer chains (which do not cross-link and readily flow under stress at high temperatures. This property allows for remoulding of the PMC and retain the given shape upon cooling to room temperature[158]. Most thermoplastic PMCs are iron oxides and iron – based materials due to their easy preparation and good stability. For iron oxide PMCs, the dispersion and polymer fabrication has been intensively researched for the purpose of improved stability and magnetorheological properties. Guo et *al*. reported improved Fe_3O_4 – PMMA stability through core shells in advanced magnetorheological materials[159,160]. This produced high magnetic susceptibility and low – density iron oxide PMCs demonstrating a low level of toxicity. Further improvements on biocompatible PMCs was reported for polymer shell type hybrid particles which prevent a direct contact between the magnetic nanoparticles and biomolecules, and can also be coated with bioactive targeting molecules[161] for applications in enzyme immobilisation[162], magnetic resonance imaging[163], and drug delivery cell separation[164]. In an effort to improve dispersion, magnetic fiber composites were homogeneously dispersed with Fe_3O_4 magnetic nanoparticles in polyvinyl alcohol (PVA) with the help of polyacrylic acid (PAA) acting as a polymer surfactant[165]. Traditionally, these magnetic fibers are produced by coating magnetic nanoparticles onto the surface of the fibers, however, this results in a low magnetic susceptibility due to insufficient amounts of magnetic nanoparticles as well as particle loss after treatment[166]. Similar approaches were reported by incorporating the magnetic nanoparticles directly into a polymeric fiber matrix by mixing, however, the challenge of obtaining well-dispersed nanoparticles without aggregation still remains[167] due to the short-range van der Waals forces and long-range magnetic dipole – dipole interactions between the particles causing aggregation and effectively separation of the two phases[109]. In contrast, isotropic composites can be produced directly from colloidal suspensions through *in-situ* polymerisation. Fe_3O_4 magnetic nanoparticles were homogeneously dispersed with a PAA polymer surfactant into Fe_3O_4/PVA composite materials. However, due to the superparamagnetic properties of Fe_3O_4, these composites have limited applicability. In contrast, ferrimagnetic Barium hexaferrites (BHF) exhibit a high uniaxial magnetocrystalline anisotropy ($K_i = 3.3 \times 10^4$ J.m^{-3}) with the magnetic easy axis parallel to the crystallographic c-axis, producing a high coercivity[168] used for permanent magnets, magnetic-recording media, and microwave applications[169]. Previous studies utilising *in-situ* polymerisation with BHF reported a maximum filler content of 0.27

wt% in PMMA[170]. The filler content of BHF depends mainly on the stability of the colloidal suspension determined by the Brownian motion of the suspended nanoparticles and their geometrical and magnetic-anisotropy[21]. BHF nanoparticles exhibits a hexagonal shape shown by Went et *al.* and their diameter depends on the synthesis method used. When in suspension, BHF particles also exhibit interesting nematic transitions and domain formations in isotropic liquids[171] and novel magneto-optical properties for magnetic field visualisation[172], or optical coherence tomography[36]. In addition, these fluids potentially have a wide range of commercial applications covering industrial coolants, sealants, light switches, hyperthermia, defect sensors, and drug targeting[173]. For this reason, ferrimagnetic scandium substituted barium hexaferrite - $BaFe_{12}O_{19}$ (BHF) nanoparticles were utilised in order to produce a novel polymer matrix nanocomposite material with hard magnetic properties. In this work, BHF magnetic nanoparticles were coated with hexadecyltrimethylammonium bromide (CTAB) surfactant which allows for a stable colloidal dispersion of BHF in ethylene glycol[174]. To take advantage of the high boiling point and functional groups of ethylene glycol solvent, a catalyst–free, direct *in–situ* condensation polymerisation reaction of the ethylene glycol ferrofluid was conducted to produce poly(ethylene) succinate (PES) with embedded barium hexaferrite magnetic nanoparticles. The PES synthesis for the barium hexaferrite PMC is developed and optimised in this report followed by the chemical and magnetic characterisation of the product. Based on the here reported synthesis method, novel direct *in-situ* thermoplastic hard magnetic PMCs are developed with potential applications in three dimensional (3D) magnetic structures or advanced bioengineering applications.

6.2. Methodology

Synthesis of magnetic nanoparticles: Sc-substituted BHF nanoparticles were hydrothermally synthesised at 190 °C following a previously reported procedure[41]. The barium (0.62 g), iron (III) (4.36 g) and scandium (III) (0.35 g) nitrates were dissolved in deionised water in a molar ratio of 1:4.5:0.5. An excess of sodium hydroxide (26.2 g) was gradually added after which precipitation occurs and the solution was allowed to cool to room temperature. After precipitation, a solution of CTAB (1.80 g in 25 ml of water) was gradually added to the

reaction mixture. The mixture was allowed to stir overnight. This overnight stirring of CTAB – coated BHF nanoparticles is essential to reduce the viscosity of the mixture. The autoclave was heated to 190 °C at a heating rate of 3 °C/min after which it was allowed to cool to 20 °C at 3 °C/min. The resultant nanoparticles were centrifuged at 201 rcf for 5 min and washed with water. The nanoparticles were dispersed in 60 ml of water and the pH was adjusted to 4.6 using nitric acid. The mixture was heated to 100 °C for 2 h on stirring. The nanoparticles were centrifuged and then washed with water. The moist CTAB surfactant coated nanoparticles were dispersed in ethylene glycol (99.8 %, Thermo Fisher Scientific) and sonicated for 2 hours at 35 W producing a concentrated (100 mg/ml) BHF ferrofluid. *Polymerisation of CTAB – stabilised ferrofluid:* CTAB-stabilised BHF ferrofluid was heated to 170 °C in an oil bath with continuous stirring, while succinic acid (99.9%, Thermo Fisher Scientific) was gradually added in a 1:2 molar ratio (succinic acid to ferrofluid). The ferrofluid (65 mg/ml) mixture was maintained at 170 °C with stirring for 10 hours, producing PES/BHF (93 mg/ml) and H_2O as follows:

$$[-O-(CH_2)_2\ -OOC-(CH_2)_2\ -CO-]\ n\ \text{(polyethylene succinate)} + nH_2O \qquad (40)$$

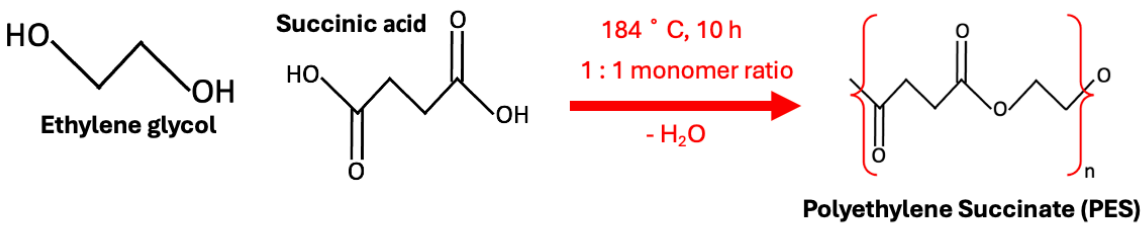

Figure 35: polycondensation reaction between ethylene glycol and succinic acid to produce polyethylene succinate (PES) at a temperature of 184 °C for 10 h and a 1 : 1 monomer ratio.

Equation 40 shows the checimal bonds in the repeating unit of PES and **Figure 35** shows the polycondensation reaction mechanism between ethylene glycol and succinic acid to produce PES. After the product was cooled at room temperature it produced a solid polyethylene succinate polymer with hard magnetic properties. The condensation polymerisation reaction between succinic acid monomers and ethylene glycol produces polyethylene succinate and requires the elimination of water to form covalent bonds between the monomers. This catalyst-free and direct *in–situ* condensation polymerisation reaction creates a stable

thermoplastic PMC while maintaining subsequent dispersion, molecular weight, and magnetic properties over several heating and cooling cycles. The thermoplastic PES is first optimized for the synthesis method with a pure PES matrix followed by varying the nanoparticles concentration of the PMC. The synthesis of the polyethylene succinate matrix was optimised for synthesis time and synthesis temperature. For the optimisation of synthesis temperature, ethylene glycol was polymerised with succinic acid at 110, 130, 150 and 170 °C. As previous studies[175] have found, the melting point of succinic acid is 184 °C, while the boiling point of ethylene glycol and succinic acid is 205 °C and 255 °C, respectively. For this reason, it is important to stay below the boiling temperature of ethylene glycol and succinic acid as well as above the boiling temperature of water. The ratio of succinic acid and ethylene glycol is also paramount for the polymerisation reaction. To determine a suitable molar ratio of the monomers to use, findings from previous literature were utilised which report the solubility of succinic acid with respect to temperature. These studies conclude that the solubility of succinic acid in all the studied solvents increases with an increase in temperature. Our preliminary studies following a similar protocol confirmed up to 50% of succinic acid solubility in ethylene glycol when heated to 80 °C (just below the boiling point of water)[176]. The pure PES matrix was characterised using Fourier Transform Infrared (FTIR) spectroscopy, Gel-Permeation Chromatography (GPC), and Nuclear Magnetic Resonance (NMR) spectroscopy to analyse the molecular weight as well as the monomer to polymer conversion as the polycondensation time and temperature was increased. The polymer molecular weight (M_n) was determined using the following equation:

$$M_n = \frac{\sum N_i M_i}{\sum N_i} \quad (41)$$

where N_i is the number of molecules of species i, and M_i is the molecular weight of species i[177]. In addition, surface hardness of the polymers, a key mechanical application property, was also measured with reaction time. After optimising the synthesis of the pure polymer matrix, the same method was followed for the polymerisation of magnetic barium hexaferrite based ferrofluids. Different concentration of bulk ferrofluid samples were polymerised and characterised using Thermogravimetric Analysis (TGA) and Vibrating

Sample Magnetometry (VSM) analysis while sliced microtome sliced samples were sliced for Transmission Electron Microscopy (TEM).

It should be noted that the polymerisation of CTAB/BHF ethylene glycol ferrofluid was also investigated with succinic chloride as opposed to succinic acid. The same methodology described above was used, including molar ratio, synthesis time and synthesis temperature. Succinic chloride has Cl atoms as opposed to OH on its outer carbons, hence a condensation polymerisation reaction with succinic chloride would produce HCl as opposed to H_20. This release of HCl is extremely damaging to the magnetic nanoparticles and was found to physically break down the particles in the reaction. Hence, succinic acid is a much more suitable monomer for the polymerisation of CTAB/BHF ferrofluid.

6.3. Results and Discussion

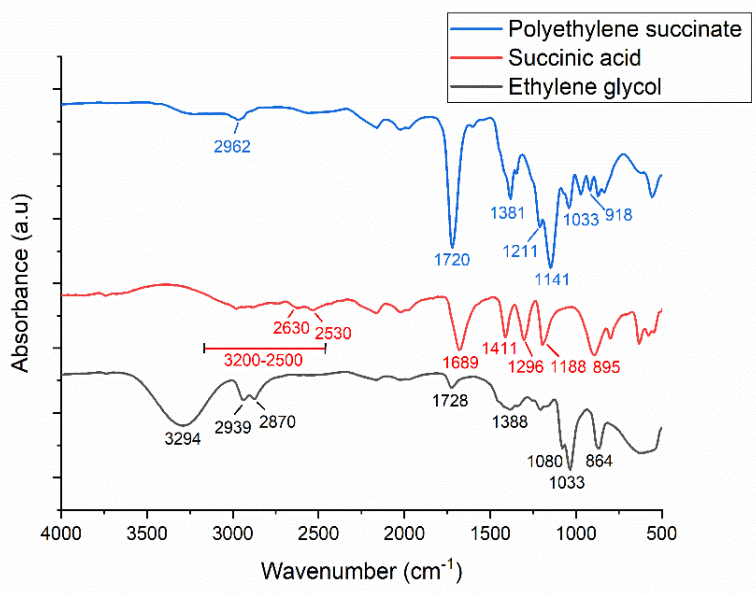

Figure 36: FTIR analysis of ethylene glycol, succinic acid, and pure polyethylene succinate (PES).

According to **Figure 36**, FTIR analysis confirms for pure PES a successful polymerisation reaction between the succinic acid and the ethylene glycol monomers. The main characteristic peaks of succinic acid are 3200 – 2500 cm^{-1} which correspond to the broad stretching vibration of the O – H group, 2630 and 2530 cm^{-1} are due to the C – H stretching, while the peak at 1689 cm^{-1} corresponds to the C = O group stretching vibration and the

peak at 895 cm^{-1} results from the out of place bending of the bonded -OH group of the carboxylic acid[175]. The peaks at 1411 and 1296 cm^{-1} were due to C – O – H in plane bending ($\delta_{C\text{-}O\text{-}H}$) and C – O stretching vibration, respectively[178]. The FTIR results for ethylene glycol show the main characteristic peaks which include, 3294 cm^{-1} due to the OH group stretching vibration and the peaks at 2939 and 2870 cm^{-1} which are assigned to the asymmetric and symmetric stretching of C – H bonds. The peak at 1388 cm^{-1} results from the CH_2 bending while nearby peaks correspond to C – O – H bending. The peaks at 1080 and 1033 cm^{-1} are due to the C – O stretching and the peak at 864 cm^{-1} corresponds to the CH_2 rocking[179]. Most importantly, the peak at 1720 cm^{-1} signifies the formation of the ester bond, which is absent in both monomers, specifically, C = O group stretching vibration. This is coupled with the disappearance of the C = O group stretching vibration of succinic acid and OH group stretching vibration of ethylene glycol which also confirms a successful condensation polymerisation reaction. Additionally, for pure PES, peaks 1141 and 1211 cm^{-1} were attributed to the stretching vibration of the (– C – O – C –) group in the ester bond of PES polymer. The peaks at 1033 and 918 cm^{-1} are due to the (– O – C – C –) stretching vibrations and (– C – OH) bending in the carboxylic acid groups of PES, respectively. Furthermore, the peaks at 2962 cm^{-1} correspond to the asymmetric stretching vibration while 1381 cm^{-1} correspond to the symmetric deformational vibrations of the – CH_2 – groups present in the main carbon chain of PES polymer[180].

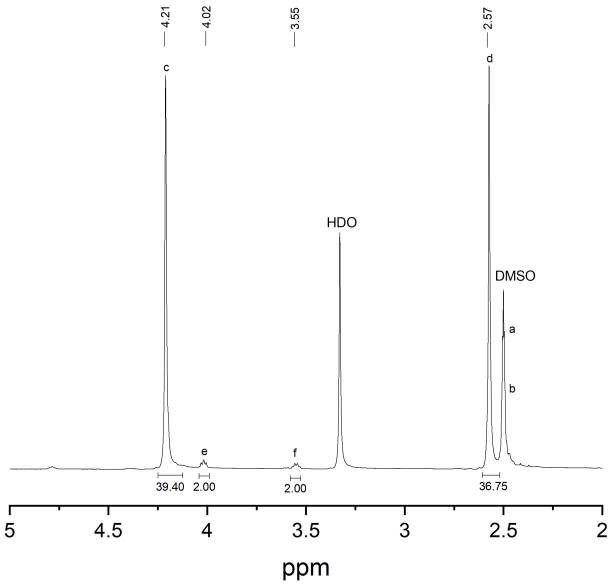

Figure 37: ^1H NMR spectra of pure PES polymer synthesised at 170 ℃ for 10h

In order to determine an optimised synthesis temperature and time, pure PES products were characterised by ^{1}H NMR spectroscopy at room temperature in DMSO – d_6. Chemical shifts are reported in ppm (δ scale) relative to tetramethylsilane (TMS). Approximately 1 – 5% w/v of pure PES polymer solutions were used for the ^{1}H NMR measurements. The degree of polymerisation or number of units can be determined by comparing the relative proton signal intensity of a known moiety (typically an end group (s) with a known number of protons), to the proton signal intensity of the repeating unit in the polymer chain. The molecular weight of pure PES was probed as a function of increasing polycondensation time. The optimal polymerisation reaction time was estimated by setting up the polymerisation reaction at 170 °C under magnetic stirring with samples extracted every 5 hours for 60 hours. The extracted samples were analysed using NMR and GPC. **Figure 37** shows the partial ^{1}H NMR spectrum for pure PES produced under these conditions for 10 hours. The ^{1}H NMR spectra shows signals assigned to the end group as well as the repeating units in the polymer chain. The singlet at 4.21 (δH^{c}) ppm was assigned to the methylene protons on the ethylene glycol monomers in the repeating unit. The singlet at 2.58 (δH^{d}) ppm was assigned to the methylene protons on the succinic acid monomers in the repeating unit. The triplet signals observed at 4.02 (δH^{e}) and 3.55 (δH^{f}) ppm can be assigned to the CH_2 protons on the end group ethylene glycol monomers. Likewise, the methylene protons on the end group succinic acid monomers give overlapping signals (δH^{a} and δH^{b}) with that of the solvent between 2.46 and 2.53 ppm. ^{1}H NMR of pure succinic acid and ethylene glycol monomers differ greatly from the ^{1}H NMR of pure PES, indicating the formation of polymer bonds and repeating units. The ^{1}H NMR spectra of pure succinic acid monomer in DMSO – d_6 shows singlets at 12.2 ppm and 2.4 ppm representing the carboxylic acid group and CH_2 protons respectively. Additionally, the ^{1}H NMR for pure ethylene glycol show two singlet peaks at 3.3 ppm corresponding to the CH_2 protons and 4.5 ppm assigned to the OH groups.

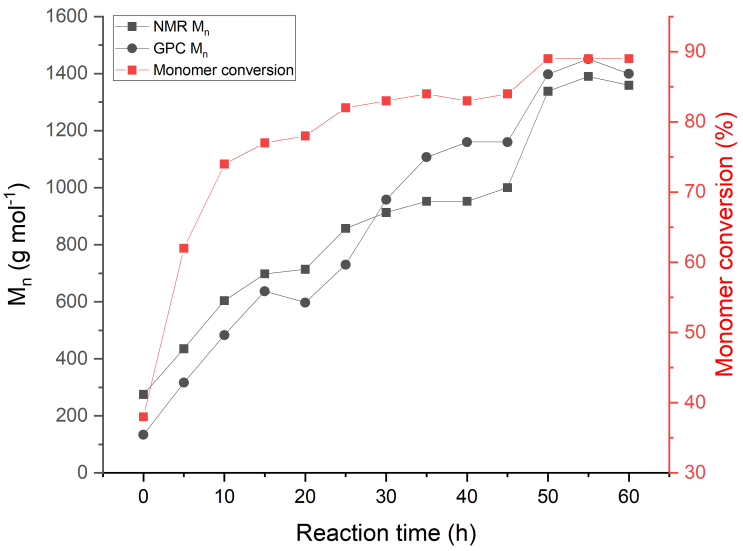

Figure 38: *monomer conversion (equation* 41*) data obtained from NMR analysis changing with reaction time and molecular weight data obtained from NMR and GPC of pure PES polymer chains as a function of reaction time.*

To further analyse the polymerisation progression with reaction time, the monomer to polymer conversion was calculated at each hour. This was determined by comparing specific monomer proton integrals with the corresponding proton integrals in the repeating unit. According to **Figure 38**, up to 91 % of ethylene glycol and succinic acid monomers are converted to polyethylene succinate as the synthesis time is increased. In addition, the NMR and GPC analysis demonstrates that the molecular weight gradually increases with synthesis time due to the step-growth mechanism. The data indicates that the polycondensation method produced relatively low molecular weight polyester chains from initially M_n = 275 to M_n = 1359 g mol^{-1} after 60 hours; low molecular weights are routinely observed for step-growth polycondensation polymerisation unless very high conversions are attained because the condensation leads to the formation of dimers, then trimers, oligomers, and eventually long-chain polymers. In our case, 1-8 repeat units are incorporated into the polymer chains. The number of repeating units in the polymer chain was calculated by dividing the relative molecular mass of polymer obtained by the relative molecular mass of 1 repeating unit. There is a general increase in molecular weight and monomer conversion as the polycondensation reaction time increases, with a significant increase in monomer conversion and molecular weight after 10 hours. However, the monomer conversion after 60 hours is only 15% higher than conversion after 10 hours leading to diminishing gains in

conversion efficiency. The molecular weight of the polyesters was also measured using GPC with respect to polycondensation reaction time. Similar to NMR, the GPC data showed a gradual increase in molecular weight as the reaction times increases. The polymer M_n data obtained from GPC are comparable to the molecular weight data derived from NMR, with M_n ranging from 134 to 1399 g mol^{-1} corresponding to 1–8 repeat units. After 50 hours of reaction time, both GPC and NMR show negligible difference in the molecular weight despite further heating. However, the molecular weight data obtained from GPC has a strong dependence on the calibrant (typically polystyrene) which can be a hinderance as it is assumed that the measured polymer and the standard have the same hydrodynamic radii at equivalent molecular weight. Hence, the underlying principle of the technique is separation on the basis of polymer hydrodynamic volume instead of molecular weight[181,182]. In comparison, ^{1}H NMR spectroscopy is our primary quantitative method for analysis without the need for calibration[183].

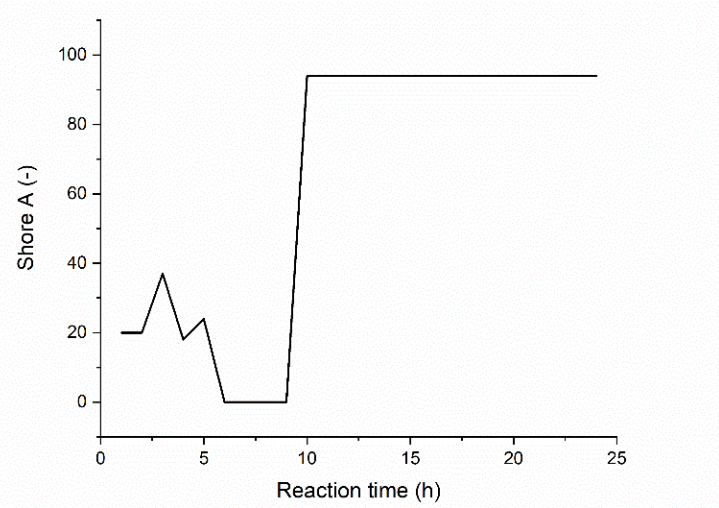

Figure 39: Surface hardness of PES in response to reaction time of polymerisation.

The pure PES synthesis produced a yellow/brown, waxy polymer from the transparent reactants which indicates the polycondensation of the initial monomers and the formation of the polyester molecules. Supplementary Information 1 confirms a gradual yellow/brown change from the transparent reactants over 60 hours. The final pure PES product is a thermoplastic which can be heated to become highly viscous and subsequently cooled to reshape. The mechanical properties of the pure PES polymer was measured using a shore A hardness probe on 25 mm thick PES samples that were cooled to room temperature. Ethylene glycol and succinic acid monomers were polymerised at 170 °C, and samples were

extracted from the batch every hour for 24 hours. The surface hardness of each extracted sample is shown in **Figure 39**. A significant peak was observed in surface hardness of the pure PES polymers at hour 10 which showed a value of 90 on the Shore A hardness scale. Below 10 hours of heating, the co – polymers are not fully reacted, and the polymer is a soft, waxy material. After 10 hours of reaction time, the surface hardness of the PES material stays constant despite prolonged polymerisation time. Hence, 10 hours polymerisation time was considered optimal for the synthesis of a polyethylene succinate matrix as it presents good monomer conversion and mechanically hard polyesters with sufficient molecular weights. In addition, extended heating periods at high temperatures have the potential to destabilise the BHF suspension. Having said this, the polymers produced below 150 °C for a period of 10 hours have a brittle structure and can easily fracture.

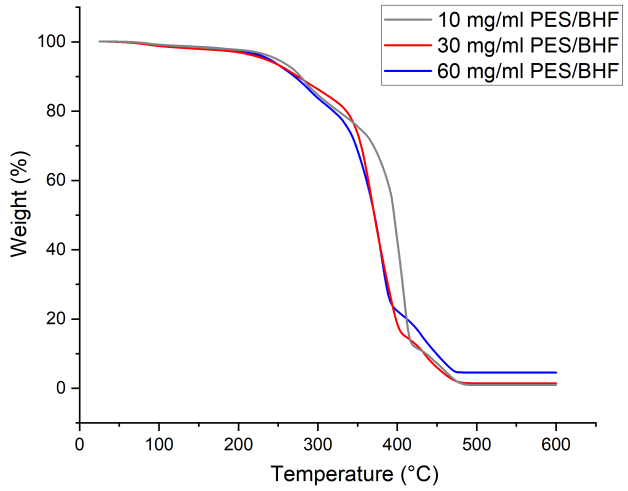

Figure 40: TGA analysis of PES/BHF polymer composite matrix at 10 mg/ml, 30 mg/ml and 60 mg/ml

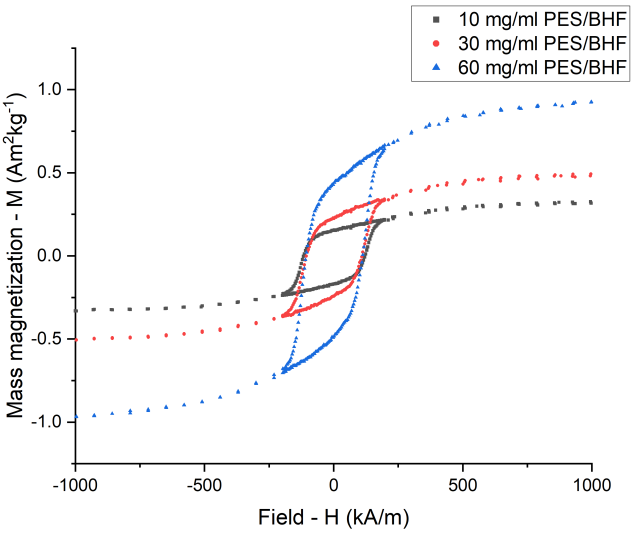

Figure 41: mass magnetisation – M against applied field – H of BHF nanoparticles embedded in a PES polymer matrix at concentrations of 10 mg/ml, 30 mg/ml and 60 mg/ml.

Based on the identified 10 hours and 170 °C synthesis conditions for the PES polymer matrix, the polycondensation reaction was repeated with a barium hexaferrite based ferrofluid where the magnetic nanoparticles are stabilised using CTAB surfactant and suspended in ethylene glycol. This ethylene glycol ferrofluid reacted with succinic acid to produce a PES/BHF polymer composite exhibiting magnetic properties from the suspended nanoplatelets. Here, the ethylene glycol suspended barium hexaferrite magnetic nanoparticles reacts with the succinic acid to produce a polyethylene succinate polymer matrix. The BHF nanoparticles are evenly dispersed within this polymer matrix once the polymer composite is allowed to cool. The thermal stability of the synthesised PES/BHF polymer composite was measured using Thermogravimetric Analysis – TGA (Mettler Toledo). This was done by heating the PES/BHF samples from 25 °C to 600 °C at 10 °C min^{-1} in air with gas flow of 100 ml/min. The TGA analysis in **Figure 40** shows the thermal degradation of synthesised PES/BHF polymer composites for varying barium hexaferrite nanoparticle concentrations of 10 mg/ml, 30 mg/ml and 60 mg/ml. The TGA curves for the three concentrations of the PES/BHF polymer composites starts decomposing between 200 °C and 330 °C with approximately 20% weight loss. Subsequently, a second decomposing step was between 320 °C and 420 °C with a weight loss of around 75% for 60 mg/ml and

approximately 85% for 30 mg/ml and 10 mg/ml. A third decomposition step can be identified between 400 °C and 480 °C with a total weight loss of 95.50% for 60 mg/ml, 98.62% for 30 mg/ml and 99.08% for 10 mg/ml. Therefore, a 60 mg/ml concentrated PES/BHF polymer composite is made up of approximately 4.50 wt% BHF nanoparticles, a 30 mg/ml PES/BHF composite contains 1.38 wt% BHF nanoparticles, and a 10 mg/ml PES/BHF composite contains 0.92 wt% BHF nanoparticles by weight. These results also confirm that a polymerisation temperature higher than 200 °C is unsuitable for this reaction as it may lead to the decomposition of the polyester chains, decreasing the molecular weight by the thermal degradation process. Thermal analysis of the polymer composites confirms the incorporation of BHF nanoparticles in the PES polymer matrix as constant mass is obtained after prolonged heating at a temperature of 600 °C, indicating the presence of BHF nanoparticles after complete polymer degradation. The ratio of BHF to polymer matrix in a given mass and how this varies with ferrofluid concentration was identified. Subsequently, magnetic properties of the PES/BHF product were measured using Vibrating Sample Magnetometry – VSM (LakeShore 7400) for the isotropically dispersed nanoparticles. The VSM samples were prepared by casting different concentrations of PES/BHF polymers at 170 °C into a brass cylinder mould and allowing them to cool down to room temperature. The magnetic properties of the solid polymer composites were measured at excitation fields between -1000 kA m^{-1} and 1000 kA m^{-1}. **Figure 41** shows the hysteresis loops of the PES/BHF polymer composites with a 60 mg/ml, 30 mg/ml and 10 mg/ml concentration of BHF nanoparticles. The hysteresis loops of all three concentrations are typical of a hard ferrimagnetic material with a constant coercivity H_c = 120 kA m^{-1}. Magnetic saturation – M_s and remanence – M_r values of the three PES/BHF polymer composites vary with particle load in the polymer matrix. The saturation and remanence values of the composites increase with increasing BHF particle concentrations, with 60 mg/ml showing magnetic saturation M_s = 0.93 Am^2 kg^{-1} and magnetic remanence M_r = 0.45 Am^2 kg^{-1}. On the other hand, 30 mg/ml concentrated PES/BHF polymer showed M_r = 0.48 Am^2 kg^{-1} and M_r = 0.24 Am^2 kg^{-1}, while 10 mg/ml PES/BHF polymer showed M_s = 0.32 Am^2 kg^{-1} and M_r = 0.16 Am^2 kg^{-1}. The weight specific remanence and magnetic saturation values are lower than pure powdered BHF nanoparticles which have reported values of up to 10.4 $mA.m^2.g^{-1}$ for remanence and 32.8 $mA.m^2.g^{-1}$ for saturation. This is mainly reflective of the relatively low nanoparticle to

polymer ratio in the PES/BHF composite as shown by the TGA results. However, the M_r/M_s ratios and H_c is the same for all three samples, indicating the absence of a magnetic interaction between the BHF nanoparticles in the PES/BHF composites[170].

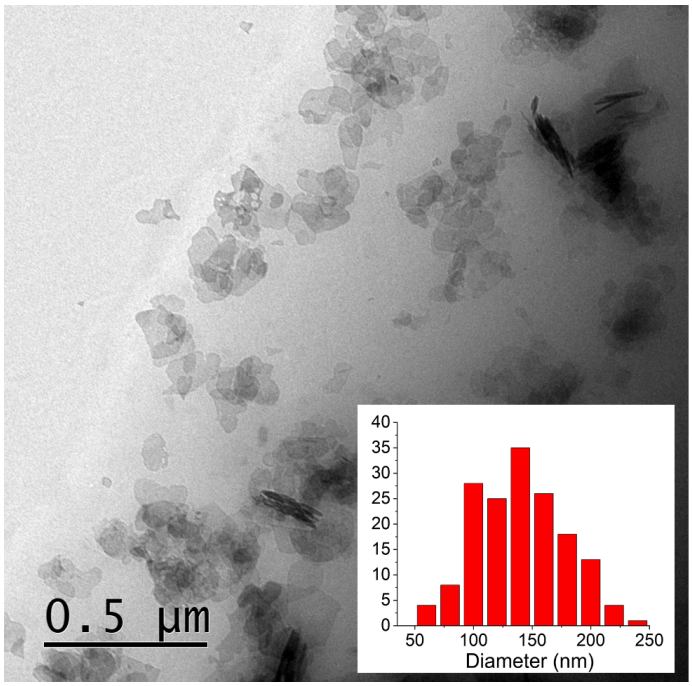

Figure 42: TEM image of isotropically dispersed BHF magnetic nanoparticles embedded in a PES polymer matrix with MNP size distribution (inset).

The synthesised PES/BHF composite was microscopically analysed using transmission electron spectroscopy (TEM). The composite was heated to 170 °C and casted into a cylinder mould upon cooling to room temperature. The casted polymer cylinders were sectioned by ultramicrotomy to 70-200 nm thickness wedged slices and cooled on water droplets which enabled to overcome compression during sectioning as well as improved adhesion to a carbon copper TEM grid support. **Figure 42** shows the TEM results for the 60 mg/ml polymerised ferrofluid. The TEM shows BHF nanoparticles embedded throughout the transparent PES polymer matrix with most of the BHF nanoparticles laying flat as opposed to perpendicular to the TEM grid. However, the BHF nanoparticles are prone to aggregation due to the strong magnetic dipole – dipole interactions between the BHF nanoparticles[109]. On the other hand, the TEM scan also shows signs of aggregated BHF nanoparticles, which could have occurred during the sliced sample preparation for which reason a size distribution was determined for the pure ethylene glycol batch in the **Figure 41** inset. In order to determine particle concentration and identify if the BHF nanoparticles are dispersed homogenously within the matrix, the density of sliced cylindrically – casted

PES/BHF samples was measured across the cylinder length. The density of pure PES polymer was measured as 1.26 g/cm^3, and increased to a density of 1.38 g/cm^3 with a standard deviation of 0.03 for PES/BH[184]. The density of the pure polymer increases by 0.12 g/cm^3 as the embedded BHF nanoparticles are introduced. Based on the characterised and optimised PES/BHF, future work will identify biodegradable properties which coupled with the controlled magnetic properties may prove beneficial in many fields such as drug delivery, tissue engineering, and functional shielding materials. On the other hand, further improvements with respect to composite filler content are expected up to 50 wt%.

6.4. Conclusion

A new polyethylene succinate (PES) hard magnetic polymer matrix composite (PMC) was developed with a high filler content of up to 4.5 wt% embedded with barium hexaferrite (BHF) magnetic nanoparticles, representing a significant increase compared to previous reports on barium hexaferrite-based polymer composites. This report thoroughly discusses a catalyst-free polycondensation reaction between ethylene glycol and succinic acid, along with the optimisation of synthesis time and temperature. These optimisations ensure a complete and successful polycondensation reaction between the monomers, producing a PES polymer matrix with robust mechanical and thermal properties. Fourier Transform Infrared (FTIR) spectroscopy, Nuclear Magnetic Resonance (NMR) spectroscopy, Gel Permeation Chromatography (GPC), and surface hardness measurements were used to chemically and mechanically characterize the pure PES polymer matrix. This was followed by the polymerisation of a CTAB-stabilised, ethylene glycol-based ferrofluid with dispersed barium hexaferrite magnetic nanoparticles. The ferrofluid was polymerised using the same catalyst-free polycondensation reaction, producing a magnetic polymer composite with homogeneously embedded isotropic barium hexaferrite nanoparticles throughout the PES matrix. The PMC was magnetically characterised using a Vibrating-Sample Magnetometer (VSM) to observe a hysteresis loop indicative of the hard magnetic properties of BHF nanoparticles, confirming the fully dispersed synthesis of a PMC with hard magnetic properties and potential biodegradability due to the PES matrix. The PMC's high filler content and thermal stability were confirmed via Thermogravimetric Analysis (TGA), while

density measurements indicated the distribution of magnetic nanoparticles. Transmission Electron Microscopy (TEM) was used to observe the BHF magnetic nanoparticles embedded within the PES polymer matrix and to assess any aggregation that may have resulted from magnetic particle interactions. Although our density measurements indicate reasonably homogeneous dispersion of BHF nanoparticles in the PES matrix, advanced methods to determine stability with greater accuracy are needed. Future work will examine the dispersion stability of higher ferrofluid concentrations and the rheological properties at high temperatures of PES/BHF samples with higher filler content. Additionally, three-dimensional (3D) manufacturing of magnetic structures will be pursued.

Chapter 7: Conclusions and Future Work

The presented research is primarily focused on Barium Hexaferrite (BHF) particles which have attracted significant attention due to their high magnetocrystalline anisotropy, large coercivity and chemical stability. Structurally BHF particles crystallise in the hexagonal magnetoplumbite structure, where magnetic moments of Fe^{3+} are distributed across inequivalent lattice sites, giving rise to its ferrimagnetic ordering. The high anisotropy field makes BHF particularly suitable for permanent magnetic applications, such as high – frequency devices and microwave absorption technologies. At the nanoscale, BHF particles display size – dependent magnetic properties, where a change in particle size can influence coercivity, magnetic saturation, and thermal stability. In addition to exploring the magnetic and structural properties of dry BHF particles, the dispersion of BHF in solvent to produce a ferrofluid material and in a polymer matrix to produce a polymer composite was also investigated.

7.1. Barium hexaferrite magnetic nanoparticles

At the initial stage of the research, it is crucial to understand the growth mechanism of BHF particles using experimental findings as well as previously reported literature. The growth mechanism includes the precipitation, nucleation and enhanced growth of the particles which ultimately affect the particle size, size distribution and morphology. Chapter 4 presents the results for the growth mechanism of hydrothermally synthesised BHF particles

at various temperatures followed by magnetic and optical characterisation. Hydrothermal synthesis offers significant advantages for the synthesis of magnetic particles including a control of particle size producing a narrow size distribution. In addition, the flexible BHF magnetoplumbite structure allows for the substitution of Fe^{3+} ions for large lanthanide cations in its lattice structure as a means to control particle size, expanding the depth of potential magnetic applications. The results presented in chapter 4 are essential for identifying the optimal hydrothermal reaction conditions for BHF particles as well as highlighting the relationship between particle size distribution and colloidal stability when dispersed in a solvent. Charged surfactants can also be utilised as stabilising agents when adsorbed onto the particle surface and provide electrostatic and steric repulsion between the particles for colloidal stability. Long – chain polymers such as dextran have been explored for the stabilisation of BHF in solvent, however, only a low loading of the particles in solvent was obtained with limited colloidal stability. In comparison, previous studies prove Dodecylbenzenesulfonic acid (DBSA) as a highly effective surfactant for dispersing hydrothermally synthesised BHF particles in 1-butanol, enabling the preparation of a stable and highly concentrated ferrofluid. DBSA - coated BHF nanoparticles exhibited long-term colloidal stability at concentrations up to 200 mg/ml, demonstrating the suitability of this surfactant for achieving dense suspensions. However, as 1-butanol is a highly volatile solvent and has limited miscibility in water, it presents significant limitations for many applications, thereby constraining the broader applicability of this system.

7.2. Barium hexaferrite dispersed in ethylene glycol

Having identified this gap in literature, this work aims was to develop a novel BHF ferrofluid stabilised in a non – volatile solvent with long – term colloidal stability. Chapter 5 presents my experimental findings on the stabilisation of BHF in ethylene glycol solvent using hexadecyltrimethylammonium bromide (CTAB) as a surfactant. Using my findings from chapter 4, dry CTAB – coated BHF particles were hydrothermally synthesised and characterised using magnetic, thermal and chemical analytical techniques. It was found that both CTAB - coated BHF in ethylene glycol and DBSA - coated BHF in 1-butanol produce ferrofluids that are stable for a sufficiently long period of time. However, the applicability of

both ferrofluids can be compared with regards to their carrier fluid. In essence, ethylene glycol as a solvent is much more useful than 1-butanol due to its high boiling point and miscibility in water which ensures the potential for a variety of applications for BHF ferrofluids. For future work, it is essential to investigate the rheological properties of the ethylene glycol–based ferrofluid, including its flow behaviour, viscosity, and shear response. Furthermore, the practical applications of BHF dispersed in ethylene glycol remain largely unexplored, and systematic evaluation will be necessary to fully assess the potential of this system within the broader field of magnetic liquids.

7.3. Barium hexaferrite dispersed within a polymer matrix composite.

The second part of my thesis involves an in – situ, catalyst – free polymerisation of CTAB – coated BHF particles stabilised in ethylene glycol. In chapter 6 presents a new polyethylene succinate (PES) polymer matrix composite (PMC) with hard magnetic properties. BHF particles were homogenously embedded in the PMC with an isotropic arrangement. The BHF/PES composite was characterised using magnetic, thermal and chemical analytical techniques. Previous studies utilising in – situ polymerisation with BHF particles reports a maximum filler content of 0.27 wt% in Poly(methyl methacrylate) PMMA. Thermal characterisation of BHF/PES composite confirmed a high filler content of up to 4.5 wt%, while magnetic measurements produced a hysteresis loop indicative of the hard magnetic properties of BHF particles. The homogenous dispersion of BHF within the PES polymer matrix was observed using optical analysis and density measurements. The combination of the magnetic properties of BHF particles with the biodegradability of the PES polymer in the developed BHF/PES composite opens promising avenues for environmentally friendly magnetic materials, with potential applications in biomedical devices, targeted delivery systems, and sustainable magnetic separation technologies. For future work, the anisotropic magnetic alignment of BHF within the PES polymer matrix would be interesting to explore and compare with the current isotropic alignment. Although the potential applications described above for BHF/PES are possible, experimental work has not been conducted to investigate this. In addition, obtaining a higher filler content of the magnetic particles in the polymer matrix would be intriguing, especially for certain possible applications.

Appendix – Supplementary Information

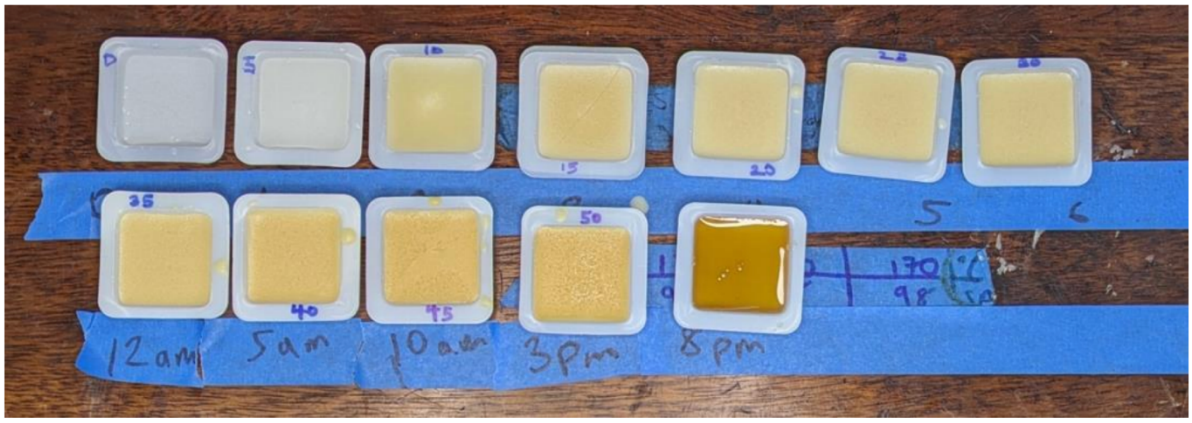

Supplementary Information 1: Picture of yellow/brown, waxy PES polymer from the transparent reactants over 60 hours.

References

(1) O'Handley, R. C. *Modern Magnetic Materials: Principles and Applications*; Wiley: New York, 2000.
(2) Coey, J. M. D. *Magnetism and Magnetic Materials*, 1st ed.; Cambridge University Press, 2001. https://doi.org/10.1017/CBO9780511845000.
(3) Chang, I. T. H.; Ren, Z. Simple Processing Method and Characterisation of Nanosized Metal Powders. *Mater. Sci. Eng. A* **2004**, *375–377*, 66–71. https://doi.org/10.1016/j.msea.2003.10.005.
(4) Rasaili, P.; Sharma, N. K.; Bhattarai, A. Comparison of Ferromagnetic Materials: Past Work, Recent Trends, and Applications. *Condens. Matter* **2022**, *7* (1), 12. https://doi.org/10.3390/condmat7010012.
(5) Goldman, A. *Handbook of Modern Ferromagnetic Materials*; Springer US: Boston, MA, 1999. https://doi.org/10.1007/978-1-4615-4917-8.
(6) Buschow, K. H. J.; De Boer, F. R. *Physics of Magnetism and Magnetic Materials*; Springer US: Boston, MA, 2003. https://doi.org/10.1007/b100503.
(7) Cullity, B. D.; Graham, C. D. *Introduction to Magnetic Materials*, 1st ed.; Wiley, 2008. https://doi.org/10.1002/9780470386323.
(8) Aharoni, A. *Introduction to the Theory of Ferromagnetism*, 2nd ed.; Oxford science publications; Oxford University Press: Oxford ; New York, 2000.
(9) Guimarães, A. P. *Principles of Nanomagnetism*; NanoScience and Technology; Springer Berlin Heidelberg: Berlin, Heidelberg, 2009. https://doi.org/10.1007/978-3-642-01482-6.
(10) Kwon, H.; Yang, Y.; Kim, G.; Gim, D.; Ha, M. Anisotropy in Magnetic Materials for Sensors and Actuators in Soft Robotic Systems. *Nanoscale* **2024**, *16* (14), 6778–6819. https://doi.org/10.1039/D3NR05737B.
(11) Meiklejohn, W. H. Exchange Anisotropy—A Review. *J. Appl. Phys.* **1962**, *33* (3), 1328–1335. https://doi.org/10.1063/1.1728716.

(12) Issa, B.; Obaidat, I.; Albiss, B.; Haik, Y. Magnetic Nanoparticles: Surface Effects and Properties Related to Biomedicine Applications. *Int. J. Mol. Sci.* **2013**, *14* (11), 21266–21305. https://doi.org/10.3390/ijms141121266.
(13) Kumar, A.; Fähler, S.; Schlörb, H.; Leistner, K.; Schultz, L. Competition between Shape Anisotropy and Magnetoelastic Anisotropy in Ni Nanowires Electrodeposited within Alumina Templates. *Phys. Rev. B* **2006**, *73* (6), 064421. https://doi.org/10.1103/PhysRevB.73.064421.
(14) Ma, Z.; Mohapatra, J.; Wei, K.; Liu, J. P.; Sun, S. Magnetic Nanoparticles: Synthesis, Anisotropy, and Applications. *Chem. Rev.* **2023**, *123* (7), 3904–3943. https://doi.org/10.1021/acs.chemrev.1c00860.
(15) *Fundamentals and Industrial Applications of Magnetic Nanoparticles*; Elsevier, 2022. https://doi.org/10.1016/C2019-0-05416-7.
(16) Patsula, V.; Moskvin, M.; Dutz, S.; Horák, D. Size-Dependent Magnetic Properties of Iron Oxide Nanoparticles. *J. Phys. Chem. Solids* **2016**, *88*, 24–30. https://doi.org/10.1016/j.jpcs.2015.09.008.
(17) *Magnetic Nanoparticles*, 1st ed.; Gubin, S. P., Ed.; Wiley, 2009. https://doi.org/10.1002/9783527627561.
(18) F. Hasany, S.; Ahmed, I.; J, R.; Rehman, A. Systematic Review of the Preparation Techniques of Iron Oxide Magnetic Nanoparticles. *Nanosci. Nanotechnol.* **2013**, *2* (6), 148–158. https://doi.org/10.5923/j.nn.20120206.01.
(19) Zeng, H.; Rice, P. M.; Wang, S. X.; Sun, S. Shape-Controlled Synthesis and Shape-Induced Texture of $MnFe_2O_4$ Nanoparticles. *J. Am. Chem. Soc.* **2004**, *126* (37), 11458–11459. https://doi.org/10.1021/ja045911d.
(20) Ding, T.; Song, K.; Clays, K.; Tung, C. Fabrication of 3D Photonic Crystals of Ellipsoids: Convective Self-Assembly in Magnetic Field. *Adv. Mater.* **2009**, *21* (19), 1936–1940. https://doi.org/10.1002/adma.200803564.
(21) Lisjak, D.; Mertelj, A. Anisotropic Magnetic Nanoparticles: A Review of Their Properties, Syntheses and Potential Applications. *Prog. Mater. Sci.* **2018**, *95*, 286–328. https://doi.org/10.1016/j.pmatsci.2018.03.003.
(22) Cordente, N.; Respaud, M.; Senocq, F.; Casanove, M.-J.; Amiens, C.; Chaudret, B. Synthesis and Magnetic Properties of Nickel Nanorods. *Nano Lett.* **2001**, *1* (10), 565–568. https://doi.org/10.1021/nl0100522.
(23) Roca, A. G.; Costo, R.; Rebolledo, A. F.; Veintemillas-Verdaguer, S.; Tartaj, P.; González-Carreño, T.; Morales, M. P.; Serna, C. J. Progress in the Preparation of Magnetic Nanoparticles for Applications in Biomedicine. *J. Phys. Appl. Phys.* **2009**, *42* (22), 224002. https://doi.org/10.1088/0022-3727/42/22/224002.
(24) Tartaj, P.; Morales, M. A. D. P.; Veintemillas-Verdaguer, S.; Gonz lez-Carre O, T.; Serna, C. J. The Preparation of Magnetic Nanoparticles for Applications in Biomedicine. *J. Phys. Appl. Phys.* **2003**, *36* (13), R182–R197. https://doi.org/10.1088/0022-3727/36/13/202.
(25) Song, Q.; Zhang, Z. J. Shape Control and Associated Magnetic Properties of Spinel Cobalt Ferrite Nanocrystals. *J. Am. Chem. Soc.* **2004**, *126* (19), 6164–6168. https://doi.org/10.1021/ja049931r.
(26) Salazar-Alvarez, G.; Qin, J.; Šepelák, V.; Bergmann, I.; Vasilakaki, M.; Trohidou, K. N.; Ardisson, J. D.; Macedo, W. A. A.; Mikhaylova, M.; Muhammed, M.; Baró, M. D.; Nogués, J. Cubic versus Spherical Magnetic Nanoparticles: The Role of Surface Anisotropy. *J. Am. Chem. Soc.* **2008**, *130* (40), 13234–13239. https://doi.org/10.1021/ja0768744.

(27) Kolhatkar, A.; Jamison, A.; Litvinov, D.; Willson, R.; Lee, T. Tuning the Magnetic Properties of Nanoparticles. *Int. J. Mol. Sci.* **2013**, *14* (8), 15977–16009. https://doi.org/10.3390/ijms140815977.
(28) Kovalenko, M. V.; Manna, L.; Cabot, A.; Hens, Z.; Talapin, D. V.; Kagan, C. R.; Klimov, V. I.; Rogach, A. L.; Reiss, P.; Milliron, D. J.; Guyot-Sionnnest, P.; Konstantatos, G.; Parak, W. J.; Hyeon, T.; Korgel, B. A.; Murray, C. B.; Heiss, W. Prospects of Nanoscience with Nanocrystals. *ACS Nano* **2015**, *9* (2), 1012–1057. https://doi.org/10.1021/nn506223h.
(29) Simeonidis, K.; Morales, M. P.; Marciello, M.; Angelakeris, M.; De La Presa, P.; Lazaro-Carrillo, A.; Tabero, A.; Villanueva, A.; Chubykalo-Fesenko, O.; Serantes, D. In-Situ Particles Reorientation during Magnetic Hyperthermia Application: Shape Matters Twice. *Sci. Rep.* **2016**, *6* (1), 38382. https://doi.org/10.1038/srep38382.
(30) Avolio, M.; Gavilán, H.; Mazario, E.; Brero, F.; Arosio, P.; Lascialfari, A.; Puerto Morales, M. Elongated Magnetic Nanoparticles with High-Aspect Ratio: A Nuclear Relaxation and Specific Absorption Rate Investigation. *Phys. Chem. Chem. Phys.* **2019**, *21* (34), 18741–18752. https://doi.org/10.1039/C9CP03441B.
(31) Schlörb, H.; Haehnel, V.; Khatri, M. S.; Srivastav, A.; Kumar, A.; Schultz, L.; Fähler, S. Magnetic Nanowires by Electrodeposition within Templates. *Phys. Status Solidi B* **2010**, *247* (10), 2364–2379. https://doi.org/10.1002/pssb.201046189.
(32) Puntes, V. F.; Zanchet, D.; Erdonmez, C. K.; Alivisatos, A. P. Synthesis of Hcp-Co Nanodisks. *J. Am. Chem. Soc.* **2002**, *124* (43), 12874–12880. https://doi.org/10.1021/ja027262g.
(33) Yang, Y.; Li, M.; Wu, Y.; Wang, T.; Choo, E. S. G.; Ding, J.; Zong, B.; Yang, Z.; Xue, J. Nanoscaled Self-Alignment of Fe_3O_4 Nanodiscs in Ultrathin rGO Films with Engineered Conductivity for Electromagnetic Interference Shielding. *Nanoscale* **2016**, *8* (35), 15989–15998. https://doi.org/10.1039/C6NR04539A.
(34) Malik, V.; Petukhov, A. V.; He, L.; Yin, Y.; Schmidt, M. Colloidal Crystallization and Structural Changes in Suspensions of Silica/Magnetite Core–Shell Nanoparticles. *Langmuir* **2012**, *28* (41), 14777–14783. https://doi.org/10.1021/la301942t.
(35) Pullar, R. C. Hexagonal Ferrites: A Review of the Synthesis, Properties and Applications of Hexaferrite Ceramics. *Prog. Mater. Sci.* **2012**, *57* (7), 1191–1334. https://doi.org/10.1016/j.pmatsci.2012.04.001.
(36) Hu, J.; Gorsak, T.; Martín Rodríguez, E.; Calle, D.; Muñoz-Ortiz, T.; Jaque, D.; Fernández, N.; Cussó, L.; Rivero, F.; Aguilar Torres, R.; García Solé, J.; Mertelj, A.; Makovec, D.; Desco, M.; Lisjak, D.; Alfonso, F.; Sanz-Rodríguez, F.; Ortgies, D. H. Magnetic Nanoplatelets for High Contrast Cardiovascular Imaging by Magnetically Modulated Optical Coherence Tomography. *ChemPhotoChem* **2019**, *3* (7), 529–539. https://doi.org/10.1002/cptc.201900071.
(37) Jean, M.; Nachbaur, V.; Bran, J.; Le Breton, J.-M. Synthesis and Characterization of SrFe12O19 Powder Obtained by Hydrothermal Process. *J. Alloys Compd.* **2010**, *496* (1–2), 306–312. https://doi.org/10.1016/j.jallcom.2010.02.002.
(38) Jamshaid, M.; Nazir, M. A.; Najam, T.; Shah, S. S. A.; Khan, H. M.; Rehman, A. U. Facile Synthesis of Yb3+-Zn2+ Substituted M Type Hexaferrites: Structural, Electric and Photocatalytic Properties under Visible Light for Methylene Blue Removal. *Chem. Phys. Lett.* **2022**, *805*, 139939. https://doi.org/10.1016/j.cplett.2022.139939.
(39) Zhang, T.; Peng, X.; Li, J.; Yang, Y.; Xu, J.; Wang, P.; Jin, D.; Jin, H.; Hong, B.; Wang, X.; Ge, H. Platelet-like Hexagonal SrFe12O19 Particles: Hydrothermal Synthesis and Their

Orientation in a Magnetic Field. *J. Magn. Magn. Mater.* **2016**, *412*, 102–106. https://doi.org/10.1016/j.jmmm.2016.03.080.
(40) Martirosyan, K. S.; Galstyan, E.; Hossain, S. M.; Wang, Y.-J.; Litvinov, D. Barium Hexaferrite Nanoparticles: Synthesis and Magnetic Properties. *Mater. Sci. Eng. B* **2011**, *176* (1), 8–13. https://doi.org/10.1016/j.mseb.2010.08.005.
(41) Lisjak, D.; Drofenik, M. Chemical Substitution—An Alternative Strategy for Controlling the Particle Size of Barium Ferrite. *Cryst. Growth Des.* **2012**, *12* (11), 5174–5179. https://doi.org/10.1021/cg301227r.
(42) Bierlich, S.; Gellersen, F.; Jacob, A.; Töpfer, J. Low-Temperature Sintering and Magnetic Properties of Sc- and In-Substituted M-Type Hexagonal Barium Ferrites for Microwave Applications. *Mater. Res. Bull.* **2017**, *86*, 19–23. https://doi.org/10.1016/j.materresbull.2016.09.025.
(43) Makovec, D.; Komelj, M.; Dražić, G.; Belec, B.; Goršak, T.; Gyergyek, S.; Lisjak, D. Incorporation of Sc into the Structure of Barium-Hexaferrite Nanoplatelets and Its Extraordinary Finite-Size Effect on the Magnetic Properties. *Acta Mater.* **2019**, *172*, 84–91. https://doi.org/10.1016/j.actamat.2019.04.050.
(44) Roca, A. G.; Gutiérrez, L.; Gavilán, H.; Fortes Brollo, M. E.; Veintemillas-Verdaguer, S.; Morales, M. D. P. Design Strategies for Shape-Controlled Magnetic Iron Oxide Nanoparticles. *Adv. Drug Deliv. Rev.* **2019**, *138*, 68–104. https://doi.org/10.1016/j.addr.2018.12.008.
(45) Cursaru, L. M.; Piticescu, R. M.; Dragut, D. V.; Morel, R.; Thébault, C.; Carrière, M.; Joisten, H.; Dieny, B. One-Step Soft Chemical Synthesis of Magnetite Nanoparticles under Inert Gas Atmosphere. Magnetic Properties and In Vitro Study. *Nanomaterials* **2020**, *10* (8), 1500. https://doi.org/10.3390/nano10081500.
(46) Maaz, K.; Karim, S.; Mumtaz, A.; Hasanain, S. K.; Liu, J.; Duan, J. L. Synthesis and Magnetic Characterization of Nickel Ferrite Nanoparticles Prepared by Co-Precipitation Route. *J. Magn. Magn. Mater.* **2009**, *321* (12), 1838–1842. https://doi.org/10.1016/j.jmmm.2008.11.098.
(47) Mee, C. D.; Jeschke, J. C. Single-Domain Properties in Hexagonal Ferrites. *J. Appl. Phys.* **1963**, *34* (4), 1271–1272. https://doi.org/10.1063/1.1729467.
(48) Lisjak, D.; Drofenik, M. The Mechanism of the Low-Temperature Formation of Barium Hexaferrite. *J. Eur. Ceram. Soc.* **2007**, *27* (16), 4515–4520. https://doi.org/10.1016/j.jeurceramsoc.2007.02.202.
(49) Lisjak, D.; Drofenik, M. The Formation of Barium Hexaferrites Using Coprecipitation Methods. In *INTERMAG Asia 2005. Digests of the IEEE International Magnetics Conference, 2005.*; IEEE: Nagoya, 2005; pp 1927–1928. https://doi.org/10.1109/INTMAG.2005.1464398.
(50) Daoush, W. M. Co-Precipitation and Magnetic Properties of Magnetite Nanoparticles for Potential Biomedical Applications. *J. Nanomedicine Res.* **2017**. https://doi.org/10.15406/jnmr.2017.05.00118.
(51) Lisjak, D.; Drofenik, M. The Influence of the Coprecipitation Conditions on the Low-Temperature Formation of Barium Hexaferrite. *J. Mater. Sci.* **2007**, *42* (20), 8606–8612. https://doi.org/10.1007/s10853-007-1850-0.
(52) Ansari, S. A. M. K.; Ficiarà, E.; Ruffinatti, F. A.; Stura, I.; Argenziano, M.; Abollino, O.; Cavalli, R.; Guiot, C.; D'Agata, F. Magnetic Iron Oxide Nanoparticles: Synthesis, Characterization and Functionalization for Biomedical Applications in the Central Nervous System. *Materials* **2019**, *12* (3), 465. https://doi.org/10.3390/ma12030465.

(53) Dudchenko, N.; Pawar, S.; Perelshtein, I.; Fixler, D. Magnetite Nanoparticles: Synthesis and Applications in Optics and Nanophotonics. *Materials* **2022**, *15* (7), 2601. https://doi.org/10.3390/ma15072601.
(54) Pullar, R. C.; Taylor, M. D.; Bhattacharya, A. K. [No Title Found]. *J. Mater. Sci.* **1997**, *32* (2), 349–352. https://doi.org/10.1023/A:1018593014378.
(55) Pullar, R. C.; Appleton, S. G.; Bhattacharya, A. K. The Manufacture, Characterisation and Microwave Properties of Aligned M Ferrite Fibres. *J. Magn. Magn. Mater.* **1998**, *186* (3), 326–332. https://doi.org/10.1016/S0304-8853(98)00107-3.
(56) Pullar, R. C.; Taylor, M. D.; Bhattacharya, A. K. [No Title Found]. *J. Mater. Sci.* **1997**, *32* (2), 365–368. https://doi.org/10.1023/A:1018549232125.
(57) Sürig, C.; Bonnenberg, D.; Hempel, K. A.; Karduck, P.; Klaar, Hj.; Sauer, Ch. Effects of Variations in Stoichiometry on M-Type Hexaferrites. *J. Phys. IV* **1997**, *07* (C1), C1-315-C1-316. https://doi.org/10.1051/jp4:19971124.
(58) Sürig, C.; Hempel, K. A.; Sauer, Ch. Influence of Stoichiometry on Hexaferrite Structure. *J. Magn. Magn. Mater.* **1996**, *157–158*, 268–269. https://doi.org/10.1016/0304-8853(95)01201-X.
(59) Zhong, W.; Ding, W.; Jiang, Y.; Zhang, N.; Zhang, J.; Du, Y.; Yan, Q. Preparation and Magnetic Properties of Barium Hexaferrite Nanoparticles Produced by the Citrate Process. *J. Am. Ceram. Soc.* **1997**, *80* (12), 3258–3262. https://doi.org/10.1111/j.1151-2916.1997.tb03264.x.
(60) Andrade, A. L.; Souza, D. M.; Pereira, M. C.; Fabris, J. D.; Domingues, R. Z. Synthesis and Characterization of Magnetic Nanoparticles Coated with Silica through a Sol-Gel Approach. *Cerâmica* **2009**, *55* (336), 420–424. https://doi.org/10.1590/S0366-69132009000400013.
(61) Torres-Gómez, N.; Nava, O.; Argueta-Figueroa, L.; García-Contreras, R.; Baeza-Barrera, A.; Vilchis-Nestor, A. R. Shape Tuning of Magnetite Nanoparticles Obtained by Hydrothermal Synthesis: Effect of Temperature. *J. Nanomater.* **2019**, *2019*, 1–15. https://doi.org/10.1155/2019/7921273.
(62) Byrappa, K. *Handbook of Hydrothermal Technology*, 2nd ed.; Materials Science and Process Technology; William Andrew: Oxford, 2013.
(63) Rafie, S. F.; Sayahi, H.; Abdollahi, H.; Abu-Zahra, N. Hydrothermal Synthesis of Fe3O4 Nanoparticles at Different pHs and Its Effect on Discoloration of Methylene Blue: Evaluation of Alternatives by TOPSIS Method. *Mater. Today Commun.* **2023**, *37*, 107589. https://doi.org/10.1016/j.mtcomm.2023.107589.
(64) Ge, S.; Shi, X.; Sun, K.; Li, C.; Uher, C.; Baker, J. R.; Banaszak Holl, M. M.; Orr, B. G. Facile Hydrothermal Synthesis of Iron Oxide Nanoparticles with Tunable Magnetic Properties. *J. Phys. Chem. C* **2009**, *113* (31), 13593–13599. https://doi.org/10.1021/jp902953t.
(65) Ali, A.; Shah, T.; Ullah, R.; Zhou, P.; Guo, M.; Ovais, M.; Tan, Z.; Rui, Y. Review on Recent Progress in Magnetic Nanoparticles: Synthesis, Characterization, and Diverse Applications. *Front. Chem.* **2021**, *9*, 629054. https://doi.org/10.3389/fchem.2021.629054.
(66) Lee, J.-H.; Byeon, T.-B.; Lee, H.-J.; Kim, C.-G.; Kim, T.-O. Preparation of Single Crystallites of Barium Ferrite by Hydrothermal Synthesis. *J. Phys. IV* **1997**, *07* (C1), C1-751-C1-752. https://doi.org/10.1051/jp4:19971307.

(67) Liu, X.; Wang, J.; Gan, L.-M.; Ng, S.-C. Improving the Magnetic Properties of Hydrothermally Synthesized Barium Ferrite. *J. Magn. Magn. Mater.* **1999**, *195* (2), 452–459. https://doi.org/10.1016/S0304-8853(99)00123-7.
(68) Satyanarayana, T. A Review on Chemical and Physical Synthesis Methods of Nanomaterials. *Int. J. Res. Appl. Sci. Eng. Technol.* **2018**, *6* (1), 2885–2889. https://doi.org/10.22214/ijraset.2018.1396.
(69) Szczyglewska, P.; Feliczak-Guzik, A.; Nowak, I. Nanotechnology–General Aspects: A Chemical Reduction Approach to the Synthesis of Nanoparticles. *Molecules* **2023**, *28* (13), 4932. https://doi.org/10.3390/molecules28134932.
(70) Reverberi, A. P.; Kuznetsov, N. T.; Meshalkin, V. P.; Salerno, M.; Fabiano, B. Systematical Analysis of Chemical Methods in Metal Nanoparticles Synthesis. *Theor. Found. Chem. Eng.* **2016**, *50* (1), 59–66. https://doi.org/10.1134/S0040579516010127.
(71) Bisht, N.; Phalswal, P.; Khanna, P. K. Selenium Nanoparticles: A Review on Synthesis and Biomedical Applications. *Mater. Adv.* **2022**, *3* (3), 1415–1431. https://doi.org/10.1039/D1MA00639H.
(72) Sharma, G.; Kumar, A.; Sharma, S.; Naushad, Mu.; Prakash Dwivedi, R.; ALOthman, Z. A.; Mola, G. T. Novel Development of Nanoparticles to Bimetallic Nanoparticles and Their Composites: A Review. *J. King Saud Univ. - Sci.* **2019**, *31* (2), 257–269. https://doi.org/10.1016/j.jksus.2017.06.012.
(73) Kelgenbaeva, Z.; Murzubraimov, B.; Kozlovsky, A.; Adil Akai Tegin, R.; Turdubai Kyzy, A.; Murzabekova, E.; Aidaraliev, J.; Dyusheeva, B. Magnetic Nanoparticles Preparation by Chemical Reduction for Biomedical Applications. *EPJ Web Conf.* **2019**, *201*, 01002. https://doi.org/10.1051/epjconf/201920101002.
(74) Sun, S.; Murray, C. B.; Doyle, H. Controlled Assembly of Monodisperse ε-Cobalt-Based Nanocrystals. *MRS Proc.* **1999**, *577*, 385. https://doi.org/10.1557/PROC-577-385.
(75) Huang, J.; He, L.; Leng, Y.; Zhang, W.; Li, X.; Chen, C.; Liu, Y. One-Pot Synthesis and Magnetic Properties of Hollow Fe_{70} Co_{30} Nanospheres. *Nanotechnology* **2007**, *18* (41), 415603. https://doi.org/10.1088/0957-4484/18/41/415603.
(76) Frey, N. A.; Peng, S.; Cheng, K.; Sun, S. Magnetic Nanoparticles: Synthesis, Functionalization, and Applications in Bioimaging and Magnetic Energy Storage. *Chem. Soc. Rev.* **2009**, *38* (9), 2532. https://doi.org/10.1039/b815548h.
(77) Hao, J.; Xu, S.; Gao, B.; Pan, L. PL Tunable GaN Nanoparticles Synthesis through Femtosecond Pulsed Laser Ablation in Different Environments. *Nanomaterials* **2020**, *10* (3), 439. https://doi.org/10.3390/nano10030439.
(78) Subhan, A.; Mourad, A.-H. I.; Al-Douri, Y. Influence of Laser Process Parameters, Liquid Medium, and External Field on the Synthesis of Colloidal Metal Nanoparticles Using Pulsed Laser Ablation in Liquid: A Review. *Nanomaterials* **2022**, *12* (13), 2144. https://doi.org/10.3390/nano12132144.
(79) Dittrich, S.; Streubel, R.; McDonnell, C.; Huber, H. P.; Barcikowski, S.; Gökce, B. Comparison of the Productivity and Ablation Efficiency of Different Laser Classes for Laser Ablation of Gold in Water and Air. *Appl. Phys. A* **2019**, *125* (6), 432. https://doi.org/10.1007/s00339-019-2704-8.
(80) Patil, P. P.; Phase, D. M.; Kulkarni, S. A.; Ghaisas, S. V.; Kulkarni, S. K.; Kanetkar, S. M.; Ogale, S. B.; Bhide, V. G. Pulsed-Laser – Induced Reactive Quenching at Liquid-Solid Interface: Aqueous Oxidation of Iron. *Phys. Rev. Lett.* **1987**, *58* (3), 238–241. https://doi.org/10.1103/PhysRevLett.58.238.

(81) Kanitz, A.; Hoppius, J. S.; del Mar Sanz, M.; Maicas, M.; Ostendorf, A.; Gurevich, E. L. Synthesis of Magnetic Nanoparticles by Ultrashort Pulsed Laser Ablation of Iron in Different Liquids. *ChemPhysChem* **2017**, *18* (9), 1155–1164. https://doi.org/10.1002/cphc.201601252.
(82) Chen, G. X.; Hong, M. H.; Lan, B.; Wang, Z. B.; Lu, Y. F.; Chong, T. C. A Convenient Way to Prepare Magnetic Colloids by Direct Nd:YAG Laser Ablation. *Appl. Surf. Sci.* **2004**, *228* (1–4), 169–175. https://doi.org/10.1016/j.apsusc.2004.01.007.
(83) Franzel, L.; Bertino, M. F.; Huba, Z. J.; Carpenter, E. E. Synthesis of Magnetic Nanoparticles by Pulsed Laser Ablation. *Appl. Surf. Sci.* **2012**, *261*, 332–336. https://doi.org/10.1016/j.apsusc.2012.08.010.
(84) Jakobi, J.; Petersen, S.; Menéndez-Manjón, A.; Wagener, P.; Barcikowski, S. Magnetic Alloy Nanoparticles from Laser Ablation in Cyclopentanone and Their Embedding into a Photoresist. *Langmuir* **2010**, *26* (10), 6892–6897. https://doi.org/10.1021/la101014g.
(85) Chen, R.; Song, G.; Wei, Y. Synthesis of Variable-Sized Fe_3O_4 Nanocrystals by Visible Light Irradiation at Room Temperature. *J. Phys. Chem. C* **2010**, *114* (32), 13409–13413. https://doi.org/10.1021/jp912162g.
(86) Liu, P.; Cai, W.; Zeng, H. Fabrication and Size-Dependent Optical Properties of FeO Nanoparticles Induced by Laser Ablation in a Liquid Medium. *J. Phys. Chem. C* **2008**, *112* (9), 3261–3266. https://doi.org/10.1021/jp709714a.
(87) V. N., A.; Johny, J.; Garza-Navarro, M. A.; Shaji, S.; Thomas, S.; M. R., A. Synthesis of Surfactant Free Stable Nanofluids Based on Barium Hexaferrite by Pulsed Laser Ablation in Liquid. *RSC Adv.* **2018**, *8* (34), 19261–19271. https://doi.org/10.1039/C8RA02754D.
(88) Kustov, L.; Vikanova, K. Synthesis of Metal Nanoparticles under Microwave Irradiation: Get Much with Less Energy. *Metals* **2023**, *13* (10), 1714. https://doi.org/10.3390/met13101714.
(89) Fernández-Barahona, I.; Muñoz-Hernando, M.; Herranz, F. Microwave-Driven Synthesis of Iron-Oxide Nanoparticles for Molecular Imaging. *Molecules* **2019**, *24* (7), 1224. https://doi.org/10.3390/molecules24071224.
(90) Seol, S. K.; Kim, D.; Jung, S.; Hwu, Y. Microwave Synthesis of Gold Nanoparticles: Effect of Applied Microwave Power and Solution pH. *Mater. Chem. Phys.* **2011**, *131* (1–2), 331–335. https://doi.org/10.1016/j.matchemphys.2011.09.050.
(91) Arshi, N.; Ahmed, F.; Kumar, S.; Anwar, M. S.; Lu, J.; Koo, B. H.; Lee, C. G. Microwave Assisted Synthesis of Gold Nanoparticles and Their Antibacterial Activity against Escherichia Coli (E. Coli). *Curr. Appl. Phys.* **2011**, *11* (1), S360–S363. https://doi.org/10.1016/j.cap.2010.11.102.
(92) Ngo, V. K. T.; Nguyen, H. P. U.; Huynh, T. P.; Tran, N. N. P.; Lam, Q. V.; Huynh, T. D. Preparation of Gold Nanoparticles by Microwave Heating and Application of Spectroscopy to Study Conjugate of Gold Nanoparticles with Antibody *E. Coli* O157:H7. *Adv. Nat. Sci. Nanosci. Nanotechnol.* **2015**, *6* (3), 035015. https://doi.org/10.1088/2043-6262/6/3/035015.
(93) Pal, J.; Deb, M. K.; Deshmukh, D. K.; Sen, B. K. Microwave-Assisted Synthesis of Platinum Nanoparticles and Their Catalytic Degradation of Methyl Violet in Aqueous Solution. *Appl. Nanosci.* **2014**, *4* (1), 61–65. https://doi.org/10.1007/s13204-012-0170-0.
(94) Chikata, T.; Katoh, S. Direct Synthesis of “Fluid-Ferrite” by Microwave-Assisted Chemical Reaction. *J. Soc. Powder Technol. Jpn.* **2004**, *41* (9), 651–655. https://doi.org/10.4164/sptj.41.651.

(95) Yamauchi, T.; Tsukahara, Y.; Sakata, T.; Mori, H.; Chikata, T.; Katoh, S.; Wada, Y. Barium Ferrite Powders Prepared by Microwave-Induced Hydrothermal Reaction and Magnetic Property. *J. Magn. Magn. Mater.* **2009**, *321* (1), 8–11. https://doi.org/10.1016/j.jmmm.2008.07.005.
(96) Cowley, M. D. **Ferrohydrodynamics.** By R. E. R OSENSWEIG . Cambridge University Press, 1985. 344 Pp. £45. *J. Fluid Mech.* **1989**, *200*, 597–599. https://doi.org/10.1017/S0022112089220773.
(97) Khajehsaeid, H.; Alaghehband, N.; Bavil, P. K. On the Yield Stress of Magnetorheological Fluids. *Chem. Eng. Sci.* **2022**, *256*, 117699. https://doi.org/10.1016/j.ces.2022.117699.
(98) DLVO Theory of Colloid Stability. In *Interface Science and Technology*; Elsevier, 2024; Vol. 37, pp 217–244. https://doi.org/10.1016/B978-0-443-16116-2.00009-6.
(99) Liang, Y.; Hilal, N.; Langston, P.; Starov, V. Interaction Forces between Colloidal Particles in Liquid: Theory and Experiment. *Adv. Colloid Interface Sci.* **2007**, *134–135*, 151–166. https://doi.org/10.1016/j.cis.2007.04.003.
(100) Van Oss, C. J.; Giese, R. F. Role of the Properties and Structure of Liquid Water in Colloidal and Interfacial Systems. *J. Dispers. Sci. Technol.* **2005**, *25* (5), 631–655. https://doi.org/10.1081/DIS-200027316.
(101) Martínez-Pedrero, F.; Tirado-Miranda, M.; Schmitt, A.; Callejas-Fernández, J. Primary and Secondary Bonds in Field Induced Aggregation of Electric Double Layered Magnetic Particles. *Langmuir* **2009**, *25* (12), 6658–6664. https://doi.org/10.1021/la803626v.
(102) Oh, J. K.; Park, J. M. Iron Oxide-Based Superparamagnetic Polymeric Nanomaterials: Design, Preparation, and Biomedical Application. *Prog. Polym. Sci.* **2011**, *36* (1), 168–189. https://doi.org/10.1016/j.progpolymsci.2010.08.005.
(103) Tsouris, C.; Scott, T. C. Flocculation of Paramagnetic Particles in a Magnetic Field. *J. Colloid Interface Sci.* **1995**, *171* (2), 319–330. https://doi.org/10.1006/jcis.1995.1186.
(104) Goršak, T.; Makovec, D.; Javornik, U.; Belec, B.; Kralj, S.; Lisjak, D. A Functionalization Strategy for the Dispersion of Permanently Magnetic Barium-Hexaferrite Nanoplatelets in Complex Biological Media. *Colloids Surf. Physicochem. Eng. Asp.* **2019**, *573*, 119–127. https://doi.org/10.1016/j.colsurfa.2019.04.051.
(105) *Principles of Colloid and Surface Chemistry, Revised and Expanded*, 0 ed.; Hiemenz, P. C., Rajagopalan, R., Eds.; CRC Press, 2016. https://doi.org/10.1201/9781315274287.
(106) Choi, H. J.; Kwon, T. M.; Jhon, M. S. Effects of Shear Rate and Particle Concentration on Rheological Properties of Magnetic Particle Suspensions. *J. Mater. Sci.* **2000**, *35* (4), 889–894. https://doi.org/10.1023/A:1004742223080.
(107) Massart, R. Preparation of Aqueous Magnetic Liquids in Alkaline and Acidic Media. *IEEE Trans. Magn.* **1981**, *17* (2), 1247–1248. https://doi.org/10.1109/TMAG.1981.1061188.
(108) *Intermolecular and Surface Forces*; Elsevier, 2011. https://doi.org/10.1016/C2009-0-21560-1.
(109) Hribar Boštjančič, P.; Tomšič, M.; Jamnik, A.; Lisjak, D.; Mertelj, A. Electrostatic Interactions between Barium Hexaferrite Nanoplatelets in Alcohol Suspensions. *J. Phys. Chem. C* **2019**, *123* (37), 23272–23279. https://doi.org/10.1021/acs.jpcc.9b07455.
(110) Barrow, M.; Taylor, A.; Murray, P.; Rosseinsky, M. J.; Adams, D. J. Design Considerations for the Synthesis of Polymer Coated Iron Oxide Nanoparticles for Stem Cell Labelling and Tracking Using MRI. *Chem Soc Rev* **2015**, *44* (19), 6733–6748. https://doi.org/10.1039/C5CS00331H.

(111) *Nanoparticles: Synthesis, Stabilization, Passivation, and Functionalization*; Nagarajan, R., Hatton, T. A., Eds.; ACS Symposium Series; American Chemical Society: Washington, DC, 2008; Vol. 996. https://doi.org/10.1021/bk-2008-0996.
(112) Heinz, H.; Pramanik, C.; Heinz, O.; Ding, Y.; Mishra, R. K.; Marchon, D.; Flatt, R. J.; Estrela-Lopis, I.; Llop, J.; Moya, S.; Ziolo, R. F. Nanoparticle Decoration with Surfactants: Molecular Interactions, Assembly, and Applications. *Surf. Sci. Rep.* **2017**, *72* (1), 1–58. https://doi.org/10.1016/j.surfrep.2017.02.001.
(113) Pujari, S. P.; Scheres, L.; Marcelis, A. T. M.; Zuilhof, H. Covalent Surface Modification of Oxide Surfaces. *Angew. Chem. Int. Ed.* **2014**, *53* (25), 6322–6356. https://doi.org/10.1002/anie.201306709.
(114) Dias, A. M. G. C.; Hussain, A.; Marcos, A. S.; Roque, A. C. A. A Biotechnological Perspective on the Application of Iron Oxide Magnetic Colloids Modified with Polysaccharides. *Biotechnol. Adv.* **2011**, *29* (1), 142–155. https://doi.org/10.1016/j.biotechadv.2010.10.003.
(115) Wang, Y.-X. J.; Hussain, S. M.; Krestin, G. P. Superparamagnetic Iron Oxide Contrast Agents: Physicochemical Characteristics and Applications in MR Imaging. *Eur. Radiol.* **2001**, *11* (11), 2319–2331. https://doi.org/10.1007/s003300100908.
(116) *Ferrofluids: Magnetically Controllable Fluids and Their Applications*; Odenbach, S., Ed.; Beig, R., Englert, B.-G., Frisch, U., Hänggi, P., Hepp, K., Hillebrandt, W., Imboden, D., Jaffe, R. L., Lipowsky, R., V. Löhneysen, H., Ojima, I., Sornette, D., Theisen, S., Weise, W., Wess, J., Zittartz, J., Series Eds.; Lecture Notes in Physics; Springer Berlin Heidelberg: Berlin, Heidelberg, 2002; Vol. 594. https://doi.org/10.1007/3-540-45646-5.
(117) *Colloidal Magnetic Fluids: Basics, Development and Application of Ferrofluids*; Odenbach, S., Ed.; Lecture Notes in Physics; Springer Berlin Heidelberg: Berlin, Heidelberg, 2009; Vol. 763. https://doi.org/10.1007/978-3-540-85387-9.
(118) Odenbach, S. Ferrofluids—Magnetically Controlled Suspensions. *Colloids Surf. Physicochem. Eng. Asp.* **2003**, *217* (1–3), 171–178. https://doi.org/10.1016/S0927-7757(02)00573-3.
(119) Scherer, C.; Figueiredo Neto, A. M. Ferrofluids: Properties and Applications. *Braz. J. Phys.* **2005**, *35* (3a), 718–727. https://doi.org/10.1590/S0103-97332005000400018.
(120) Nagornyi, A. V.; Socoliuc, V.; Petrenko, V. I.; Almasy, L.; Ivankov, O. I.; Avdeev, M. V.; Bulavin, L. A.; Vekas, L. Structural Characterization of Concentrated Aqueous Ferrofluids. *J. Magn. Magn. Mater.* **2020**, *501*, 166445. https://doi.org/10.1016/j.jmmm.2020.166445.
(121) Sajid, M.; Kalinowska, K.; Płotka-Wasylka, J. Ferrofluids Based Analytical Extractions and Evaluation of Their Greenness. *J. Mol. Liq.* **2021**, *339*, 116901. https://doi.org/10.1016/j.molliq.2021.116901.
(122) Socoliuc, V.; Taculescu, A.; Podaru, C.; Dobra, A.; Daia, C.; Marinica, O.; Turcu, R.; Vekas, L.; Häfeli, U.; Schütt, W.; Zborowski, M. Clustering in Water Based Magnetic Nanofluids: Investigations by Light Scattering Methods; Rostock, (Germany), 2010; pp 89–95. https://doi.org/10.1063/1.3530065.
(123) Dick, S. G.; Fuerstenau, D. W.; Healy, T. W. Adsorption of Alkylbenzene Sulfonate (A.B.S.) Surfactants at the Alumina-Water Interface. *J. Colloid Interface Sci.* **1971**, *37* (3), 595–602. https://doi.org/10.1016/0021-9797(71)90337-7.
(124) Leong, Y. K.; Boger, D. V.; Scales, P. J.; Healy, T. W. Interparticle Forces Arising from Adsorbed Surfactants in Colloidal Suspensions: An Additional Attractive Force. *J. Colloid Interface Sci.* **1996**, *181* (2), 605–612. https://doi.org/10.1006/jcis.1996.0418.

(125) Panya, P.; Arquero, O.; Franks, G. V.; Wanless, E. J. Dispersion Stability of a Ceramic Glaze Achieved through Ionic Surfactant Adsorption. *J. Colloid Interface Sci.* **2004**, *279* (1), 23–35. https://doi.org/10.1016/j.jcis.2004.06.061.
(126) Ovtar, S.; Lisjak, D.; Drofenik, M. Barium Hexaferrite Suspensions for Electrophoretic Deposition. *J. Colloid Interface Sci.* **2009**, *337* (2), 456–463. https://doi.org/10.1016/j.jcis.2009.05.041.
(127) Primc, D.; Makovec, D.; Lisjak, D.; Drofenik, M. Hydrothermal Synthesis of Ultrafine Barium Hexaferrite Nanoparticles and the Preparation of Their Stable Suspensions. *Nanotechnology* **2009**, *20* (31), 315605. https://doi.org/10.1088/0957-4484/20/31/315605.
(128) Pankov, V. V.; Pernet, M.; Germi, P.; Mollard, P. Fine Hexaferrite Particles for Perpendicular Recording Prepared by the Coprecipitation Method in the Presence of an Inert Component. *J. Magn. Magn. Mater.* **1993**, *120* (1–3), 69–72. https://doi.org/10.1016/0304-8853(93)91289-J.
(129) Haneda, K.; Kojima, H. Magnetization Reversal Process in Chemically Precipitated and Ordinary Prepared BaFe12O19. *J. Appl. Phys.* **1973**, *44* (8), 3760–3762. https://doi.org/10.1063/1.1662836.
(130) Xu, P.; Han, X.; Zhao, H.; Liang, Z.; Wang, J. Effect of Stoichiometry on the Phase Formation and Magnetic Properties of BaFe12O19 Nanoparticles by Reverse Micelle Technique. *Mater. Lett.* **2008**, *62* (8–9), 1305–1308. https://doi.org/10.1016/j.matlet.2007.08.039.
(131) Müller, R.; Hiergeist, R.; Steinmetz, H.; Ayoub, N.; Fujisaki, M.; Schüppel, W. Barium Hexaferrite Ferrofluids – Preparation and Physical Properties. *J. Magn. Magn. Mater.* **1999**, *201* (1–3), 34–37. https://doi.org/10.1016/S0304-8853(99)00016-5.
(132) Müller, R.; Hiergeist, R.; Gawalek, W.; Hoell, A.; Wiedenmann, A. Magnetic and Structural Investigations on Barium Hexaferrite Ferrofluids. *J. Magn. Magn. Mater.* **2002**, *252*, 43–45. https://doi.org/10.1016/S0304-8853(02)00682-0.
(133) Duong, G. V.; Sato Turtelli, R.; Thuan, B. D.; Linh, D. V.; Hanh, N.; Groessinger, R. Magnetic Properties of Nanocrystalline BaFe12O19 Prepared by Hydrothermal Method. *J. Non-Cryst. Solids* **2007**, *353* (8–10), 811–813. https://doi.org/10.1016/j.jnoncrysol.2006.12.047.
(134) Makovec, D.; Gyergyek, S.; Goršak, T.; Belec, B.; Lisjak, D. Evolution of the Microstructure during the Early Stages of Sintering Barium Hexaferrite Nanoplatelets. *J. Eur. Ceram. Soc.* **2019**, *39* (15), 4831–4841. https://doi.org/10.1016/j.jeurceramsoc.2019.07.016.
(135) Wang, M.-L.; Shih, Z.-W.; Lin, C.-H. Reaction Mechanism of Producing Barium Hexaferrites from γ-Fe2O3 and Ba(OH)2 by Hydrothermal Method. *J. Cryst. Growth* **1991**, *114* (3), 435–445. https://doi.org/10.1016/0022-0248(91)90059-E.
(136) Drofenik, M.; Kristl, M.; Žnidaršič, A.; Hanžel, D.; Lisjak, D. Hydrothermal Synthesis of Ba-Hexaferrite Nanoparticles. *J. Am. Ceram. Soc.* **2007**, *90* (7), 2057–2061. https://doi.org/10.1111/j.1551-2916.2007.01740.x.
(137) Makovec, D.; Belec, B.; Goršak, T.; Lisjak, D.; Komelj, M.; Dražić, G.; Gyergyek, S. Discrete Evolution of the Crystal Structure during the Growth of Ba-Hexaferrite Nanoplatelets. *Nanoscale* **2018**, *10* (30), 14480–14491. https://doi.org/10.1039/C8NR03815E.
(138) Drofenik, M.; Ban, I.; Makovec, D.; Žnidaršič, A.; Jagličić, Z.; Hanžel, D.; Lisjak, D. The Hydrothermal Synthesis of Super-Paramagnetic Barium Hexaferrite Particles. *Mater.*

Chem. Phys. **2011**, *127* (3), 415–419. https://doi.org/10.1016/j.matchemphys.2011.02.037.
(139) Drofenik, M.; Ban, I.; Ferk, G.; Makovec, D.; Žnidaršič, A.; Jagličić, Z.; Lisjak, D. The Concept of a Low-Temperature Synthesis for Superparamagnetic $BaFe_{12}O_{19}$ Particles. *J. Am. Ceram. Soc.* **2010**, *93* (6), 1602–1607. https://doi.org/10.1111/j.1551-2916.2010.03620.x.
(140) Primc, D.; Drofenik, M.; Makovec, D. Low-Temperature Hydrothermal Synthesis of Ultrafine Strontium Hexaferrite Nanoparticles. *Eur. J. Inorg. Chem.* **2011**, *2011* (25), 3802–3809. https://doi.org/10.1002/ejic.201100326.
(141) Makovec, D.; Primc, D.; Šturm, S.; Kodre, A.; Hanžel, D.; Drofenik, M. Structural Properties of Ultrafine Ba-Hexaferrite Nanoparticles. *J. Solid State Chem.* **2012**, *196*, 63–71. https://doi.org/10.1016/j.jssc.2012.07.043.
(142) G. W. Rathenau, E. W. Gorter, G. W. van Oosterhout, J. J. W. Ferroxdure a Class of New Permanent Magnet Materials. *Phillips Tech. Rev* **1952**, *13* ((7)), 194–208.
(143) Dairy, A. R. A.; Al-Hmoud, L. A.; Khatatbeh, H. A. Magnetic and Structural Properties of Barium Hexaferrite Nanoparticles Doped with Titanium. *Symmetry* **2019**, *11* (6), 732. https://doi.org/10.3390/sym11060732.
(144) Manglam, M. K.; Kumari, S.; Mallick, J.; Kar, M. Crystal Structure and Magnetic Properties Study on Barium Hexaferrite of Different Average Crystallite Size. *Appl. Phys. A* **2021**, *127* (2), 138. https://doi.org/10.1007/s00339-020-04232-8.
(145) Ovtar, S.; Lisjak, D.; Drofenik, M. Preparation of Oriented Barium Hexaferrite Films by Electrophoretic Deposition: Preparation of Oriented Barium Hexaferrite Films. *J. Am. Ceram. Soc.* **2011**, *94* (10), 3373–3379. https://doi.org/10.1111/j.1551-2916.2011.04500.x.
(146) Lisjak, D.; Ovtar, S.; Kovač, J.; Gregoratti, L.; Aleman, B.; Amati, M.; Fanetti, M.; Makovec, D. A Surface-Chemistry Study of Barium Ferrite Nanoplates with DBSa-Modified Surfaces. *Appl. Surf. Sci.* **2014**, *305*, 366–374. https://doi.org/10.1016/j.apsusc.2014.03.092.
(147) Pattanayak, R.; Panigrahi, S.; Dash, T.; Muduli, R.; Behera, D. Electric Transport Properties Study of Bulk BaFe12O19 by Complex Impedance Spectroscopy. *Phys. B Condens. Matter* **2015**, *474*, 57–63. https://doi.org/10.1016/j.physb.2015.06.006.
(148) Hunter, R. *Zeta Potential in Colloid Science: Principles and Applications (Colloid Sciences Series)*., 1st ed.; Academic Press, 1989.
(149) Kim, Y.; Lim, I. J.; Lim, H.; Joo, Y.; Park, J.; Hossain, M. M.; Cho, H.; You, N.; Ahn, S.; Lee, H.; Lee, S. S.; Joo, Y.; Moon, S. Y.; Yoo, H. I.; Lum, C.; Park, C.; Choi, S. Q.; Jang, S. G. High-Density Boron Nitride Nanotube Composites via Surfactant-Stabilized Lyotropic Liquid Crystals for Enhanced Space Radiation Shielding. *Adv. Funct. Mater.* **2025**, *35* (52), e10716. https://doi.org/10.1002/adfm.202510716.
(150) Wilhoit, R. C.; Chao, J.; Hall, K. R. Thermodynamic Properties of Key Organic Oxygen Compounds in the Carbon Range C_1 to C_4. Part 1. Properties of Condensed Phases. *J. Phys. Chem. Ref. Data* **1985**, *14* (1), 1–175. https://doi.org/10.1063/1.555747.
(151) Ru-Min Wang, Shui-Rong Zheng and Ya-Ping Zheng. *Polymer Matrix Composites and Technology*; 2011.
(152) Wei, X.; Jin, M.-L.; Yang, H.; Wang, X.-X.; Long, Y.-Z.; Chen, Z. Advances in 3D Printing of Magnetic Materials: Fabrication, Properties, and Their Applications. *J. Adv. Ceram.* **2022**, *11* (5), 665–701. https://doi.org/10.1007/s40145-022-0567-5.

(153) Li, W.; Gu, H.; Liu, Z.; Zhang, H.; Jiang, L.; Zhou, X. Research Progress in the Synthesis and Application of Magnetic Self-Healing Polymer Composites. *Eur. Polym. J.* **2024**, *202*, 112633. https://doi.org/10.1016/j.eurpolymj.2023.112633.
(154) Sharma, A.; Mangla, D.; Shehnaz; Chaudhry, S. A. Recent Advances in Magnetic Composites as Adsorbents for Wastewater Remediation. *J. Environ. Manage.* **2022**, *306*, 114483. https://doi.org/10.1016/j.jenvman.2022.114483.
(155) Gil, S.; Mano, J. F. Magnetic Composite Biomaterials for Tissue Engineering. *Biomater Sci* **2014**, *2* (6), 812–818. https://doi.org/10.1039/C4BM00041B.
(156) Ramos, J.; Millán, A.; Palacio, F. Production of Magnetic Nanoparticles in a Polyvinylpyridine Matrix. *Polymer* **2000**, *41* (24), 8461–8464. https://doi.org/10.1016/S0032-3861(00)00272-X.
(157) Matthews, F. L.; Rawlings, R. D. Polymer Matrix Composites. In *Composite Materials*; Elsevier, 1999; pp 168–205. https://doi.org/10.1016/B978-1-85573-473-9.50008-4.
(158) *Composite Materials*; Elsevier, 1999. https://doi.org/10.1016/C2013-0-17714-8.
(159) Jiang, W.; Zhu, H.; Guo, C.; Li, J.; Xue, Q.; Feng, J.; Gong, X. Poly(Methyl Methacrylate)-Coated Carbonyl Iron Particles and Their Magnetorheological Characteristics: Magnetorheological Characteristics of PMMA-Coated CI Particles. *Polym. Int.* **2010**, *59* (7), 879–883. https://doi.org/10.1002/pi.2794.
(160) Guo, Z.; Henry, L. L.; Palshin, V.; Podlaha, E. J. Synthesis of Poly(Methyl Methacrylate) Stabilized Colloidal Zero-Valence Metallic Nanoparticles. *J Mater Chem* **2006**, *16* (18), 1772–1777. https://doi.org/10.1039/B515565G.
(161) Gong, T.; Yang, D.; Hu, J.; Yang, W.; Wang, C.; Lu, J. Q. Preparation of Monodispersed Hybrid Nanospheres with High Magnetite Content from Uniform Fe3O4 Clusters. *Colloids Surf. Physicochem. Eng. Asp.* **2009**, *339* (1–3), 232–239. https://doi.org/10.1016/j.colsurfa.2009.02.034.
(162) Akgöl, S.; Kaçar, Y.; Denizli, A.; Arıca, M. Y. Hydrolysis of Sucrose by Invertase Immobilized onto Novel Magnetic Polyvinylalcohol Microspheres. *Food Chem.* **2001**, *74* (3), 281–288. https://doi.org/10.1016/S0308-8146(01)00150-9.
(163) Yang, J.; Lee, T.-I.; Lee, J.; Lim, E.-K.; Hyung, W.; Lee, C.-H.; Song, Y. J.; Suh, J.-S.; Yoon, H.-G.; Huh, Y.-M.; Haam, S. Synthesis of Ultrasensitive Magnetic Resonance Contrast Agents for Cancer Imaging Using PEG-Fatty Acid. *Chem. Mater.* **2007**, *19* (16), 3870–3876. https://doi.org/10.1021/cm070495s.
(164) Banerjee, S. S.; Chen, D.-H. Magnetic Nanoparticles Grafted with Cyclodextrin for Hydrophobic Drug Delivery. *Chem. Mater.* **2007**, *19* (25), 6345–6349. https://doi.org/10.1021/cm702278u.
(165) Liu, F.; Ni, Q.-Q.; Murakami, Y. Preparation of Magnetic Polyvinyl Alcohol Composite Nanofibers with Homogenously Dispersed Nanoparticles and High Water Resistance. *Text. Res. J.* **2013**, *83* (5), 510–518. https://doi.org/10.1177/0040517512444334.
(166) Mayes, E. L.; Vollrath, F.; Mann, S. Fabrication of Magnetic Spider Silk and Other Silk-Fiber Composites Using Inorganic Nanoparticles. *Adv. Mater.* **1998**, *10* (10), 801–805. https://doi.org/10.1002/(SICI)1521-4095(199807)10:10<801::AID-ADMA801>3.0.CO;2-I.
(167) Liu, X.; Guan, Y.; Ma, Z.; Liu, H. Surface Modification and Characterization of Magnetic Polymer Nanospheres Prepared by Miniemulsion Polymerization. *Langmuir* **2004**, *20* (23), 10278–10282. https://doi.org/10.1021/la0491908.
(168) Went, J. J.; Rathenau, G. W.; Gorter, E. W.; van Oosterhout, G. W. Hexagonal Iron-Oxide Compounds as Permanent-Magnet Materials. *Phys. Rev.* **1952**, *86* (3), 424–425. https://doi.org/10.1103/PhysRev.86.424.2.

(169) Pullar, R. C. Hexagonal Ferrites: A Review of the Synthesis, Properties and Applications of Hexaferrite Ceramics. *Prog. Mater. Sci.* **2012**, *57* (7), 1191–1334. https://doi.org/10.1016/j.pmatsci.2012.04.001.
(170) Ferk, G.; Krajnc, P.; Hamler, A.; Mertelj, A.; Cebollada, F.; Drofenik, M.; Lisjak, D. Monolithic Magneto-Optical Nanocomposites of Barium Hexaferrite Platelets in PMMA. *Sci. Rep.* **2015**, *5* (1), 11395. https://doi.org/10.1038/srep11395.
(171) Gregorin, Ž.; Sebastián, N.; Osterman, N.; Hribar Boštjančič, P.; Lisjak, D.; Mertelj, A. Dynamics of Domain Formation in a Ferromagnetic Fluid. *J. Mol. Liq.* **2022**, *366*, 120308. https://doi.org/10.1016/j.molliq.2022.120308.
(172) Gao, S.; Fleisch, M.; Rupp, R. A.; Cmok, L.; Medle-Rupnik, P.; Mertelj, A.; Lisjak, D.; Zhang, X.; Drevenšek-Olenik, I. Magnetically Tunable Optical Diffraction Gratings Based on a Ferromagnetic Liquid Crystal. *Opt. Express* **2019**, *27* (6), 8900. https://doi.org/10.1364/OE.27.008900.
(173) Philip, J. Magnetic Nanofluids (Ferrofluids): Recent Advances, Applications, Challenges, and Future Directions. *Adv. Colloid Interface Sci.* **2023**, *311*, 102810. https://doi.org/10.1016/j.cis.2022.102810.
(174) Ahmed, Y.; Paul, A.; Hribar Boštjančič, P.; Mertelj, A.; Lisjak, D.; Zabek, D. Synthesis of Barium Hexaferrite Nano-Platelets for Ethylene Glycol Ferrofluids. *J. Mater. Chem. C* **2023**, *11* (45), 16066–16073. https://doi.org/10.1039/D3TC03833E.
(175) Abdelghafour, M. M.; Orbán, Á.; Deák, Á.; Lamch, Ł.; Frank, É.; Nagy, R.; Ádám, A.; Sipos, P.; Farkas, E.; Bari, F.; Janovák, L. The Effect of Molecular Weight on the Solubility Properties of Biocompatible Poly(Ethylene Succinate) Polyester. *Polymers* **2021**, *13* (16), 2725. https://doi.org/10.3390/polym13162725.
(176) Jiang, X.; Hu, Y.; Meng, Z.; Yang, W.; Shen, F. Solubility of Succinic Acid in Different Aqueous Solvent Mixtures: Experimental Measurement and Thermodynamic Modeling. *Fluid Phase Equilibria* **2013**, *341*, 7–11. https://doi.org/10.1016/j.fluid.2012.12.018.
(177) Izunobi, J. U.; Higginbotham, C. L. Polymer Molecular Weight Analysis by ^{1}H NMR Spectroscopy. *J. Chem. Educ.* **2011**, *88* (8), 1098–1104. https://doi.org/10.1021/ed100461v.
(178) Mitra, T.; Sailakshmi, G.; Gnanamani, A.; Mandal, A. B. Studies on Cross-Linking of Succinic Acid with Chitosan/Collagen. *Mater. Res.* **2013**, *16* (4), 755–765. https://doi.org/10.1590/S1516-14392013005000059.
(179) Krishnan, K.; Krishnan, R. S. Raman and Infrared Spectra of Ethylene Glycol. *Proc. Indian Acad. Sci. - Sect. A* **1966**, *64* (2), 111. https://doi.org/10.1007/BF03047675.
(180) Phua, Y. J.; Chow, W. S.; Mohd Ishak, Z. A. The Hydrolytic Effect of Moisture and Hygrothermal Aging on Poly(Butylene Succinate)/Organo-Montmorillonite Nanocomposites. *Polym. Degrad. Stab.* **2011**, *96* (7), 1194–1203. https://doi.org/10.1016/j.polymdegradstab.2011.04.017.
(181) Wong, M.; Hollinger, J.; Kozycz, L. M.; McCormick, T. M.; Lu, Y.; Burns, D. C.; Seferos, D. S. An Apparent Size-Exclusion Quantification Limit Reveals a Molecular Weight Limit in the Synthesis of Externally Initiated Polythiophenes. *ACS Macro Lett.* **2012**, *1* (11), 1266–1269. https://doi.org/10.1021/mz300333f.
(182) Sibilia, J. P. *A Guide to Materials Characterization and Chemical Analysis*, 2nd ed.; VCH: New York, 1996.
(183) Barth, H. G.; Mays, J. W. *Modern Methods of Polymer Chararcterization*; Chemical analysis; J. Wiley & sons: New York Chichester Brisbane [etc.], 1991.

(184) Aliotta, L.; Seggiani, M.; Lazzeri, A.; Gigante, V.; Cinelli, P. A Brief Review of Poly (Butylene Succinate) (PBS) and Its Main Copolymers: Synthesis, Blends, Composites, Biodegradability, and Applications. *Polymers* **2022**, *14* (4), 844. https://doi.org/10.3390/polym14040844.

Authors Publications

1) **Ahmed, Y**.; Paul, A.; Hribar Boštjančič, P.; Mertelj, A.; Lisjak, D.; Zabek, D. Synthesis of Barium Hexaferrite Nano-Platelets for Ethylene Glycol Ferrofluids. *J. Mater. Chem. C* **2023**, *11* (45), 16066–16073. https://doi.org/10.1039/D3TC03833E.
2) **Ahmed, Y**.; Ward, B. D.; Steer, J.; Zabek, D. In Situ Polymerization of Barium Hexaferrite Ferrofluids for Poly(Ethylene) Succinate Magnetic Nanoparticle Composites. *J. Appl. Polym. Sci.* **2025**, *142* (23), e56984. https://doi.org/10.1002/app.56984.
3) Zabek, D.; Veryard, J.; **Ahmed, Y.;** Berg, A. van den; Askey, J.; Ladak, S. Structural and Magnetic Properties of Barium Hexaferrite Nanoplatelets. arXiv 2025. https://doi.org/10.48550/ARXIV.2507.03414.

Authors Oral/Poster Presentations

1) In-situ Polymerisation of Ferrofluids Creating a Barium Hexaferrite Nanoparticle Composite Matrix, presented at REPM University of Birmingham, 3rd-7th September 2023 (poster presentation).
2) Barium Hexaferrite Ferrofluid in Ethylene Glycol, presented at JEMS 13th European Magnetic Symposia, Madrid, 28th August 2023 (oral presentation).
3) Barium Hexaferrite Ferrofluid in Ethylene Glycol, presented for the M4 colloids conference at Cardiff University, 5th July 2023 (oral presentation).
4) Barium Hexaferrite Ferrofluid in Ethylene Glycol, presented at the Cardiff Engineering Research Conference, 13th July 2023 (poster presentation).
5) Barium Hexaferrite Ferrofluid in Ethylene Glycol, presented at the Advanced School in Liquids and Complex Fluids, Sheffield Hallam University, 5th-8th December 2022 (poster presentation).